Spectroscopy as a tool to investigate the high energy optical properties of nanostructured magnetically doped topological insulator

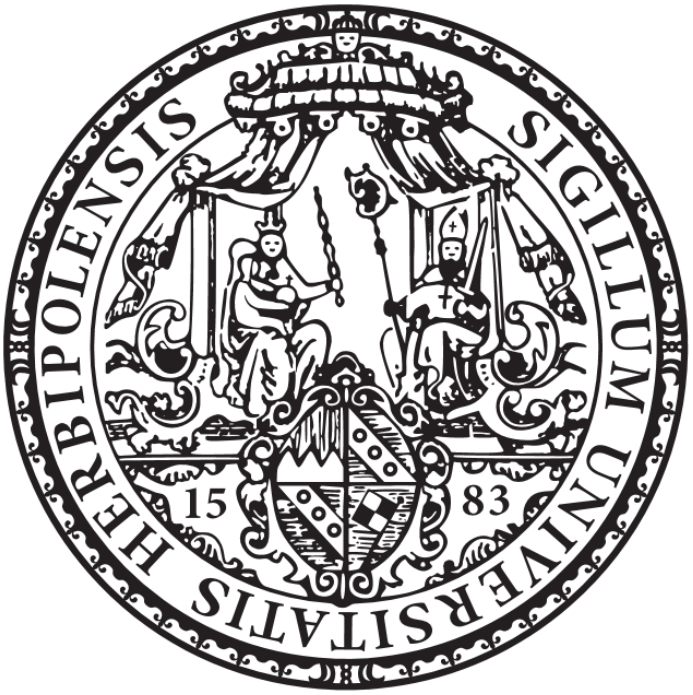

Dissertation zur Erlangung des naturwissenschaftlichen Doktorgrades der Julius-Maximilians-Universität Würzburg

vorgelegt von

Mohammed Al-Baidhani
aus Bagdad

Würzburg 2017

Eingereicht am: 07.12.2017
bei der Fakultät für Physik und Astronomie

1. Gutachter: Prof. Dr. Friedrich Reinert
2. Gutachter: Prof. Dr. Jean Geurts
3. Gutachter: Prof. Dr. Giorgio Sangiovanni
der Dissertation

Vorsitzende: Prof. Dr. Peter Michael Jakob
1. Prüfer: Prof. Dr. Friedrich Reinert
2. Prüfer: Prof. Dr. Jean Geurts
3. Prüfer: Prof. Dr. Giorgio Sangiovanni
im Promotionskolloquium

Tag des Promotionskolloquiums: 01.Februar.2018

Doktorurkunde ausgehändigt am: .....

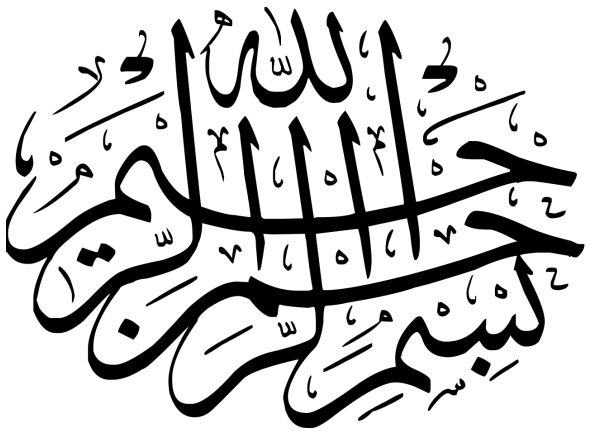

[1]

Für Al-Mahdi, Friede sei mit ihm.

ZUSAMMENFASSUNG

Die vorliegende Dissertation beschäftigt sich mit den elektronischen und hochenergetischen optischen Eigenschaften von auf der Nanoskala dünnen Filmen des magnetischen topologischen Isolators (MTI) $(V,Cr)_y(Bi_xSb_{1-x})_{2-y}Te_3$ mithilfe von Röntgenphotoelektronenspektroskopie (engl.: X-ray photoelectron spectroscopy, XPS), sowie Elektronenenergieverlustspektroskopie (engl.: electron energy-loss spectroscopy, EELS). Magnetische topologische Isolatoren sind gegenwärtig von großem Interesse, da die Kombination von Ferromagnetismus und Spin-Bahn-Kopplung in diesen Materialien zu einer neuen topologischen Phase führt, der Quanten-Anomalen-Hall-Phase (engl.: quantum anomalous Hall state, QAHS), die sich durch verlustfreie Leitungskanäle auszeichnet. Bestimmung und Kontrolle der physikalischen Eigenschaften dieser komplexen Materialien ist somit erstrebenswert für ein fundamentales Verständnis des QAHS sowie für Anwendungen in der Spintronik. EELS erlaubt die direkte Untersuchung der Elektronenenergieverlustfunktion eines Materials, aus der man, mithilfe der Kramers-Kronig-Transformation und des Drude-Lindhard-Modells von Plasmonenoszillationen, die komplexe dynamische dielektrische Funktion des Materials erhält.

In den XPS-Spektren der Rumpfniveaus in $(V,Cr)_y(Bi_xSb_{1-x})_{2-y}Te_3$ wird detailliert insbesondere der Beitrag des inelastischen Untergrunds analysiert. Es kann gezeigt werden, dass, basierend auf der in einem unabhängigen EELS-Experiment gewonnenen Elektronenenergieverlustfunktion, die Rumpfniveauspektren präzise beschrieben werden können. Dies erlaubt eine umfangreiche und quantitative Analyse der Daten, was zukünftige Rumpfniveaustudien dieser Klasse topologischer Materialien erleichtern wird. Die mit EELS gewonnenen Daten ermöglichen weiterhin eine Abschätzung der optischen Eigenschaften von Volumen und Oberfläche der Materialien, die in der vorliegenden Arbeit mit *ab initio* Berechnungen aus der Literatur für Sb_2Te_3 verglichen werden, welche auf Basis der Dichtefunktionaltheorie (DFT) in GW-näherung durchgeführt wurden. Die experimentellen Ergebnisse zeigen gute Übereinstimmungen mit der berechneten komplexen dielektrischen Funktion, sowie mit der Energieverlustfunktion. Es wird erwartet, dass die hier beschriebenen Positionen der Hauptplasmonenmoden im Allgemeinen ähnlich zu denen anderer Materialien dieser Klasse auf der Nanoskala dünner topologischer

Isolatoren sind. Somit stellt die vorliegende Arbeit das EELS Experiment als eine mächtige Methode vor, die einen Zugang zu den hochenergetischen optischen Eigenschaften dünner TIs schafft. Basierend auf den hier vorgestellten Ergebnissen bleibt es interessant sein die Auswirkungen von Stöchiometrie, magnetischer Dotierung, Filmdicke, sowie Oberflächenmorphologie auf die Energieverlustfunktion systematischer zu untersuchen, um damit ein besseres Verständnis für das komplexe Zusammenspiel aus strukturellen, elektronischen und optischen Eigenschaften in MTI-Nanostrukturen zu erlangen.

SUMMARY

In this dissertation the electronic and high-energy optical properties of thin nanoscale films of the magnetic topological insulator (MTI) $(V,Cr)_y(Bi_xSb_{1-x})_{2-y}Te_3$ are studied by means of X-ray photoelectron spectroscopy (XPS) and electron energy-loss spectroscopy (EELS). Magnetic topological insulators are presently of broad interest as the combination of ferromagnetism and spin-orbit coupling in these materials leads to a new topological phase, the quantum anomalous Hall state (QAHS), with dissipation less conduction channels. Determining and controlling the physical properties of these complex materials is therefore desirable for a fundamental understanding of the QAHS and for their possible application in spintronics. EELS can directly probe the electron energy-loss function of a material from which one can obtain the complex dynamic dielectric function by means of the Kramers-Kronig transformation and the Drude-Lindhard model of plasmon oscillations.

The XPS core-level spectra in $(V,Cr)_y(Bi_xSb_{1-x})_{2-y}Te_3$ are analyzed in detail with regards to inelastic background contributions. It is shown that the spectra can be accurately described based on the electron energy-loss function obtained from an independent EELS measurement. This allows for a comprehensive and quantitative analysis of the XPS data, which will facilitate future core-level spectroscopy studies in this class of topological materials. From the EELS data, furthermore, the bulk and surface optical properties were estimated, and compared to *ab initio* calculations based on density functional theory (DFT) performed in the GW approximation for Sb_2Te_3. The experimental results show a good agreement with the calculated complex dielectric function and the calculated energy-loss function. The positions of the main plasmon modes reported here are expected to be generally similar in other materials in this class of nanoscale TI films. Hence, the present work introduces EELS as a powerful method to access the high-energy optical properties of TI thin films. Based on the presented results it will be interesting to explore more systematically the effects of stoichiometry, magnetic doping, film thickness and surface morphology on the electron-loss function, potentially leading to a better understanding of the complex interplay of structural, electronic, magnetic and optical properties in MTI nanostructures.

TABLE OF CONTENTS

CHAPTER 1

INTRODUCTION

With the increasing scientific and technological interest on topological insulators (TI) , these materials have been extensively investigated by a number of surface science techniques regarding transport properties and electronic band structure at the nanoscale. The TI band structure possesses topologically protected, Kramers-Kronig degenerated spin-polarized surface states at the bulk band gap, due to time-reversal symmetry (TRS). The magnetic impurities implanted in the TI structure break the TRS, i.e. the degeneracy of the two spin states, creating a new quantum state of matter, namely the quantum anomalous Hall state (QAHS), at temperatures typically below 300 mK. So, the system shows the quantization of only one spin-channel at the surface or edges, which makes this system even more interesting for low-consumption spintronic applications. The recent discovery of the QAHS at the $(V,Cr)_y(Bi_x\ Sb_{1-x})_{2-y}Te_3$ MTI thin films has boosted their potential application in spintronic devices. For that it is very important to understand and control the electronic, magnetic and optical properties of these quantum nanomaterials. However, the optical properties of these systems remain not fully explored. In this context, the electron energy loss spectroscopy (EELS) is a well-established technique in the present-day analytical surface science and plays a fundamental role on probing the high energy optical properties, plasmon dispersion and the dielectric functions of complex surfaces. In this work the electron energy loss spectrum of $(V,Cr)_y(Bi_x\ Sb_{1-x})_{2-y}Te_3$ thin films was investigated by REELS and used to determine the dielectric function and the high energy optical properties of these QAH systems.

Epitaxial films of $(Bi_xSb_{1-x})_2Te_3$ were grown by molecular beam epitaxy (MBE) with thicknesses of about 10 nm, on top of Si(111) or InP(111) substrates. By coevaporation, the films were doped with magnetic V or Cr atoms. Typical Bi concentrations

were of $x = 0.21$ and (V, Cr) concentrations of $y = 0.1 - 0.2$, which corresponds to $2 - 4$ at.%. In order to prevent the MTI thin films from being contaminated during samples transportation, the nano thin films were capped by a 200 nm thick amorphous Se or Te layer. Prior to the spectroscopic experiments, heating the samples was employed as decapping process under HVU conditions. X-ray photoemission spectroscopy (XPS) measurements were performed with ASPHERE III end-station, at the XUV beamline P04 of PETRA III (DESY, Hamburg), and BESSY II beamline Helmholtz-Zentrum Berlin (UE52 PGM-Multi-Color-PES) end-station. Furthermore, XPS measurements were performed in the Experimentelle Physik VII (EPVII), Würzburg Universität with Scienta R4000 electron analyzer. The REELS measurements were performed at the EP VII, using a VG ESCALab MK II analyzer, with electron source, equipped with an electron gun (LEG 24) of LEED-System (Low Energy Electron Diffraction), with excitation energies from $10 - 1000$ eV. The crucial parameters which control the geometry used in this measurement are the angle of incidence θ_i and the angle of exit θ_o, which made an angle of $\theta_i + \theta_o = 120$.

The epitaxial films $(V,Cr)_y(Bi_x\ Sb_{1-x})_{2-y}Te_3$ samples were first characterized by XPS in order to check the Se-cap removal decapping process, and the stoichiometry in these samples. Furthermore, the XPS spectra were used to identify the inelastic background containing the energy loss signatures. Subsequently, REELS measurements were performed at different primary energies, ranging from 100 to 1000 eV. The analysis of the data comprises two steps. The first step consists in obtaining the complex dielectric function and the optical parameters from the experimental single-scattering energy loss function, by applying the Kramers-Kronig transformations. The characteristic inelastic scattering cross sections λK(E) were fitted with Drude-Lindhard oscillators. The second step consists in identifying the bulk and surface plasmon modes of the MTI thin films from the primary electron energy dependence of the experimental REEL-spectra. The relative contribution of surface and bulk plasmon oscillation in REELS has been investigated. The obtained complex dielectric function was compared to theoretical values for Sb_2Te_3, calculated by density functional theory (DFT) based on the GW approximation. The surface and bulk plasmon energies are in good agreement with the theoretical predictions.

The work is divided as follows: In chapter 1, a motivation and an introduction to the topic is presented. Chapter 2, provides the relevant theoretical background which is necessary to interpret the measured data. Chapter, 3 shows the methods and the models used to investigate the samples also the experimental setup which is used in this study. Chapter, 4 concerned with the surface preparation and the heat process used to remove selenium protective cap and the structure of the topological insulator nano thin film $(V,Cr)_y(Bi_x\ Sb_{1-x})_{2-y}Te_3$ through X-ray photoemission spectroscopy. The REELS approach is applied to different concentrations of vanadium

and chromium doped and undoped (V,Cr)$_y$(Bi$_{0.21}$ Sb$_{0.79}$)$_{2-y}$Te$_3$. Furthermore, the optical properties have been extracted and analyzed. Also, a comparison between the experimental output and the theoretical calculations, based on DFT calculation by Dr. Nechaev of Donostia International Physics Center in San Sebastán-Spain . Chapter 5 gives an outlook on finally summary of the results and on further improvements.

CHAPTER 2

TOPOLOGICAL MATERIALS

Approximately one decade ago, a new class of crystalline materials, characterized by a non-trivial topology of their band structure, has been predicted theoretically [2] and shortly after discovered experimentally [3]. These topological insulators (TI) feature an insulating three-dimensional bulk band structure whereas their surfaces support non-trivial, metallic surface states, so-called topological surface states [4–7]. TI also exist in two dimensions, i.e. in nanoscaled thin quantum well films, where the surface states appears as one-dimensional edge states [8]. The existence of topological surface states is an immediate consequence of the topology of the bulk material. Hence, they are predicted to be particularly robust in the presence of disorder, arising, for example, from impurity atoms on the surface. A notable property of the surface states is that their spin degeneracy is lifted characteristically as a result of the spin-orbit coupling [9]. In general they show a well-defined spin orientation which is locked to the direction perpendicular to the crystal momentum of the associated Bloch state function. As a consequence, the backscattering of the surface states at impurities is predicted to be strongly suppressed as long as time-reversal symmetry is not broken [3], i.e. in the absence of external magnetic fields or magnetic impurities. These unconventional properties make TI promising candidates for applications in the field of spintronics, which aims at exploiting the spin degree of freedom of the electronic states. Well-established TI materials are the layered Van-der-Waals semiconductors of $V_2\,VI_3$ class, as e.g. Sb_2Te_3, Bi_2Te_3 and Bi_2Se_3 that feature a comparably simple surface electronic structure with a single Dirac cone and a rather large bulk energy gap on the order of 100 meV or more [2, 10]. More recently, a large interest concerns the interaction between the surface states of TI with magnetic impurities [11–15]. This interest is encouraged,

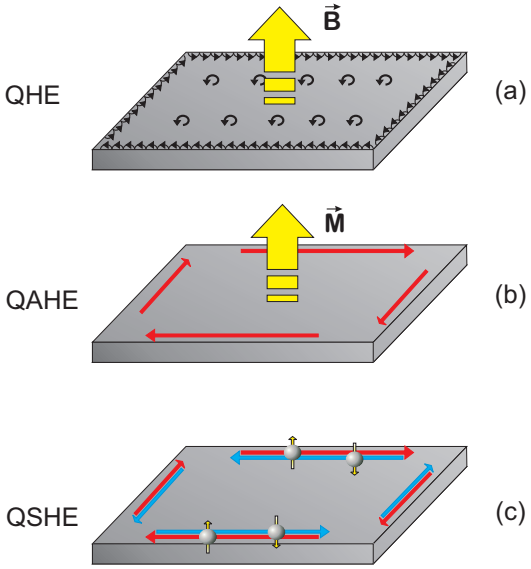

Figure 2.1: Schematic illustration of (**a**) the quantum Hall effect (QHE), (**b**) the quantum anomalous Hall effect (QAHE), and (**c**) the quantum spin Hall effect (QSHE) in a two-dimensional material system. In the QHE a chiral one-dimensional edge state appears in the presence of a strong external magnetic field. The QAHE is also characterized by a chiral edge state, but the external field is replaced by an intrinsic magnetization. The QSHE is characterized by helical edge states, i.e. by two counter propagating states with opposite spin polarization.

on the one hand, by new effects predicted by theory which are based on nanoscaled heterostructures of TI and ferromagnetic layers, such as the topological magneto-electric effect and magnetic monopoles [16]. On the other hand, such bulk doping provide possibilities to manipulate the surface electronic structure of TIs, e.g. by doping, and to test theoretical predictions on the robustness of topological surface states toward impurities. It has been shown that doping Sb_2Te_3, Bi_2Te_3 and Bi_2Se_3 by 3d impurities [17], like V or Cr, can induce ferromagnetic order in topological insulators, realizing magnetic topological insulators [14, 18–20]. In thin films of these materials the emergent combination of ferromagnetism and a non-trivial topology gives rise to the quantum anomalous Hall (QAH) effect (see fig. 2.1b) [12, 18, 21]. The QAH effect can be viewed as a realization of the quantum Hall effect [15, 22–24] in the absence of an external magnetic field. The discovery of the QAH effect spurred large interest in novel magnetoelectric phenomena in thin films of magnetic topological insulators. Figure 2.1 shows a summary of the three quantized Hall states. The first one is the quantum Hall effect (QHE) that was detected in two-dimensional Si/SiO_2 systems [22]. A quantized Hall conductance in the absence of an external field was observed in V- and Cr-doped $Bi_{2-x}Sb_xTe_3$ thin films, realizing the QAHE state. The quantum spin Hall effect (QSHE) (see fig. 2.1c)

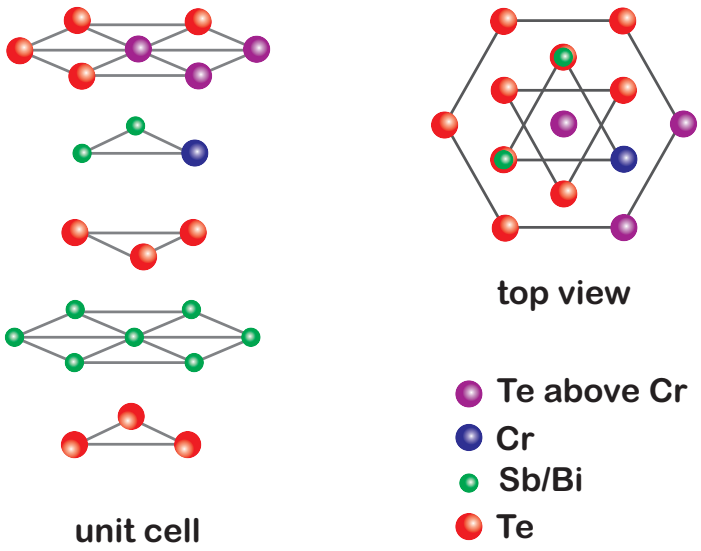

Figure 2.2: The atomic structural model indicating the position of a chromium as a ferromagnetic dopant in the topological insulator Sb_2Te_3 lattice [25].

was first theoretically predicted in graphene [2] and later observed in HgTe/CdTe quantum wells [8]. QSH insulators can be denoted as two-dimensional topological insulators.

2.1 The Bi_2Se_3-based material class of topological insulators

Lastly Bi_2Te_3, Bi_2Se_3 and Sb_2Te_3 have a layered rhombohedral crystal structure composed of quintuple layers with a hexagonal unit cell [26, 27], see fig. 2.2. Two adjacent quintuple layers are coupled by Van-der-Waals forces, which are considerably weaker than the covalent bonds within the quintuple layers. Based on first-principles calculations of the bulk band structure all three materials were predicted to be topological insulators [28]. A calculation of the surface band structure showed the expected topological surface states (see fig. 2.3) which were confirmed by angle-resolved photoemission experiments (ARPES) [10, 29]. The importance of spin-orbit coupling, which increases with the atomic number of the constituting elements, for the non-trivial topology is nicely seen by the fact that the calculation for Sb_2Se_3, i.e. the material with the lightest elements among the four examples (Z_{Sb}=51, Z_{Se}=34; vs Z_{Bi}=83, Z_{Te}=52), displays no topological surface state and, hence, trivial topological properties 2.3. It turns out that the above chalcogenide materials show a strong intrinsic charge doping probably due to defects. The resulting high bulk conductivity obscures a clear identification of the topological surface states in

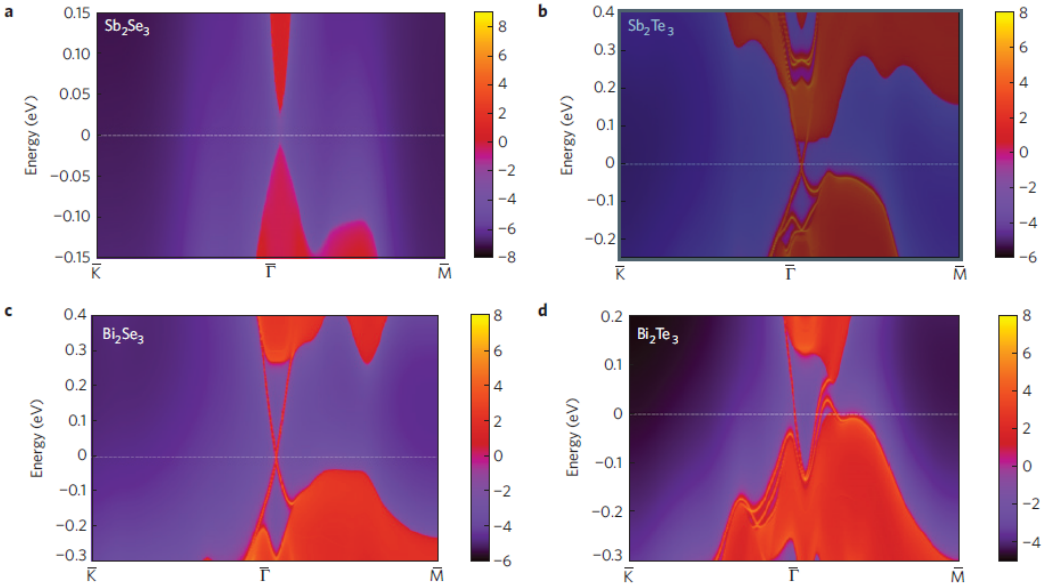

Figure 2.3: a, b, c and d represent energy and momentum dependence of the local density of states (LDOS) for (**a**)Sb_2Se_3 (**b**)Sb_2Te_3 (**c**)Bi_2Se_3 (**d**)Bi_2Te_3 on the(111) surface. The red colored regions indicate bulk energy bands and the blue regions indicate bulk energy gaps. Around the Γ point lies the surface states as red lines dispersing in the bulk gap for Sb_2Te_3 Bi_2Se_3 Bi_2Te_3. Obviously there is no surface state appearing for Sb_2Se_3 [28].

transport experiments. To address this issue, ternary or even quaternary combinations, like $Bi_{2-x}Sb_xTe_3$, are often utilized in order to minimize the bulk conductivity through charge compensation by different types of defects [28]. It was shown in ref. [3] that by varying the parameter x in $Bi_{2-x}Sb_xTe_3$ allows one to change the position of the Fermi level from the bulk conduction band to the bulk valence band [28]. In order to introduce magnetism, $Bi_{2-x}Sb_xTe_3$ and related compounds can be doped with 3d transition metal impurities. In particular, ferromagnetic order has been achieved for V- and Cr-doped $Bi_{2-x}Sb_xTe_3$ [19]. The Curie temperatures depend on doping concentration and can reach values of up to of about 100 K. In both of the above materials the QAH effect has been observed [19].

2.2 Topological insulator nanostructures

In the form of nanostructured devices, topological insulator materials offer numerous benefits to explore the nature of its surface states due to the large surface to volume ratio. Different morphologies, such as bulk crystals [30], nanoribbons [31] and nanoplates [32] were achieved, and then opens the gates towards the de-

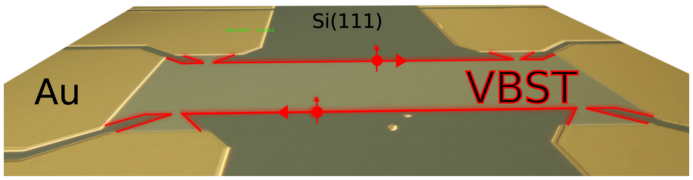

Figure 2.4: Photograph illustrate the quantum anomalous Hall effect with in the $V_{0.1}(Bi_{0.21}\ Sb_{0.79})_{1.9}Te_3$ (VBST) three dimensional nanoscale thin film device. The layers of the topological insulator with ferromagnetic dopants are of a constant thickness of about 9 nm. The thickness of each layer is 0.7 nm. These layer deposited on Si(111) substrates by means of molecular beam epitaxy (MBE), each layers consist of islands with an average diameter of about 100 nm on Si(111), all the contacts are made of gold. This device was fabricated in the Experimentelle Physik III in Würzburg [33].

velopment of novel TI nanoscale devices. The rapid developments in the field of spintronics have been enabled the enhanced understanding and control the spin dynamics in novel topological insulator. The QAHE in TI doped with ferromagnetic materials offers promising prospects towards the advent of low energy-consumption electronic devices [15, 23, 24].

Figure 2.4 shows a $V_{0.1}(Bi_{0.21}\ Sb_{0.79})_{1.9}Te_3$ (VBST) three dimensional nanoscale thin film device [33] constructed in the institute of physics Würzburg university. The use of molecular beam epitaxy (MBE) technique [34] to prepare topological insulator nanoscale films, decreases the bulk residual carriers and consequently ideal topological insulators with truly insulating bulk and tunable surface states across the Dirac point can be achieved. Therefore and because of the significant effect of the nanostructure on the topological insulators, this work concerned with the investigation of the high energy optical properties of $(V,Cr)_y(Bi_{0.21}\ Sb_{0.79})_xTe_3$ nanoscale thin films prepared by means of MBE technique.

2.3 Surface-sensitive spectroscopy of topological insulators

The hallmark of topological insulators are their topologically protected surface states that form a metallic two-dimensional electron system at the surface of an insulating bulk. Hence, the surface and bulk electronic properties of topological insulators are fundamentally different. The typical extension of the surface-state wave

function along the surface-normal direction amounts to 1-2 nm [35], according to first-principles calculations, which implies a localization at the surface on an atomic length scale. Therefore, surface-sensitive spectroscopies have played an important role in the discovery topological insulators and the subsequent investigation of their properties. Perhaps most importantly, angle-resolved photoemission spectroscopy (ARPES) is widely applied as it provides direct access to the surface band structure with a probing depth comparable to the surface-state extension along the surface-normal [2, 29]. Furthermore, scanning-tunneling-microscopy and -spectroscopy (STM and STS) are frequently used to directly probe the topological surface states [36, 37]. The present thesis aims at introducing another well-known surface-sensitive technique for the investigation of topological insulators, namely electron energy loss spectroscopy (EELS) [38, 39] at low electron energies and in reflection geometry. Compared to the other mentioned methods, EELS has very rarely been employed systematically in the context of topological insulators. Its probing depth (only for low energy) is comparable to the one of ARPES and, in particular, it can more easily be varied especially under laboratory conditions, namely by tuning the incident electron energy. As described in detail in chapter 3, EELS provides access to the electron-energy loss function of a material, that is directly related to the complex dielectric function and other optical properties [40]. In topological insulators the surface states give rise to metallic conductivity which can be expected to induce deviations in the dielectric function at the surface compared to the insulating bulk. This general consideration shows that EELS can potentially be a suitable method for the investigation of topological insulators that provides information not accessible by, e.g., ARPES and STM. Additionally, EELS often is an indispensable tool for a reliable interpretation of a XPS photoemission experiment. Firstly, the electron loss function (ELF) allows for an improved analysis of core-level photoemission (XPS) spectra [41]. Particularly in complex materials, as the V:$(BiSb)_2Te_3$ thin films studied in this work, this is important because, among others, the complex film morphology, the low concentration of the impurities, and the mixed-alloy stoichiometry make a quantitative analysis highly challenging. Secondly, the dielectric function, that reflects the interaction of light with the material, can be important for an understanding of matrix elements in valence band ARPES [42]. These matrix elements are often used to access the spin- and orbital character of topological surface states, which usually is done within the dipole approximation for the photoemission process [43, 44]. The latter, however, can be not fully valid at energies with a strong dielectric response, e.g. at and below plasmon resonances [42]. Overall, these considerations appear to provide a solid motivation to explore the use of EELS in the context of topological insulators. While addressing all the above-mentioned points goes beyond the scope of the present work, it will be shown in detail in chapter four that

EELS allows to describe comprehensively the complex inelastic background in XPS spectra of the magnetic TI V:$(BiSb)_2Te_3$.

2.4 Previous studies of optical properties and the dielectric function in the V_2 VI_3 class materials.

Many research groups investigated the dielectric function and the optical properties of the V_2 VI_3 materials. In the 1960's Greenaway et. al. studied the optical properties as well the band structure of Bi_2Se_3 and Bi_2Te_3 (see fig. 2.5) and their respective alloys like $Bi_2Te_{1.8}Se_{1.2}$ and $Bi_2Te_{2.85}Se_{0.15}$, by measuring the fundamental reflectivity over the energy range $0.1 - 12\,eV$ [45]. Another work on Bi_2Te_3, Bi_2Se_3 and Sb_2Te_3 crystals reported temperature-dependent reflectivity data in the range of $0.7 - 12.5\,eV$ [46]. With the increasing importance of the study of semiconducting materials, an X-ray photoelectron spectroscopy (XPS) and electron energy loss spectroscopy (EELS) study was published by Nascimento et. al. for single-crystalline and polycrystalline Bi_2Se_3 [47]. The EELS study with different primary energies ($100 - 2000\,eV$) allowed to distinguish surface and bulk plasmons and to identify the interband transitions.

Increasing interest in the V_2 VI_3 materials as topological insulators raised the necessity to understand in detail their electronic band structure and their optical properties. Investigations based on EELS to determine the electron loss function (ELF) and the surface electron loss function (SELF) became necessary to achieve this goal. Experiments for the Bi_2Se_3 were performed by Liou et. al. using a transmission electron microscope (TEM) with EELS option. The real and the imaginary parts of the dielectric function, as well as the energy of bulk and surface plasmons were determined with direct real-space resolution [48], see Fig. 2.7. Ou et. al. studied plasmon losses in the topological insulator $Bi_{1.5}Sb_{0.5}Te_{1.8}Se_{1.2}$ in the range $0.7 - 6.1\,eV$. The study shows plasmonic resonances from $1.2 - 5.4\,eV$ which resulted from a combination of contributions from the topologically protected surface state and interband transitions between strongly dispersive bands. Another experimental study by Zhao et.al. observed plasmon modes in nanoplates of the topological insulator Bi_2Te_3 [49]. The zero-cross frequency of the real part ε_1 (change from positive to negative) was found at 1.6 eV. They concluded that a surface plasmon should resonate at energies greater than 1.6 eV, in accordance with the ELF spectrum showing two energy-loss peaks at 2.1 and 3 eV.

Investigation concerning the "Dirac plasmons" made by Di Pietro et. al. for the topological insulator Bi_2Se_3 grown by molecular beam epitaxy (Al_2O_3) substrates using infrared spectroscopy in the very narrow energy range from 0 to $6\,\nu$(THz) which correspond to $(0 - 25\,meV)$. The plasmon position was found to be fixed

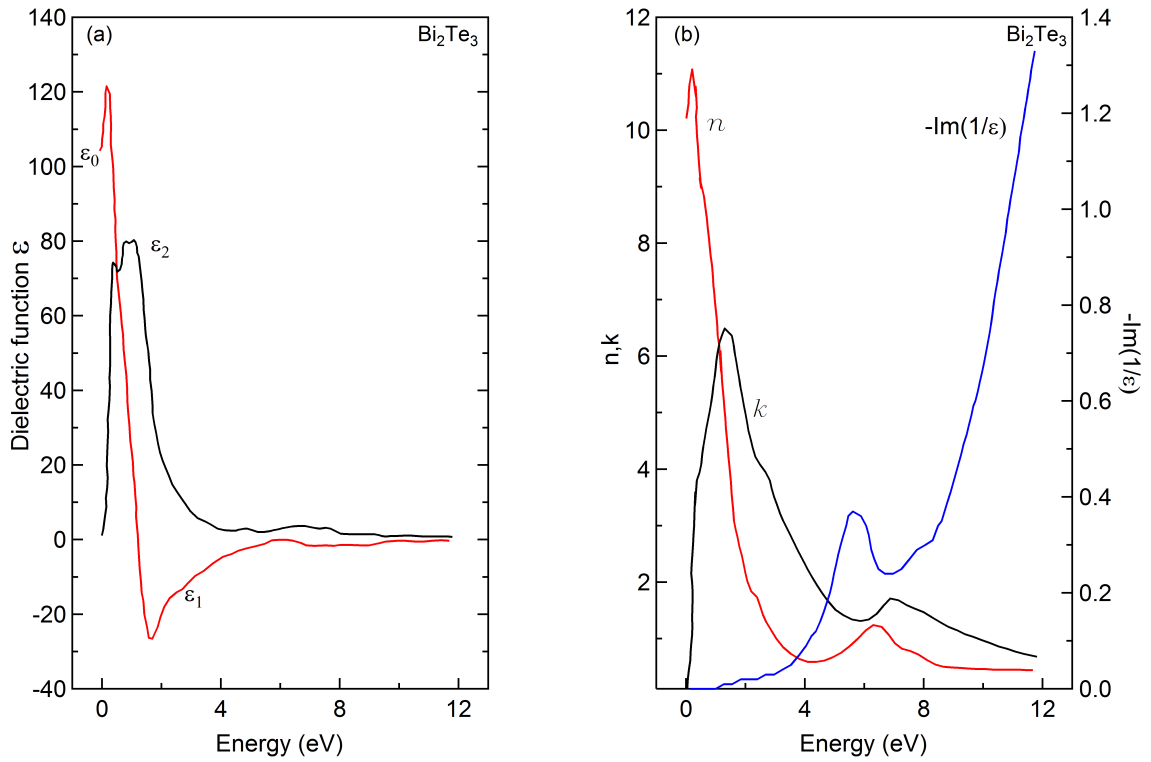

Figure 2.5: The optical constants of Bi_2Te_3 alloy obtained at room temperature as reported in [45]. Figure (a) illustrates the behavior of the real and imaginary part of the dielectric constant ε_1 and ε_2. It is obvious that the value of ε_0 is to high due to the strong interband transitions occur between 0.2 and 1.8 eV. Figure (b) shows the variation of the refractive index n and the extinction coefficients k with the energy and also the behavior of the loss function -Im$(1/\varepsilon)$. The electron loss function indicate that the plasma loss for valence electrons occurs at higher energies than the limit of their measurements. While the theoretical value calculated by Greenaway et. al. is of about 15 eV, and they did not mange to explain the peak arise at 6 eV in the -Im$(1/\varepsilon)$ spectra [45].

at approximately $2\,\nu$(THz) which is equal to (0.008 eV), even with changing the temperature from 6 to 300 K. FTIR spectroscopy was used by Reijnders et. al. to explore the optical properties of four Bi-based TIs, Bi_2Te_2Se, $BiSbSe_2Te$, Bi_2Te_3 and Bi_2Se_3 in the range $0.0025 - 5.95$ eV, see fig2.8. They found that below 43 K the reflectance increases at 16 meV due to surface state conductance [50]. By using the open-aperture Z-scan technique for thin films (800 nm) of the topological insulator Bi_2Se_3 on a quartz substrate, Krishna et. al. found a saturable absorption behavior due to the bulk insulating state [51]. A broadband absorption technique was used to probe the Bi_2Se_3 TI thin films by Sapkota et. al. in order to investigate the optical bandgap properties of this TI. Two peaks were observed in the imaginary part of

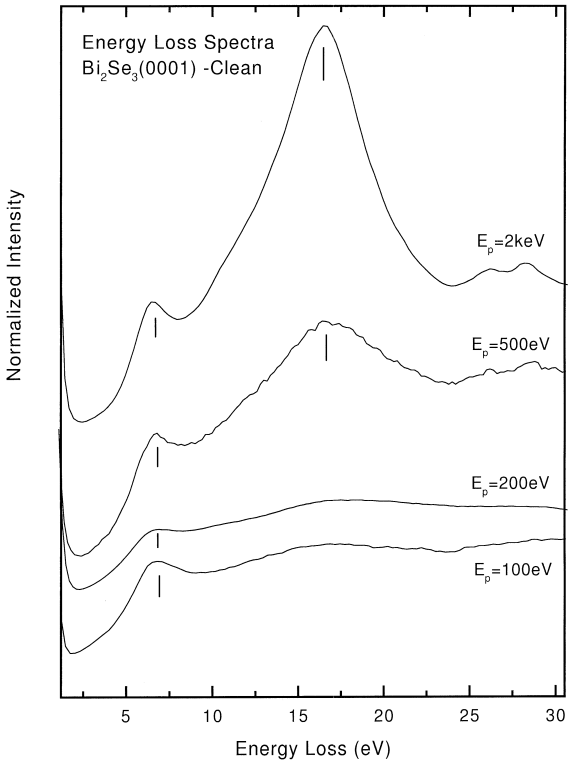

Figure 2.6: Shows the energy loss in Bi_2Se_3 (0001) semiconductor, studied by Nascimento et. al. at different incident electron beam primary energies (100, 200, 500 and 2000 eV). The feature at about 16.5 eV corresponds to a wide peak in the integrated spectra and it is the largest peak at 2000 eV primary energy explained as a loss caused by bulk plasmon. As well two other losses are observed at about 25.8 and 28.5 eV. These structures correspond to the transitions from the core levels Bi $5d_{5/2}$ and Bi $5d_{3/2}$ to the bottom of the conduction band. The remained observed losses occur at about 10.8 and 6.4 eV caused by excitation occurring at the surface, possibly a surface plasmon [47].

the dielectric function ε_2, the strongest one at 2.0 eV and a shoulder at 1.4 eV [52].

Theoretical studies of the electronic structure have been made using the density functional theory for the Bi_2Te_3 and Bi_2Se_3 topological insulators. Different kinds of approximations were employed in the DFT like the local-density approximation (LDA), the generalized gradient approximation (GGA) and the more advanced Green's function-Coulomb interaction (GW) approximation [53–57]. Nechaev et. al. calculated not just the electronc structure but also the dielectric function in its real and imagenary parts using the full-potential linearized augmented-plane-wave (FLAPW) formalism as implemented in the DFT within the GW approximation [58]. A comparison between the theoretical results and experimental EELS and TEM data for the Sb_2Te_3 in the energy range up to 50 eV was done. Five different features at

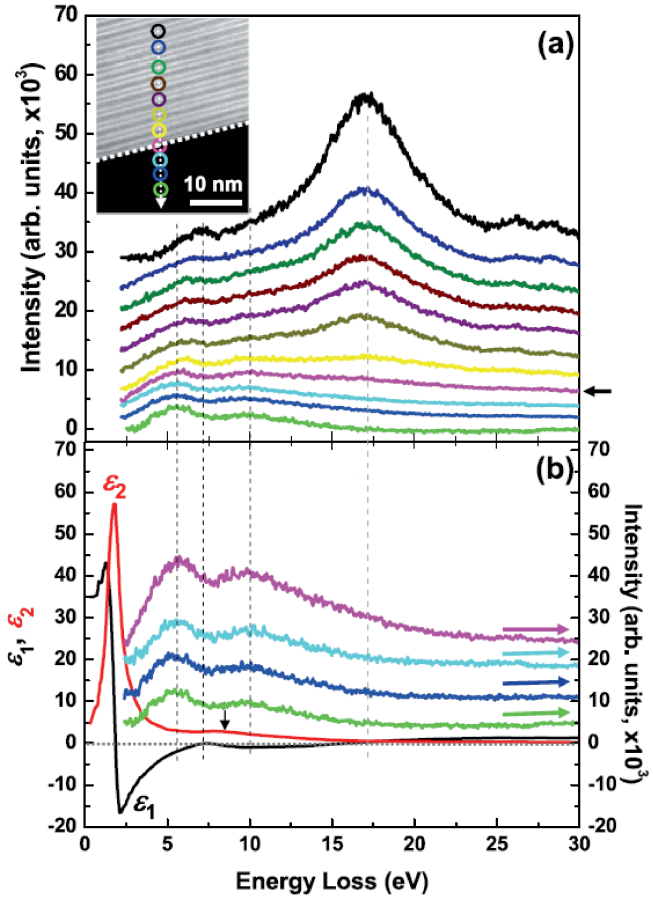

Figure 2.7: Shows the behavior of the dielectric function in its real an imaginary parts for the topological insulator single crystal Bi_2Se_3. The electron probe positioned at various locations of the material. The color circles denote probe locations and the corresponding EELS spectra are shown by the same colors. A broad feature around $(8-12\,\text{eV})$ in the imaginary part of the dielectric function due to interband transition excitations. Liou et. al. assumed a surface plasmon mods at 5.5 and 10 eV and bulk plasmon in 7 and 17 eV. While at low energy excitation $(0.7-1.6\,\text{eV})$ was also observed which attributed to the direct interband transitions [48].

5.9, 11.6, 16.5, 34.4, and 41.8 eV were observed (see fig. 2.9). A detailed comparison between the theoretical calculations of Nechaev et al. of the real and imaginary parts of the dielectric function with experimental results obtained in this thesis is presented in chapter 4.3.1).

Experimentally, Yin et. al. examined the $Bi_xSb_{1-x}Te_ySe_{1-y}$ single crystal topological insulator by means of visible to UV frequencies. A bulk plasmonic properties dominated as interband transition could be in the range of $(2-3\,\text{eV})$, and all the experimental observation carried out in the energy range $0-8\,\text{eV}$. The real and the

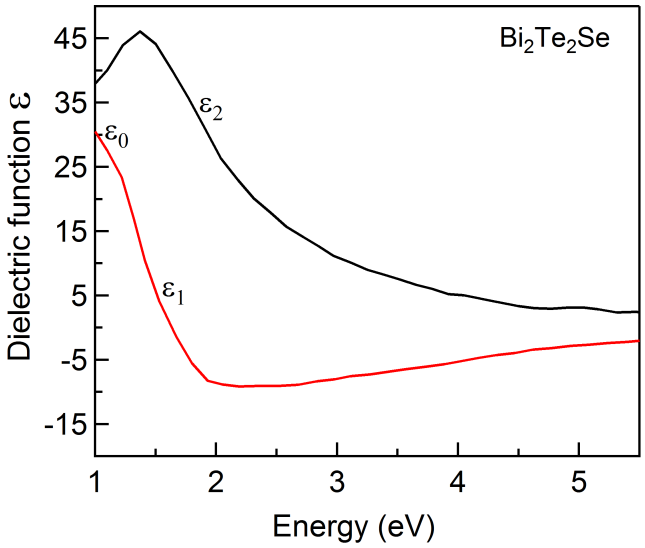

Figure 2.8: Shows the experimental behavior of the complex dielectric function ε_1 and ε_2 calculated by Reijnders et. al. for the topological insulator Bi_2Te_2Se. The bulk plasmons was not identified because of the narrow rang of energy, which is up to 5.95 eV [50].

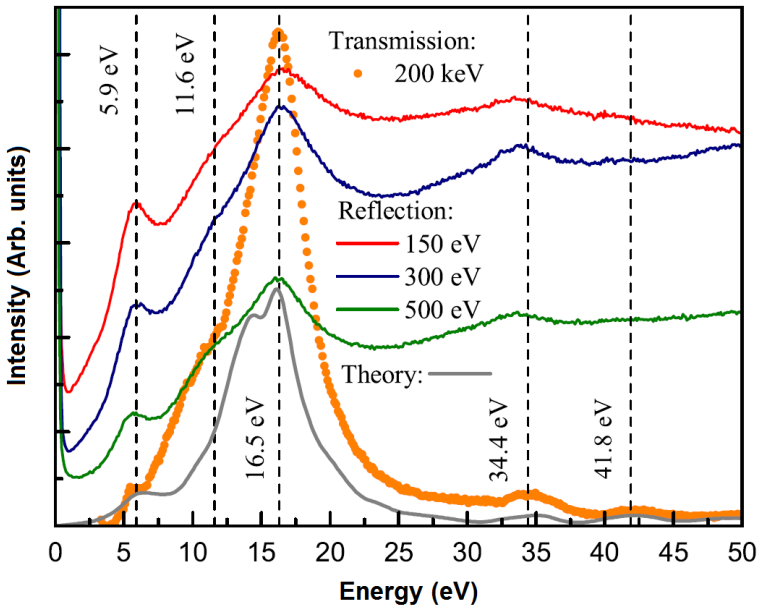

Figure 2.9: EELS data for Sb_2Te_3 in reflection and transmission modes [58]. The primary electron beam energies are 150, 300, and 500 eV for reflection EELS while it is 200 keV in the energy-filtered TEM experiment. Different plasmon modes in reflection EELS and TEM were marked at 5.9, 11.6, 16.5, 34.4, and 41.8 eV. The gray line curve represent the Gaussian-broadened theoretical ELF corresponding to the GGA+GW. The peaks at high energies are derived from the transitions from semicore states.

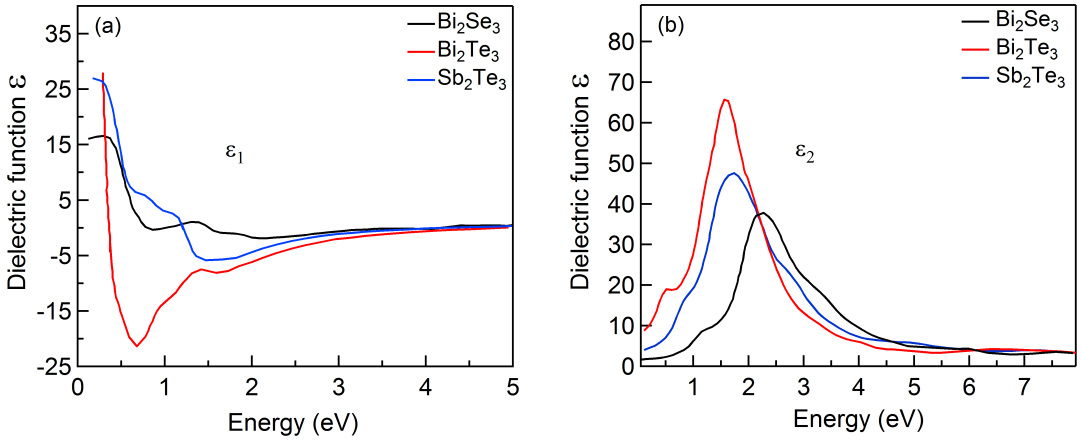

Figure 2.10: Describe the behavior of the dielectric function in its (a) real and (b) imaginary parts for Bi_2Se_3, Sb_2Te_3 and Bi_2Te_3 topological insulators observed be Yin et. al. of Nanyang Technological University, Singapore [59].

imaginary parts of the dielectric function were compared to its theoretical counterpart calculated through density functional theory (DFT) with the local density approximation (LDA) using Quantum ESPRESSO code. Furthermore a remarkable convergence between the experimental and the DFT theoretical results [59]. Figure 2.10 shows the experimental behavior of the real and imaginary parts of the dielectric function for Bi_2Se_3, Sb_2Te_3 and Bi_2Te_3. For a better understanding to the behavior of the complex dielectric function of the $(V,Cr)_y(Bi_xSb_{1-x})_{2-y}Te_3$ topological insulator, a comparison made between Yin et. al. observation and the measured real and imaginary parts of ε at the laboratories of the institute of physics in Würzburg university (see chapter 4.3.1).

CHAPTER 3

METHODOLOGY

3.1 Photoelectron spectroscopy (PES)

The base of the photoelectron spectroscopy (PES) was set by Heinrich Hertz in 1887 with his discovery of the photoelectric effect [60]. In 1905 Albert Einstein succeeded to explain this phenomena through the quantization of light, for which he received the Nobel Prize in physics 1921 [61–63]. Because of the quantum nature of the light, the fundamental photoelectric equation is:

$$E_{kin}^{max} = h\nu - \Phi_f \,, \tag{3.1}$$

where E_{kin} is the kinetic energy of the photoelectron and $h\nu$ is the energy of the exciting photon with frequency ν. The quantity Φ_f is a characteristic material and surface dependent constant of the solid and denoted by $workfunction$. For a monochromatic photon source and a known value of Φ_f, the binding energy is determined as:

$$E_{kin} = h\nu - \Phi_f - E_{bin} \,, \tag{3.2}$$

the kinetic energy of the emitted electrons from a sample depends on the work function of the material and the energies of the incident photons. Thus, electrons assigned to strongly bound core levels will be excited by X-rays. Consequently, this method is called XPS (X-ray photoelectron spectroscopy), developed to study and to analyze the samples according to their chemical composition in 1975 by Kai

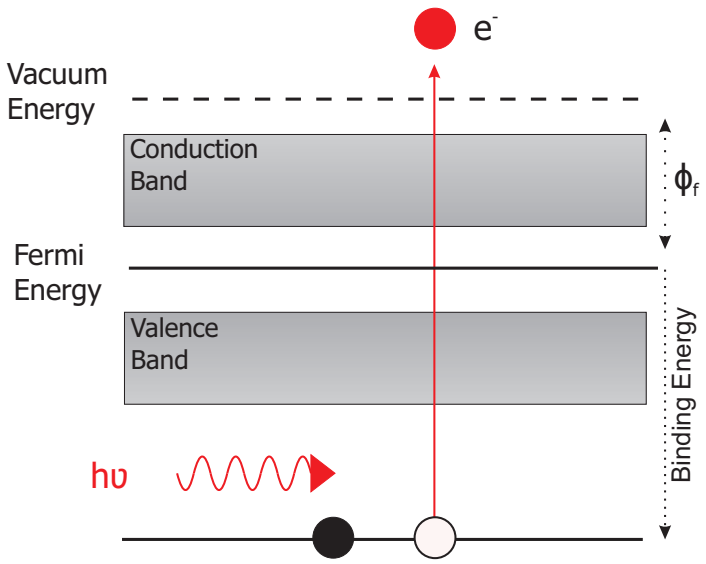

Figure 3.1: Schematic diagram of the X-ray photoemission spectroscopy process. The core level electrons are emitted after receiving sufficient amount of energy. The equation governing the process showed text above (see eq. 3.2).

Siegbahn [64] (see fig. 3.1). Furthermore, this process known as electron spectroscopy for chemical analysis (ESCA) it is widely used as a technique to investigate the chemical composition of surfaces.

In photoelectron spectroscopy, the photoelectric current generated by the excitation of electrons from an initial state $|\psi_i\rangle$ to a final state $|\psi_f\rangle$by a photon with the energy $h\nu$ is proportional to the quantum-mechanical transition probability $w_{i\to f}$ described by Fermi's golden rule [65]:

$$w_{i\to f} = \frac{2\pi}{\hbar} |\langle\psi_f|\mathbf{A}\cdot\mathbf{p}|\psi_i\rangle|^2\delta(h\nu - E_i - E_f - E_{kin}), \tag{3.3}$$

where $\mathbf{A}$ is the vector potential of the exciting electromagnetic wave and $\mathbf{p}$ the momentum operator of an electron. The δ-function guarantees the energy conservation between an initial state E_i and a final state E_f safely at an irradiated photon energy. The photoelectron inelastic mean free path of about (1-3 nm) in the energy range of 0-1500 eV makes PES a very surface sensitive method [65].

Apart from the continuous background by scattered electrons, there are other phenomena which, besides the core levels, can lead to signals in the spectrum, such as, for example, Auger electrons and electrons with characteristic energy loss. The latter consist of, for example, oscillations of the quasi-free electron gas with a specific frequency. The kinetic energy of the photoelectrons thus decreases by a characteristic value. Inelastic scattering processes occur on average according to the mean free

path of an electron (**I**nelastic **M**ean **F**ree **P**ath, IMPF) λ. It can be calculated using the $TPP-2M$ equation:

$$\lambda = \frac{E}{E_p^2[\beta ln(\gamma E) - CE^2 + DE^{-2}]}. \tag{3.4}$$

This formula is used to estimate the IMFPs and has been proposed by Tanuma, Powell and Penn [66–72], where E_p indicates the plasmon energy of free electrons, β, γ, C and D are material-specific parameters . Due to the low penetration depth of the photoelectrons, the XPS is a surface-sensitive method. The depth z can give information, which is determined by the mean free path λ and the exit angle θ relative to the normal emission [73] by:

$$z = 3\lambda cos(\theta). \tag{3.5}$$

It indicates the width of the surface layer from which 95% of the electrons are emitted. Surface sensitivity is enhanced by tilting the sample [73].

Electrons can be scattered elastically or inelastically in a solid, which manifests itself in a change in their kinetic energy. As shown in fig. 3.2 the behavior of different elements with respect to the mean free path length (IMFP) over the kinetic energy. At about 40 eV there is a minimum with an IMFP less than 5 Å. Electrons with a kinetic energy of < 40 eV are mainly scattered elastically, whereas with energies > 40 eV, the control partners are mostly electrons and provide for an inelastic scattering.

The universal curve shows the case of electrons in photoelectron spectroscopy. Here, the electron has only to be triggered once by the solid, since it is triggered by a photon. In the case of electron energy loss spectroscopy, it must be noted that the electron passes through the solid twice (incident and precipitated electrons). Therefore the IMFP will be lower for EELS than for PES. In the REELS measurements the kinetic energy of the electrons is varied between $100 - 1000$ eV and thus also the maximum penetration depth. Different mean free path lengths of electrons have been calculated using the QUASES IMFP TPP2M program [71, 72].

3.2 Electron energy loss (EELS)

In general, electron energy loss spectroscopy (EELS) is a method in which the electron beam interacts with a specimen, and the spectra of the scattered electrons, used to obtain the energy spectrum of the interactions of electrons [75]. The first theoretical predictions for electron energy loss spectroscopy were formulated by Bohm and Pines at the beginning of the 1950s, in which they modeled the behavior

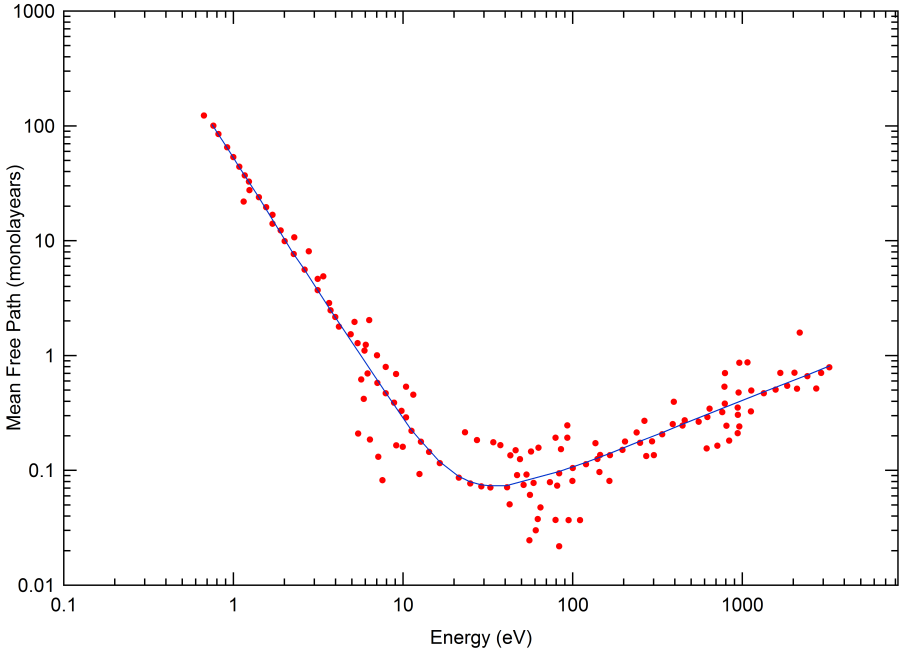

Figure 3.2: Mean free path length, plotted against the kinetic energy of electrons for various metals according to the literature by Seah and Dench in 1979 [74].

of the electrons in an electron plasma according to the individual and the collective behavior [76–78]. Later, these predictions were confirmed by Watanabe by EELS experiment on some solid materials [39].

There are two methods of electron energy loss according to the detection mode of the scattered electrons. The first mode is the reflected electrons mode, which is mainly excited by elastic scattering or backscattering of electrons and for that called reflection electron energy loss spectroscopy (REELS) measurements. This mode can be performed with very low primary energy E_0 ($100 - 1000\,\mathrm{eV}$). While the second mode is the transmission electron energy loss spectroscopy (TEELS) in contrast requires some keV because the electrons must pass through the medium [79]. In this dissertation the REELS method is employed. The surface effects are much more pronounced, which is the main focus of our research. In addition, REELS has the advantage in comparison to TEELS that the sample is not limited to a thickness less than the mean free path of the electrons. Thus, various magnetic doped topological insulator with different film and substrate thickness have been used in this work.

The electron energy loss measurement 3.3 in reflection is composed of different physical phenomena. These arise when the electrons with variable primary energy E_0 interact with the electrons and lattice atoms in the sample and are scattered elastically or inelastically. Consequently, the equation which control the electron

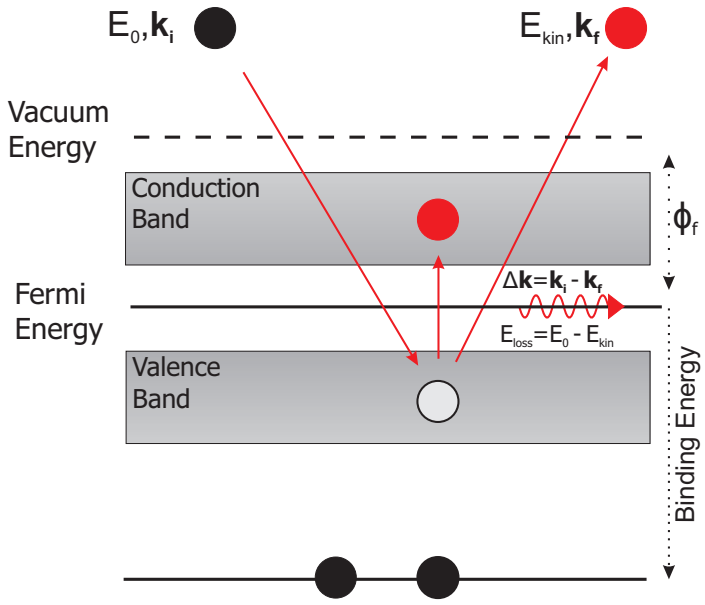

Figure 3.3: Schematic diagram of the electron energy loss spectroscopy process. The sample exposed to a beam of electrons with a known range of kinetic energies. The energy loss can be measured by the equation 3.6. Inelastic interactions include in particular phonon excitations, surface and bulk plasmon excitations and interband transition.

energy loss can be written:

$$E_{kin} = E_0 - E_{loss}. \tag{3.6}$$

The losses caused by inelastic scattering can be divided into [79]: Excitation by surface and volume plasmons, electron interactions (interband transition or ionization) and multiple scattering. In the case of excitation by surface and volume plasmons, the primary electrons cause a collective (resonant) oscillation of the valence electrons in a solid, i.e., a plasmon.

3.3 The Drude-Lorentz model

After the discovery of the electron by J.J. Thomson in 1897, Drude wrote his theory on the behavior of electrons in a metal in 1900 [80, 81]. He referred to the already existing kinetic theory of the gases and transferred them to metals, which he described as electron gas [82]. He assumed that the valence electrons can move freely through the metal, while the atomic nuclei remain immovable. In his assumptions be neglected the electron-electron interaction (independent electrons approximation), but not the Pauli principle, and the electron-atom interaction (free electrons

approximation). Thus, the electrons and the atomic bumped electron are decelerated due to the collision between them [83, 84]. The theory of Drude can be applied in good agreement on alkali, semi-metals and noble metals.

The Lorentz theory or Lorentz model is an extension of the Drude theory. Using the Lorentz oscillators to describe the electrical and ionic polarization in a solid [84]. If an electron that is bound to a lattice atom undergoes a deflection x, a restoring force arises. If it is excited by an electrical alternating field, the system dynamics will be determined by the motion equation:

$$m\frac{d^2\vec{x}}{dt^2} + m\beta\frac{d\vec{x}}{dt} + m\omega_0^2\,\vec{x} = -q\vec{E}, \tag{3.7}$$

where q is the electron charge, m is the mass, β the damping constant, ω_0 is the angular frequency of the undamped oscillator, and the driving force or in another term the electric force is $(q\vec{E})$ [84]. And thus, $\vec{x}$ in the left side of the equation 3.7 represent the deflection. The equation which describes the deflection in term of the driving electrical field and Lorentz parameters m, ω_0 and β will be

$$\vec{x}(\omega) = -\frac{q}{m_e}\cdot\frac{\vec{E}(\omega)}{\omega_0^2 - \omega^2 - i\omega\beta}. \tag{3.8}$$

By means of eq. 3.8 and the electric dipole moment $\vec{\mu}(\omega) = -q\vec{x}(\omega)$, can be written:

$$\vec{\mu}(\omega) = \frac{q^2}{m_e}\cdot\frac{\vec{E}(\omega)}{\omega_0^2 - \omega^2 - i\omega\beta}, \tag{3.9}$$

for that the Lorentz polarizability for a single atom:

$$\alpha(\omega) = \frac{q^2}{m_e}\cdot\frac{1}{\omega_0^2 - \omega^2 - i\omega\beta}, \tag{3.10}$$

and the electric polarizability per unit volume:

$$\vec{P}(\omega) = N\,\langle\vec{\mu}(\omega)\rangle = \varepsilon_0\chi(\omega)\vec{E}(\omega), \tag{3.11}$$

where N is the number of atoms per unit volume and $\langle\,\rangle$ the statistical average of the dipole moment [84],

$$\vec{\mu}(\omega) = \alpha(\omega)\vec{E}(\omega), \tag{3.12}$$

one may obtain an expression for the susceptibility $\chi(\omega) = N\alpha(\omega)/\varepsilon_0$:

$$\chi(\omega) = \left(\frac{Nq^2}{\varepsilon_0 m_e}\right) \cdot \frac{1}{\omega_0^2 - \omega^2 - i\omega\beta}. \tag{3.13}$$

the material polarization (or the electric displacement field) in incorporated into the constitutive relation

$$\vec{D} = \varepsilon_0 \vec{E} + \vec{P}, \tag{3.14}$$

where $\varepsilon_0\vec{E}$ represent the response of free space and $\vec{P}$ is the response of material. The constitutive relation (or the electric displacement field) in terms of relative permittivity and susceptibility,

$$\vec{D} = \varepsilon_0\varepsilon\vec{E} = \varepsilon_0\vec{E} + \varepsilon_0\chi\vec{E}, \tag{3.15}$$

comparing the above equations 3.14,3.15,

$$\vec{D} = \varepsilon_0\vec{E} + \vec{P} = \varepsilon_0\vec{E} + \varepsilon_0\chi\vec{E} \Rightarrow \vec{P} = \varepsilon_0\chi\vec{E}, \tag{3.16}$$

and

$$\vec{D} = \varepsilon_0\varepsilon\vec{E} = \varepsilon_0(1+\chi)\vec{E} \Rightarrow \varepsilon = 1 + \chi, \tag{3.17}$$

the dielectric function $\varepsilon(\omega)$ is defined by [84]:

$$\varepsilon(\omega) = 1 + \chi(\omega), \tag{3.18}$$

therefore, the dielectric function can be written as:

$$\varepsilon(\omega) = \varepsilon_1(\omega) + i\varepsilon_2(\omega), \tag{3.19}$$

where $\varepsilon_1(\omega)$ is the real part and $\varepsilon_2(\omega)$ is the imaginary part of the dielectric function [84] and can be determined from eq. 3.13 as well as other optical parameters, such as the refractive index n, the extinction coefficient κ, and the absorption coefficient μ which will be discussed in more detail in this section. The typical lineshape of the ε_1 and the ε_2 are shown in the fig. 3.4. The imaginary part ε_2 of the dielectric function has the shape of a resonance curve. The width of this curve depends on the damping coefficient of the harmonic oscillator. The real part ε_1 of the dielectric function has a static value for $\omega \to 0$. For increasing ω, ε_1 gains intensity, reaches a maximum in the resonance region and decreases subsequently. The first zero crossing of ε_1 is approximately at frequency called the resonance frequency ω_1. As $\omega > \omega_1$ the real part ε_1 of the dielectric function is negative. Furthermore increasing frequency it converges towards one. It is worth recalling that the real materials exhibit more

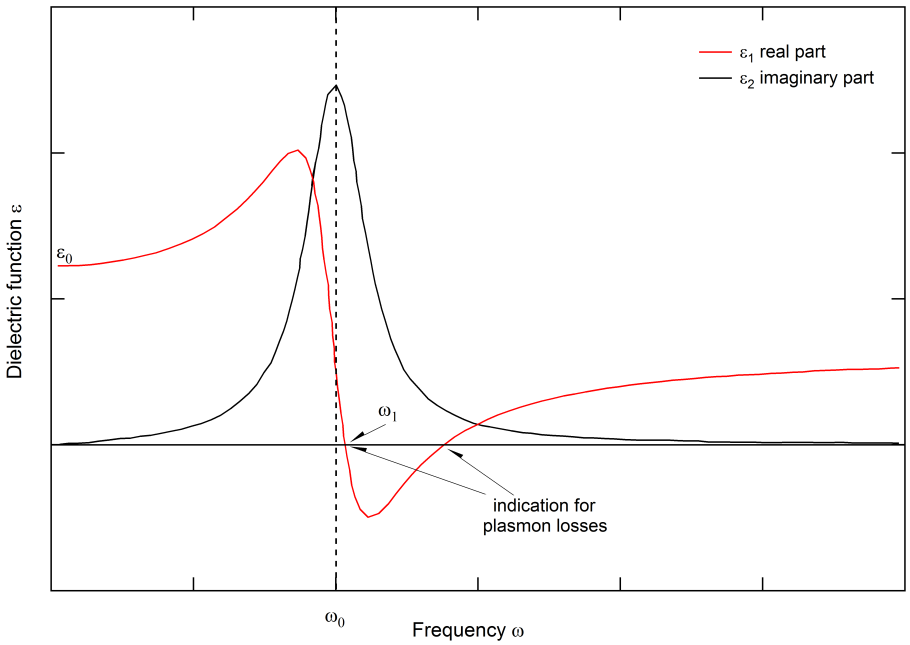

Figure 3.4: The real part ε_1 and of the imaginary part ε_2 of the dielectric function path is in dependence of the frequency ω according to the Lorentz oscillator model. Thus for a weak damping the first zero crossing of ε_1 is approximately at the resonance frequency ω_1.

than one resonance frequency. This means the dielectric function includes several contributions, e.g., a quasi-free electron contribution and an interband transition contribution [85]. A characteristic frequency is found for the quasi-free electron contribution, which can be recognized as the resonance frequency of longitudinal oscillations of electrons, known as plasma frequency ω_p. This frequency is defined by the zero-crossings of the real part ε_1 of the dielectric function and the imaginary part ε_2 must not have a maximum value [86]. The plasma oscillation is a collective oscillation of the conduction electrons. This quasi-particle is called plasmon. The plasmon frequency ω_p is proportional to the square root of the charge carrier concentration N, electron mass m_e and can be written:

$$\omega_p = \sqrt{\frac{Nq^2}{\varepsilon_0 m_e}}. \tag{3.20}$$

Thus, by recalling eq. 3.13 the susceptibility of a dielectric material can be written:

$$\chi(\omega) = \frac{\omega_p^2}{\omega_0^2 - \omega^2 - i\omega\beta}, \tag{3.21}$$

by using eq. 3.18, the dielectric function for a material with a single resonance can be written as:

$$\varepsilon(\omega) = 1 + \frac{\omega_p^2}{\omega_0^2 - \omega^2 - i\omega\beta}, \tag{3.22}$$

and split into real and imaginary parts

$$\varepsilon(\omega) = 1 + \frac{1}{(\omega_0^2 - \omega^2) - i\omega\beta} \cdot \frac{(\omega_0^2 - \omega^2) + i\omega\beta}{(\omega_0^2 - \omega^2) + i\omega\beta}$$

$$= 1 + \omega_p^2 \frac{(\omega_0^2 - \omega^2) + i\omega\beta}{(\omega_0^2 - \omega^2)^2 + \omega^2\beta^2}$$

$$= \underbrace{\left(1 + \omega^2{}_p \frac{(\omega_0^2 - \omega^2)}{(\omega_0^2 - \omega^2)^2 + \omega^2\beta^2}\right)}_{\varepsilon_1(\omega)} + i\underbrace{\left(\omega_p^2 \frac{\omega\beta}{(\omega_0^2 - \omega^2)^2 + \omega^2\beta^2}\right)}_{\varepsilon_2(\omega)}.$$

Now, recalling equation 3.19, the real part of the dielectric function:

$$\varepsilon_1(\omega) = 1 + \omega_p^2 \frac{(\omega_0^2 - \omega^2)}{(\omega_0^2 - \omega^2)^2 + \omega^2\beta^2}, \tag{3.23}$$

and the imaginary part of the dielectric function can be written as:

$$\varepsilon_2(\omega) = \omega_p^2 \frac{\omega\beta}{(\omega_0^2 - \omega^2)^2 + \omega^2\beta^2}. \tag{3.24}$$

In metals, most valence electrons can be considered as free because they are not bound to a nucleus. For this reason, the restoring force is negligible and there is no natural frequency. Thus, the Drude model for metals by assuming $\omega_0 = 0$ in equation 3.22 yield:

$$\varepsilon(\omega) = 1 - \frac{\omega_p^2}{\omega^2 + i\omega\beta} \tag{3.25}$$

so that the dielectric function for a metal in term of real and imaginary parts:

$$\varepsilon(\omega) = \underbrace{\left(1 - \frac{(\omega_p^2/\omega^2)}{(1 + (\omega^2/\beta^2)}\right)}_{\varepsilon_1(\omega)} + i\underbrace{\left(\frac{(\omega_p^2\beta)/\omega}{(1 + (\omega^2/\beta^2)}\right)}_{\varepsilon_2(\omega)} \tag{3.26}$$

Thus, the real part of dielectric constant for a metal according to 3.19 and 3.26:

$$\varepsilon_1(\omega) = 1 - \frac{(\omega_p^2/\omega^2)}{(1 + (\omega^2/\beta^2)} \tag{3.27}$$

whereas the imaginary part of the dielectric constant:

$$\varepsilon_2(\omega) = \frac{(\omega_p^2\beta)/\omega}{(1 + (\omega^2/\beta^2)} \tag{3.28}$$

The Drude-Lorentz model describes the plasmons as an oscillation of the electron gas. Plasmons losses mainly occur at a loss energy E_{loss}< 30 eV and are the dominating scattering processes [87] in the low-energy range of the loss spectrum. Incoming electrons lose energy in multiples of $\hbar\omega_p$, where $\omega_p = \sqrt{\frac{4\pi ne^2}{m_e}}$ is the plasma frequency, where n is the density of the valence electrons and e and m_e are the electron charge and mass. In the vicinity of the sample surface, the plasma frequency is reduced approximately to $\omega_p/\sqrt{2}$ for a flat surface. If the surface exhibits agglomerations, ω_p is reduced by $1/\sqrt{3}$. If the surface is contaminated, for example with oxides, this results in a new surface plasma frequency of $\omega_p/\sqrt{1+\varepsilon_0}$ with ε_0 as the dielectric constant of the contamination [88]. In electron interactions, electrons can be excited from an occupied state to an unoccupied state, or they can be completely ionized. Likewise, in the case of loss experiments, the multiple scattering of the incident electrons has to be considered. Since the sample thickness is significantly greater than the mean free path of the inelastically scattered electrons, they can scatter at other electrons or lattice atoms of the material.

The plasmon losses discussed here all have a characteristic energy loss signature, which is caused by a change in the energy $\hbar\omega$ and the momentum $\mathbf{k}$ of the inelastically scattered electrons and is characterized by the energy loss function (ELF)[89]:

$$\mathrm{Im}[-1/\varepsilon(\omega,\vec{k})]. \tag{3.29}$$

The surface-related losses are determined by the surface energy loss function (SELF):

$$\mathrm{Im}[-1/(\varepsilon(\omega,\vec{k}) + 1)]. \tag{3.30}$$

With the aid of the energy loss function $\mathrm{Im}[1/\varepsilon]$, which is accessible in a wide energy window, the real part $\mathrm{Re}[1/\varepsilon]$ can be determined by means of a Kramers-Kronig transformation [90, 91]. From equation 3.19 of the complex dielectric function, the real part of the dielectric function will be [92]:

$$\varepsilon_1 = \frac{\mathrm{Re}[1/\varepsilon]}{(\mathrm{Re}[1/\varepsilon])^2 + (\mathrm{Im}[1/\varepsilon])^2} \tag{3.31}$$

and the imaginary part of the dielectric function is [92]

$$\varepsilon_1 = \frac{\mathrm{Im}[1/\varepsilon]}{(\mathrm{Re}[1/\varepsilon])^2 + (\mathrm{Im}[1/\varepsilon])^2}. \tag{3.32}$$

The dielectric function $1/\varepsilon$ is fundamental for solid state spectroscopies and characterizes the properties of matter in dependence of the frequency ω and the wave vector $\vec{k}$. For simplicity let the dielectric function $1/\varepsilon$ depends only on ω. The dielectric function $1/\varepsilon$ links the electric field $\vec{E}$ with the electric displacement field $\vec{D}$ (see equations 3.14,3.15)according to [93]

$$\vec{D} = \varepsilon_0 \varepsilon \vec{E}. \tag{3.33}$$

the dielectric function (a common designation also is permittivity) is a measure of how a dielectric medium is influenced by an electric field, i.e., how easy atoms are polarized. The dielectric function is linked with the optical constants of the refractive index n and extinction coefficient κ [94]. In general the dielectric constant is a complex function (see equation 3.19). It is furthermore connected to the complex index of refraction via $n = n + i\kappa = \sqrt{\varepsilon}$. Explicitly one can obtain the following expressions:

$$\varepsilon_1 = n^2 - \kappa^2, \quad \varepsilon_2 = 2n\kappa$$

$$(n + i\kappa)^2 = \varepsilon_1 + i\varepsilon_2, \tag{3.34}$$

The optical properties such as the refractive index n which are obtained from $\varepsilon_1$and ε_2 [92] as:

$$n = \sqrt{\frac{1}{2}(\sqrt{\varepsilon_1^2 + \varepsilon_2^2} + \varepsilon_1)} \tag{3.35}$$

and the extinction coefficient κ can be write [92]

$$\kappa = \sqrt{\frac{1}{2}(\sqrt{\varepsilon_1^2 + \varepsilon_2^2} - \varepsilon_1)}. \tag{3.36}$$

The absorption coefficient μ [95] is related to κ

$$\mu = \frac{2\omega}{c}\kappa \tag{3.37}$$

The angular frequency $\omega = E/\hbar$. From these three parameters, the reflection coefficient R can be derived as [96]:

$$R = \frac{[(1-n)^2 + \kappa^2]}{[(1+n)^2 + \kappa^2]}. \tag{3.38}$$

the absorption coefficient A is given by:

$$A = 1 - \frac{I}{I_0}, \tag{3.39}$$

where: I is the intensity of the transmitted light and I_0 is intensity of the incident (irradiated) light. Furthermore, by using Lambert-Beerschen law:

$$I = I_0 e^{(-\mu \cdot d)}, \tag{3.40}$$

where μ is the absorption coefficient and d is the thickness of the sample, for which the possible maximum mean free path length λ is used, which results in the process of the absorption. The transmission T of the samples is determined by the relationship

$$R + A + T = 1. \tag{3.41}$$

Since the energy range of the calculations can be determined up to very large loss energies E_{loss}, this method makes it possible to access areas of the optical spectrum which far exceeds the range of conventional optical measurements. The range of E_{loss} less than 1000 eV used here covers the entire electromagnetic spectrum from microwave to terahertz range, the infrared range over the visible range, the UV range to the soft X-ray radiation. Even ellipsometric measurements do not reach the frequency range of the X-rays. Thus, the REELS method has a clear advantage with respect to the methods established so far. Furthermore, the plasma frequency can be fine-tuned by varying the doping concentration in a semiconductor a topological insulator.

3.4 Electron energy loss in condensed matter

The scattering probability P of an electron losing a certain energy $\hbar\omega$ and a momentum $\hbar\vec{k}$, in an inelastic electron scattering experiment can be define as [94]:

$$P(\vec{k},\omega)\, d\Omega\, d(\hbar\omega) = \frac{4\,a\,N}{a_0^2\,\vec{k}^4}\, S(\vec{k},\omega)\, d\Omega\, d(\hbar\omega)\,, \tag{3.42}$$

where a_0, a, and N are the Bohr radius, the layer thickness, and the density of particles, respectively. The form factor $S(\vec{k},\omega)$ is a fundamental measure for many-body systems and correspondingly, the ultimate goal of the calculation. According to the dielectric theory this form factor is related to the imaginary part of the dielectric function. Thus, for a given point charge targeted a solid and while it moves in the solid it will polarize the surrounding. For that an electric field will appears and affects the charged particle. Then the energy loss per time unit according to the form factor can be proposed [94]:

$$S(\vec{k},\omega) = -\frac{\hbar\,\vec{k}^2}{4\pi^2\,e^2\,N}\mathrm{Im}\left[\frac{1}{\varepsilon(\vec{k},\omega)}\right]. \tag{3.43}$$

In addition the excitation of oscillation of a system can be described and the influence of surfaces can be included. The factor -Im$\frac{1}{\varepsilon(\vec{k},\omega)}$ in the equation 3.43, determines the retardation of the charged particle. Thus the energy loss function (ELF) can be denoted as this factor, since it determines the energy loss spectrum. It can be stated [94]:

$$-\,\mathrm{Im}\frac{1}{\varepsilon(\vec{k},\omega)} = -\mathrm{Im}\frac{\varepsilon_1 - i\varepsilon_2}{\varepsilon_1^2+\varepsilon_2^2} = \frac{\varepsilon_2}{|\varepsilon|^2}. \tag{3.44}$$

By the single particle excitations, the imaginary part of the dielectric function ε_2 can be determined, whereas the ELF includes the collective excitations. The real part ε_1 characterizes the screening of the electrons and the ions under the presence of an external field. Thereby ε_1 is a measure of the contribution of the collective excitations. By comparison with the imaginary part ε_2 characterizes the damping of an external field due to the excitation of electron transitions in the solid. Therefore, the ELF in equation 3.44 the parameter ε_2 demonstrates the excitation of an electron and the factor $|\varepsilon|^2$ exhibits the impact of the surrounding electrons and ions. thus calculating the ELF requires just the the real or imaginary part. Actually, the ε_1 and ε_2 are associated counterpart and can be calculated with the help of the Kramers-Kronig relation [90, 91].

By means of the optical reflection measurements and employing equation 3.35 and 3.36, a complete information of the bulk dielectric function of a solid can be investigated. Another prospect to calculate ε is the excitation of electrons under the assumption that no multiple scattering events occur. This is usually given for high primary electron energies and thin foil samples. Particularly, for the inspection of fast electrons which lose energy in thin foil samples by means of transmission electron energy loss spectroscopy (TEELS) surface contamination can be neglected. While the multiple losses have to be observed by using the reflection electron energy loss (REELS) technique in order to be subtracted in a iterative equation for further evaluations. The inelastic scattering cross section $\lambda K(E)$ which is comparable to the inelastic mean free path, in that only the single particle scattering features are involved can be calculated supposing that the scattering probability is homogeneous $K(E,T)$ per energy loss T [97], is given by:

$$\lambda(E_0)K(E_0,E_0-E_i)=\frac{1}{j_l(E_0)\Delta E}\left[j_l(E_i)-\sum_{m=1}^{i-1}\lambda K(E_0,E_m-E_i)j_l(E_m)\Delta E\right] \tag{3.45}$$

where E_0 is the incoming primary electron energy, $j_l(E)$ is the measured REELS spectrum and $j_l(E_0)\Delta E$ is the area under the elastic peak. The REELS spectrum is divided into several channel E_i. This $\lambda K(E)$ can be directly correlated to the form factor $S(\vec{k},\omega)$ (see equation 3.43).

In order to obtain the pure loss function, the total intensity is normalized to 1 [92].

$$\lambda K=\int_0^E IMFP\cdot K(T)dT. \tag{3.46}$$

Hence, Tougaard assumed that the $\lambda K(E)$area ≈ 1 [98]. Because the measured energy loss range is smaller than E and because of the weak effect of the multiple elastic scattering event, he suggested that the $\lambda K(E)$area <1. He also considered that the value of the $\lambda K(E)$area lies in the range 0.7<$\lambda K(E)$area<0.95, and the lower value for $E\approx$ few hundred eV [98].

The relationship between $K(T)$ and the energy loss function Im$[-1/\varepsilon]$ is given by the Lindhard equation [99]:

$$K(E_0,\hbar\omega)=\frac{1}{\pi E_0 a_0}\int_{k-}^{k+}\frac{dk}{k}\mathrm{Im}\left(-\frac{1}{\varepsilon(k,\omega)}\right), \tag{3.47}$$

wher

$$k\pm=\sqrt{\frac{2m}{\hbar^2}}\left(\sqrt{E}\sqrt{E-\hbar\omega}\right), \tag{3.48}$$

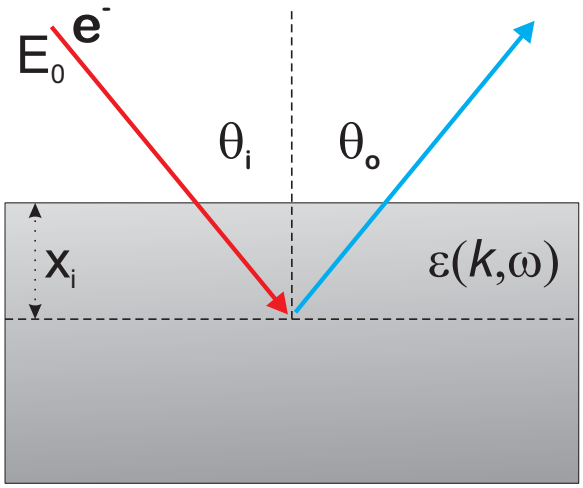

Figure 3.5: Geometric view of a REELS measurement. An electron with a primary energy E_0 targeted a sample with an incidence angle θ_i and reflected with an angle θ_o. The electron energy loss can be determined by means of the complex dielectric function $\varepsilon(k,\omega)$.

a_0 represent the Bohr radius and $\varepsilon(k,\omega)$ is the complex dielectric function of the solid.

A model to calculate the inelastic scattering cross sections as determined from REELS with the dielectric function as input was proposed in 1992 [100] for normal incidence and emission angles and in 1996 [85] it was extended to include general incidence and emission angles. Inside the solid, the electron travels a multiplicity of different trajectories, which all contribute to the experimental $\lambda K(E)$. Thus, the REELS spectrum is a superposition of all trajectories for different probing depths.

The complex dielectric function $\varepsilon(k,\omega)$ is determined of the electrons reflected from a solid surface by the energy distribution, impinging at a constant primary energy E_0 as shown in fig. 3.5. By means of $\varepsilon(k,\omega)$ the optical constants can be determined. The theory is based on the assumption that the excitations of the electrons in the solid can be described by the dielectric function $\varepsilon(k,\omega)$. To specify the dielectric function for a given measurement geometry (θ_i,θ_o), the equation for the energy loss function (ELF) which was set up by Ritchie et al. [101] is used:

$$\text{Im}\left[-\frac{1}{\varepsilon(k,\omega)}\right] = \sum_i \frac{A_i \beta_i \hbar\omega}{\left[(\hbar\omega_{0i} + \alpha_i \frac{\hbar^2 k^2}{2m})^2 - \hbar^2\omega^2\right]^2 + (\hbar\beta_i\hbar\omega)^2} \cdot \Theta(\hbar\omega - E_g), \tag{3.49}$$

where $\hbar\omega_i$, $\hbar\beta_i$ and α_i are the parameters that describe the energy, damping and dispersion of each oscillator that are employed to characterize the response in time and space of the electrons of the specimen. The step function $\Theta(\hbar\omega - E_g)$ is

included to describe the effect of a band gap in semiconductors and insulators. The dispersion parameter $\alpha_i \approx 1$ for metals for oscillators with $\hbar\omega_i < 20 - 30\,\text{eV}$ while $\alpha_i \approx 0$ for oscillators with $\hbar\omega_i > 30 - 60\,\text{eV}$. For insulators and semiconductors it is expected that $\alpha_i \approx 0$ for all oscillators when the bandgap is large ($> 3 - 9\,\text{eV}$) while $\alpha_i \approx 0.2 - 0.6$ for all oscillators when the band gap is smaller ($< 1 - 3\,\text{eV}$). These values are stated in the literature [102, 103].

The adjustment of the oscillators is ensured by the Kramers-Kronig sum rule [103]:

$$\frac{2}{\pi}\int_0^\infty \text{Im}\left[-\frac{1}{\varepsilon(k,\omega)}\right]\frac{d\omega}{\omega} + \frac{1}{n^2} = 1 \tag{3.50}$$

where n is the refractive index of the material for E$\rightarrow$0. In order to determine the theoretical loss function K_{theo} $(E_0, \hbar\omega)$ at a primary energy E_0 and the energy loss of an electron, the different orbits of the electrons in the solid must also be taken into account.

By this surface reflection model the electron and its image charge are considered, which travel through the vacuum $(\varepsilon = 1)$ and in the infinite medium. There are four terms which formed the inelastic scattering cross section, correspond to the losses of the electron [85, 104]:

- The incoming electron in the vacuum $K_{eff}^{V_i}$
- The incoming electron in the medium $K_{eff}^{M_i}$
- The outgoing electron in the medium $K_{eff}^{M_0}$
- The outgoing electron in the vacuum $K_{eff}^{V_0}$

$$K_{eff} = K_{eff}^{V_i} + K_{eff}^{M_i} + K_{eff}^{M_0} + K_{eff}^{V_0}. \tag{3.51}$$

The detailed considerations for the calculation of K_{eff} are as follows: The boundary conditions (bc) result from the electron trajectory and the conditions of the electron surface system. Using the parameter x_i^{bc}, which describes the interaction between electron and surface with respect to the angle of incidence and reflection (θ_i, θ_o) the penetration depth and the induced potential $\Phi_{bc}^{ind}(k,\omega;\varepsilon,x_i^{bc})$, the effective inelastic scattering cross section can be defined as:

$$\begin{aligned} K_{eff}^{bc}(E_0,\hbar\omega;\varepsilon,x_i^{bc}) = &\frac{2}{(2\pi)^4 x\hbar^2\omega}\int_{+\infty}^{-\infty} dt \int d^3r\rho_e(\vec{\mathbf{r}},t) \\ &\cdot \text{Re}\left[i\int d^3k\vec{k}\cdot\vec{\mathbf{v}}\Phi_{ind}^{bc}(k,\omega;\varepsilon,x_i^{bc})e^{i\vec{k}\vec{\mathbf{r}}-\omega t}\right]. \end{aligned} \tag{3.52}$$

where E_0 is the primary energy, $\vec{\mathbf{v}}$ is the velocity of electrons, $\rho_e(\vec{\mathbf{r}},t)$ is the charge density of electrons, x is the distance traveled in the solid, and t, $\vec{\mathbf{r}}$, k is the time, path and momentum variables of integration [92].

Hence, the inelastic scattering cross section is originated from a given geometry and energy of the primary electrons if the dielectric function ε is known. Thus, a Lorentz oscillator model for the dielectric function is usually used. In fact, Yubero-Tougaard theory was validated several times[40, 104, 105]. The electrons have to pass the surface region twice in a REELS experiment which is in contrast to XPS experiments. This may result in a different surface and bulk contribution of REELS in comparison with XPS [41]. This effect could be minimized by using higher primary electron energies in order to reduce the surface contribution to the REELS spectrum [106].

In order to calculate the optical properties of a system. Using the previously determined energy loss function $\mathrm{Im}\left[\frac{1}{\varepsilon(\vec{k},\omega)}\right]$, the Kramers-Kronig transformation (equation 3.50) can be used to calculate the real part [85]:

$$\begin{aligned}\mathrm{Re}\left[\frac{1}{\varepsilon(k,\omega)}\right] =& 1-\sum_{i=1}^{n}\frac{A_i(\hbar^2\omega_{0ik}^2-\hbar^2\omega^2)}{(\hbar^2\omega_{0ik}^2-\hbar^2\omega^2)^2+\gamma_i^2\hbar^2\omega^2}+\\ &\frac{2}{\pi}\int_0^{E_g}\mathrm{Im}\left[\frac{1}{\varepsilon(k,z)}\right]\frac{zdz}{z^2-\omega^2}\end{aligned} \tag{3.53}$$

Via $\mathrm{Im}\left[\frac{1}{\varepsilon(\vec{k},\omega)}\right]$ and $\mathrm{Re}\left[\frac{1}{\varepsilon(\vec{k},\omega)}\right]$ the real and imaginary part of the dielectric function, $\varepsilon(\omega)=\varepsilon_1(\omega)+i\varepsilon_2(\omega)$ can be calculated according to equations 3.31 and 3.32. These are the basis for the determination of the refractive index n according to equation 3.35, the extinction coefficient 3.36 according to equation 3.37 and the absorption coefficient A according to equation 3.39.

3.5 Theoretical calculation of the electron energy loss

Several approaches were reported concerning the electronic structure of the topological insulator [53, 55, 56, 107–109] by means of the Density Functional Theory (DFT) calculations with the (GW) approximation [110]. In this method, the electron self-energy operator is approximated by the first term of the dressed Green's function G and screened Coulomb interaction $W(\sum \approx iGW)$. Lately, the electron energy losses for the topological insulators materials have been calculated theoretically by using the (DFT) theory with the GW approximation [58, 111]. Furthermore, the local density approximation (LDA) with the Quantum ESPRESSO code employed to study the electronic structure and optical response of TI materials [59].

Another approach to determine the electron energy losses for the topological insulators is through *ab initio* calculations have been performed by using $WIEN2k$ code [112, 113]. In this scheme, generalized gradient approximation (GGA) using Perdew-Burke-Ernzenhof (PBE) parametrization [114] is adopted for the electronic exchange and correlation functional [115].

3.6 Sample description and preparation

Topological insulators doped with magnetic elements have been investigated [13, 18–20, 33, 116] by different core level techniques to study the electronic structure from the spectroscopic point of view. The well recognized technique of X-ray photoemission spectroscopy (XPS) and X-ray absorption spectroscopy (XAS) are most appropriate for that assignment. Also resonant photoemission (ResPES) used to identify the signature of the magnetic elements valence states and electron energy loss spectroscopy (EELS) to investigate the dielectric loss function and the optical properties. The previous techniques is used to study the electronic structure of Chromium and Vanadium doped $(V,Cr)_y(Bi_{0.21}Sb_{0.79})_{1-y}Te_3$ nano-structured epitaxial films grown on Si(111), InP(111).

The core of this work is based on experiments on topological insulator thin films $(V,Cr)_y(Bi_{0.21}\ Sb_{0.79})_{1-y}Te_3$ grown on Si(111) and InP(111) in Würzburg at the Experimental Physics III by molecular beam epitaxy (MBE) , in a Createc MBE system with a base pressure of 1×10^{-10} mbar. In this method [20, 117, 118], crystalline layers of high purity are grow by bombarding a directed molecular beam onto the substrate in the ultrahigh vacuum. The preparation of the samples used here are described in [20, 33, 119] and briefly described here. Prior to the growth, the Si(111) and InP(111) wafer was etched in 50 at.% hydrochloric acid to remove the oxide layer and form a hydrogen passivation on the surface. The 10 nm thick film was grown on the hydrogen passivated Si(111), InP(111) substrate at 300°C. The materials Bi, Sb, Te and Se are heated in different evaporation cells and simultaneously directed as molecular beams onto the substrate. The respective partial pressures for each element are:

$$p\text{Bi} = 1 \times 10^{-7}\,\text{mbar} \qquad p\text{Se} = 3 \times 10^{-6}\,\text{mbar}$$

$$p\text{Te} = 1 \times 10^{-7}\,\text{mbar} \qquad p\text{Cr} = 1 \times 10^{-7}\,\text{mbar}$$

$$p\text{Sb} = 1 \times 10^{-7}\,\text{mbar} \qquad p\text{V} = 1 \times 10^{-7}\,\text{mbar}$$

After growth, the film was cooled to a temperature below 10°C and capped by an amorphous Selenium, Tellurium or Al_2O_3 layer, approximately between $(2 - 200\,\text{nm})$ thick, to protect the surface from contamination during the sample

transport in air and storage outside the UHV. The protective cap is only removed immediately before the measurement in the UHV. The samples studied have nominal Vanadium concentrations of 0 at.% (as reference), 2 at.% and 4 at.%, and Chromium concentration of 0 at.% (as reference), up to 6 at.%.

3.7 Experimental setup

Under a ultra high vacuum (UHV) the photoelectron spectroscopy experiments were performed to avoid the contamination of the ferromagnetically doped topological insulator nanoscale thin film samples. Three chambers under UHV conditions were attached to one another through manual or electrical gate valves. The first of these chambers is known as the load lock and is used to brought the sample into the UHV-system, after venting it for a short time. A few hours pumping for the load lock reaches 1×10^{-7} mbar and then the sample may be transferred to the neighboring chamber called the preparation chamber. The sample preparation accomplished at a base pressure of about 5×10^{-10} mbar. Sputtering with Ar^{+} ions via a bombardment gun, used as a cleaning process for the sample surface. In addition to that a heating stage attached to this chamber, employed for the thermal treatment (decapping process) that samples may need during sample preparation.

The analysis chamber is the last destination for the sample, where the photoemission experiment take place, with a base pressure of below 5×10^{-10} mbar. The sample can be attached to the manipulator with a special sample holder dedicated to each UHV-system. This manipulator allows movement of the sample within up to six degree of freedom. As in fig. 3.6 the sample can be rotated around the azimuthal angle α in addition to the transitional movement along x,y and z, furthermore it can be tilted with the x-axis or y-axis as rotational axis. The analysis chamber is equipped with a low energy electron diffraction (LEED) experiment, which allows to monitor the surface quality of the samples. Furthermore, an electron gun attached is to one of the laboratory UHV-systems, which consequently allows the user to conduct the reflection electron energy loss spectroscopy (REELS) experiment, taking into consideration the possibility of controlling the incident and the exit angles as shown in fig. 3.7.

A photon source as well as electron analyzer are affixed to the analysis chamber. The emitted electrons travel through the analyzer, which has a multiple entrance slits, and are detected with the aid of the multichannel plate fixed behind the exit slit of the analyzer. The analyzer can be set to angular mode, which allows to resolve the electrons emission angle, and utilized for ARPES measurements (not performed in this thesis). While the second setting is the transition mode, applied frequently for

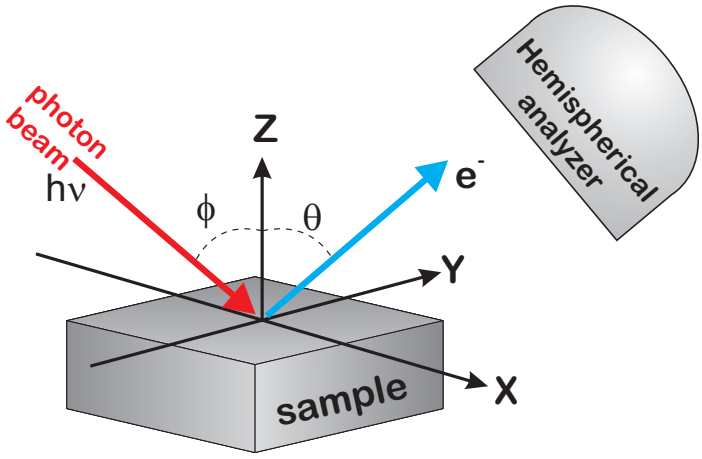

Figure 3.6: Schematic diagram of the XPS experiment. Showing the photon beam coming from an X-ray source or Synchrotron beamline and the electrons are detected be the analyzer. The important parameters to be measured are then the kinetic energy E_{kin} of the photoemission electron, and its angle with respect to the impinging light ($\phi + \theta$).

X-ray photoemission spectroscopy (XPS) measurements. Furthermore, different pass energies can be employed, which determine the energy window that is detected simultaneously. The low pass energy decrease number of the transmitted electrons but increase the resolution of the experiment. The different setups in this dissertation can be classified in laboratory setup in Würzburg university and the synchrotron setups of the Helmholtz-Zentrum Berlin and PETRA III Hamburg. The advantage of the laboratory setup are the simplicity in operation which makes it appropriate for experiments that need a particular arrangement in the experimental setup, the time-consuming for the preparatory experiments for sample characterization, whereas the synchrotron light source offers facilities for tuning the photon energy and the polarization. The setups will be described individually with more details, according to the specification and the available light source.

3.7.1 Synchrotron radiation sources

The XPS measurements were performed at the BESSY II beamline Helmholtz-Zentrum Berlin (UE52 PGM-Multi-Color-PES) end-station with PGM monochromator, energy range $h\nu \approx 85 - 1600$ eV, energy resolution > 10000 at 400 eV, Photon flux on sample several 10^{12} photons/s. And at the ASPHERE III end-station, XUV beamline P04 of PETRA III (DESY, Hamburg) with full polarization control, and energy range $h\nu \approx 250 - 3000$ eV, also with Photon flux on sample several 10^{12} photons/s [119, 120], at a base pressure of 1×10^{-10} mbar, using a Scienta R4000 electron

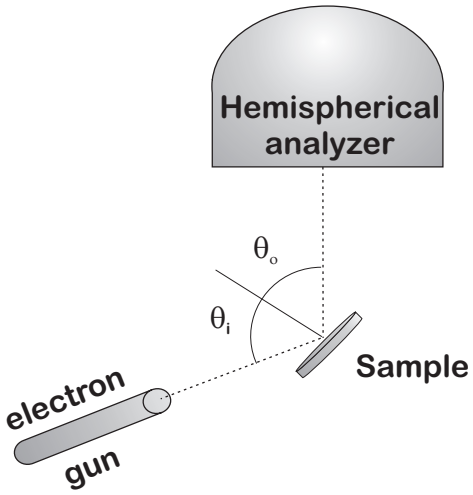

Figure 3.7: Schematic diagram of the REELS setup. The dashed line shows the beam profile of the electrons with the angle of incidence θ_i and the angle of exit θ_o. These two angles regard to the surface normal of the TI sample makes ($\theta_i + \theta_o = 120°$).

analyzer with energy resolution $\Delta E < 10\,meV$, momentum resolution $\Delta k \approx 0.01\,Å^{-1}$, parallel angle detection $\Delta\theta \approx 20°$ and Kinetic energy range $E_{kin} \approx 0 - 3\,keV$.

Prior to the measurements, the samples were decapped by heating up to 180°C under a pressure of 1×10^{-9} mbar. The measurements were performed at room temperature, and for different photon energies, in order to reduce secondary-electron background, optimize matrix element effects, and look for resonances.

3.7.2 Laboratories at the Institute of Physics - Würzburg University

Reflection electron energy loss spectroscopy (REELS) were acquired at the Institute of Physics, Würzburg University, with a VG ESCALab MK II analyzer. For the electron source, an electron gun (LEG 24) of LEED-System (Low Energy Electron Diffraction) Model 8011 (Thermo VG scientific) the electron energy loss measurements have been performed in Reflection (REELS), providing excitation energies from $10 - 1000\,eV$, The electron gun was run at a constant filament current of 2.5 A and an emission current of 0.35 mA. All experiments were performed at an incident angle of 56° and an exit angle of 64° (with respect to the surface normal of the sample) that means the angle between electron gun and electron analyzer is $\theta_i + \theta_o = 120°$ (see fig. 3.7). The base pressure was 1×10^{-10} mbar [121]. In order to enhance the surface sensitivity, the energy of the primary electron varied from $100 - 1000\,eV$ in 50 eV steps. The results this energy range are presented. All experiments were carried out at room temperature. In additions extra XPS measurements where per-

formed in the same institute with Scienta R4000 electron analyzer, with magnesium anode (Mg $K_\alpha : h\upsilon = 1253.6\,eV$), and aluminum anode (Al $K_\alpha : h\upsilon = 1486.6\,eV$). All the measurements were taken at a base pressure of 1×10^{-10} mbar. Since these measurements are mainly based on the phenomena on the surface they must be carried out in UHV. This prevents the surface from being immediately contaminated with adsorbates which would falsify the results. The surface contamination residues can be removed by a SPECS IQE11 Ar^+ ion sputtering gun in the preparation chamber. Sputtering process goes under certain conditions, acceleration voltage of 50 V and at pressure of $p \leq 5.4 \times 10^{-5}$ mbar at an angle of $\pm 45°$ to the sample normal.

3.8 Experimental quantitative analysis

The analysis of the XPS data sets is explained below by means of an example. For the evaluation of the measured data sets the correction of the satellite lines was made in the first step. In addition to the most intense main line (here: Al $K_{\alpha 1,2}$), the radiation of the non-monochromatized X-ray source has additional secondary lines (e.g. $K_{\alpha 3,4}$, Al K_β). Measurement signals derived from electrons that have been excited by photons of secondary lines are called satellites [122, 123]. The measured spectra were corrected by two satellites shifted by the energy of $+9.8\,eV$ ($\alpha 3$) or $+11.8\,eV$ ($\alpha 4$), and showing 6.4% and 3.2% of the intensity of the corresponding main line [123]. After adjusting the satellite of the background of the spectrum was subtracted. The simplest option is the adoption of a linear background from start to finish of an intensity maximum, but this leads to the asymmetry of the background to inaccuracies.

Processing XPS data requires an efficient method to treat the background signal. A procedure was described by D.A. Shirley's [124] in order to remove the background signal:

$$S_n(E) = k_n \int_E^{E_{right}} dE' \left[I(E') - I_{right} - B_{n-1}(E') \right] \tag{3.54}$$

where E is the kinetic energy, (I_{right} and E_{right}) represent a point at the right side of the peak (low binding energy). $S_n(E)$ represent the iterative of Shirley background, k_n defines the step in the background and $I(E')$ is the photoelectric signal.

Figure 3.8 shows a measured XPS spectrum of the Te 3d core levels.The satellites at approximately 560.8 eV and 562.84 eV arises in the low binding energy because typical X-ray sources also emit some X-rays of a slightly higher photon energy than the main Al K_α line. These satellite peaks are ghost lines of the main Te $3d_{3/2}$ and Te $3d_{5/2}$ peaks arising from ionization by these additional X-rays. The intensity of the satellites of the electron loss (5/2, 3/2) is too small to be seen in the figure. In

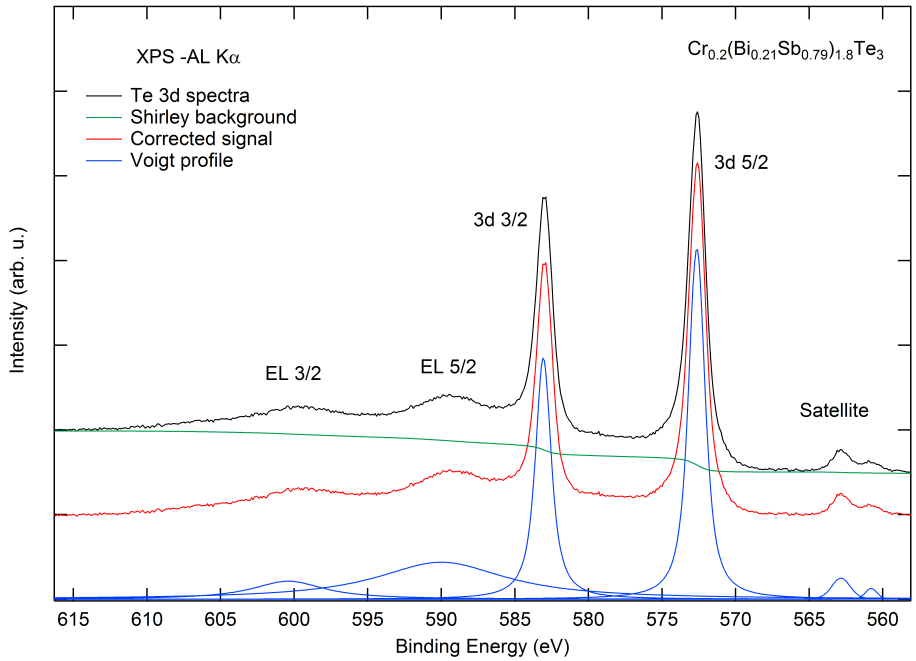

Figure 3.8: The XPS measurement spectrum of the Te 3d core level for the $Cr_{0.2}(Bi_{0.21}Sb_{0.79})_{1.8}Te_3$ film in normal emission (—). The Shirley background plotted with (—) lineshape, and the (—) lineshape represent the corrected spectrum, while the (—) Voigt peaks were adapted to each individual signals. Furthermore, two satellite peaks appear at the binding energy range $560.8 - 562.84\,\text{eV}$.

the core-level peaks and the satellite peaks, Shirley background was calculated. A linear background was assumed for the range of the loss peaks ($E_B \geq 585\,\text{eV}$) due to the shape of the spectrum.

To track the progress of the core levels, Voigt profiles were adjusted to the maximum intensity. These are characterized by position, peak height (maximum intensity), width and a factor which indicates the ratio between Gaussian and Lorentzian proportions. Apart from the two intensity maxima of the separate spin-orbit splitted Te $3d_{3/2}$ and Te $3d_{5/2}$ core levels, two broad lines are seen at larger binding energies, which are caused by electrons losses, and have a lower kinetic energy due to characteristic energy losses on the way to the sample surface. They are marked with $EL_{3/2}$ or $EL_{5/2}$ in fig. 3.8. For adjusting the core level and the loss peaks, known parameters from the literature were used. The signals of the loss electrons were treated the same as those of the core levels.

In the literature [125] the spin orbit splitting for Te 3d is $\Delta E\,(\text{Te}\,3\text{d}) = 10.4\,\text{eV}$. Since the widths and the Gauss-Lorentz factor of the two lines must coincide respectively, these (separately for core levels and loss lines) were equated. The area ratio of the split lines to each other is for electrons of any atom X that are

emitted from d-orbitals [122]:

$$h(X_{5/2}) \cdot h(X_{3/2}) = 3:2. \tag{3.55}$$

Except the widths form factors of the peaks, the height ratio was fixed. The binding energies of the Te $3d_{3/2}$ and Te $3d_{5/2}$ levels can be determined to be 572.64 eV and 583.4 eV respectively, which is consistent with the literature values at 573 eV and 583 eV [123]. The loss peaks are 589.86 eV ($EL_{3/2}$) and 600.8 eV ($EL_{5/2}$). This corresponds to an energy difference of E(EL $3d_{3/2}$)−E(EL $3d_{5/2}$) = 17.4 eV.

Another background method was proposed by Sven Tougaard [40, 126–130]. The idea of Tougaard background is based on the existence of an energy loss cross section $F(x)$, which represent the probability of an electron undergo a loss in its energy. This excitation consequently appears as a contribution to the background. An equation was used to calculate this background from a given spectrum $S(E')$:

$$T(E) = \int_E^\infty F(E' - E)S(E')dE' \tag{3.56}$$

Tougaard offers a universal cross section suitable for most metals, their oxides and alloys. Furthermore, cross section for polymers and semiconductors were included in his software package. The third facility is to use the cross section of given sample calculated from REELS experiment. In this work Tougaard background was used to process the XPS data.

Several factors control the X-ray photoemission intensity from surface. If a homogeneous specimen, with an infinite thickness, vertical detection, and the angle between photon source and detector so that the angular asymmetry is unity are assumed, then the intensity line of an element A for XPS chart at a specific kinetic energy E_A of a photoelectron is given as [131]:

$$\frac{N_A}{N_B} = \frac{I_A \sigma_{rel,B} T(E_{kin,B}) \lambda(E_{kin,B})}{I_B \sigma_{rel,A} T(E_{kin,A}) \lambda(E_{kin,A})}. \tag{3.57}$$

Here, $I_{A,B}$ indicate the area under the maximal intensity, the cross section $\sigma_{rel,A/B}$ can be found in reference [132]. The IMFP $\lambda(E_{A/B})$ is calculated according to the eq. 3.4 . The transmission function $T(E_{kin,A/B})$ depends on the analyzer used. In the stoichiometric calculations for Bi 5d, Sb 4d, Te 4d and Se 3d performed in this work [133], the energy range of the analyzed core level excitations for the SES 200 analyzer used is: $T(E_{kin}) \approx 1$. The area and position of these core levels were determined by a simultaneous fit of Voigt profiles of the peaks where the area ratio was fixed according to the spin-orbit split $(2j + 1)$.

CHAPTER 4

ANALYTIC REVIEW

In the following, the measurements, the analysis and the results of magnetically doped nano topological insulator thin films $(V,Cr)_y(Bi_xSb_{1-x})_{2-y}Te_3$ with different Vanadium and Chromium concentrations. This system was examined with two described measuring methods, XPS and REELS. In addition, the samples produced by means of MBE on which the main attention of this study is based. A magnetically doped nano topological insulator sample was tested for comparison in order to be able to trace possible differences in the surface characteristics of the samples to the type and ratio of doping and the preparation. The second part of this studies will exhibit the analysis and the results of REELS measurements, and the optical properties of these magnetic doped nano topological insulators based on the XPS data.

4.1 Surface preparation and Se protective cap.

The $(V,Cr)_y(Bi_xSb_{1-x})_{2-y}Te_3$ topological insulator films were grown in an UHV-chamber dedicated to the MBE growth of semiconductor thin films. In order to perform the spectroscopic characterization by XPS and EELS, it was necessary to transport the samples under atmospheric conditions into another chamber or to synchrotron facilities. Therefore, it was required to protect the films against oxidation and other contamination in air. This was accomplished by covering the as-grown sample with thick amorphous selenium capping layers. After introducing the sample in the characterization chamber, prior to the experiment, the cap was removed from the film by heating up to about 167°C for a few minutes. Shortly

before reaching the desorption temperature, a transitory change of the sample surface can be observed at bare eye, namely the surface exhibits a "milky" appearance. The desorption is complete when the milky phase disappears. Excessively high temperatures (> 180°C) may lead to evaporation of Te atoms from the surface and change of the surface stoichiometry and of the TI film structure. If the temperature is too low, the protective layer is not completely removed from the surface. The LEED experiment provides a first control of the surface quality. After the successful removal of the capping layer, the ordered surface of the TI film shows a clear LEED pattern with a sixfold symmetry, in agreement with the expected (111) plane orientation of the surface, as seen in the inset of fig 4.1 for a $Cr_{0.1}(Bi_{0.21}Sb_{0.79})_{1.9}Te_3$ film. The diffuse character of the LEED pattern points out the disorder of the film surface after decapping.

Before and after the decapping process, XPS was performed at the surface of the sample in order to get a clear vision to the changes occur after this thermal treatment (Se cap removal). Figure 4.1 shows the Se 3d core level from a $Cr_{0.1}(Bi_{0.21}Sb_{0.79})_{1.9}Te_3$ film, measured with the Al K_α line ($h\nu$ = 1486.6 eV), at normal emission, before and after decapping. The film was capped with a 200 nm thick amorphous Se layer. A binding energy of 55.9 eV for the Se 3d level measured at the Se-cap (black curve) agrees well with the value of bulk elemental selenium [103]. After the decapping procedure (red curve), an energy shift of approximately 1.2 eV towards smaller binding energies is observed. This is a signature of a different chemical environment of the Se atoms at the surface of the $Cr_{0.1}(Bi_{0.21}Sb_{0.79})_{1.9}Te_3$ film, suggesting a possible substitution of Te by Se atoms. A more detailed analysis of the angle-dependence of the Se core levels after the decapping procedure revealed a Se-rich environment at the surface, with a gradient of Se concentration within the first $2-3$ quintuple layers. This serves as evidence for the incomplete removal of the Se cap. This will be discussed in detail in section 4.2.1.

4.2 Electronic structure of the magnetically doped topological insulator films

A first survey of the chemical fingerprint of a layered system can be obtained by the photoelectron spectroscopic investigation of the core-levels. Figure 4.2 shows an overview XPS spectrum of a decapped $V_{0.1}(Bi_{0.21}Sb_{0.79})_{1.9}Te_3$, taken at $h\nu$ = 1000 eV, at beamline P04 (PETRA III, DESY). All core-level and Auger excitation peaks of the expected constituent elements are identified and labeled. The spectra in fig. 4.2 shows some carbon contamination of the surface (C 1s, E_B = 285 eV), which can be due to the heating process adopted to remove the Se cap. Remarkably strong are

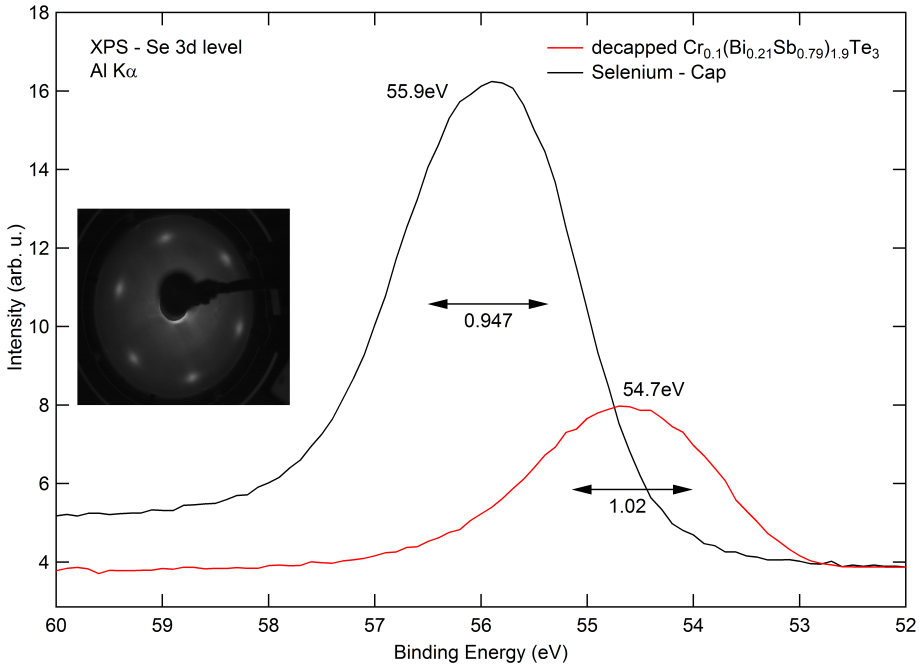

Figure 4.1: X-ray photoemission spectroscopy spectra of Se 3d before and after the decapping process, and LEED image at 40 eV, taken at the Al K_α line ($h\nu = 1486.6$ eV), illustrate the success of selenium cap removal. The FWHM for the decapped $Cr_{0.1}(Bi_{0.21}Sb_{0.79})_{1.9}Te_3$ is about 0.947 and of about 1.02 for the amorphous selenium cap. The binding energy of the Se 3d level are labeled, and both spectra were normalized. Inset: represent LEED pattern of the surface after a successful decapping

the Se $3d_{5/2}$ and $3d_{3/2}$ peaks (53.2 eV and 54.1 eV, respectively). Other Se peaks observed are the $3p_{3/2}$ (162.8 eV), $3p_{1/2}$) (168.4 eV) and 3s (232 eV). In addition, we also identified the main intrinsic core-level peaks of the other constituent elements, briefly summarized as follows. The Bi peaks observed are the $5d_{7/2}$ (24.5 eV), $5d_{5/2}$ (27.8 eV), $4f_{7/2}$ (160.6 eV), $4f_{5/2}$ (166 eV), $4d_{5/2}$ (440 eV) and $4d_{3/2}$ (464 eV). From Sb, the peaks observed are the $4d_{5/2}$ (32.4 eV), $4d_{3/2}$ (33.9 eV), $3d_{5/2}$ (531.8 eV) and $3d_{3/2}$ (541.2 eV). From Te, we identified the $4d_{5/2}$ (39.9 eV), $4d_{3/2}$ (41.3 eV) $3d_{5/2}$ (592.8 eV) and $3d_{3/2}$ (603.2 eV). One could expect to observe some oxygen contamination, but the O 1s core-level (531 eV) overlaps with the strong Sb $3d_{5/2}$ and therefore could not be distinguished.

In particular, the V $2p_{3/2}$ and $2p_{1/2}$ core-levels were clearly identified, respectively at 512 eV and 520 eV, even at such low concentrations as $2-4\%$. In the case of Cr-doped TI samples, the Cr 2p peaks coincide with the strong Te 3d levels, thus making its determination very difficult. As an alternative approach to estimate the Cr 2p lineshape in TI films, we measured a similar system containing Se instead of

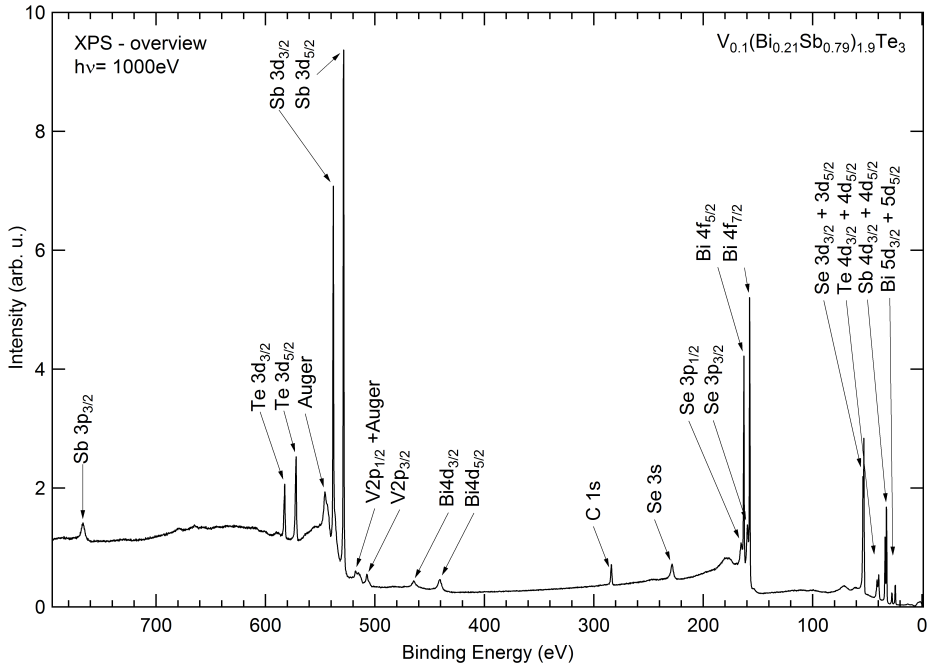

Figure 4.2: X-ray photoemission overview spectrum of $V_{0.1}(Bi_{0.21}Sb_{0.79})_{1.9}Te_3$, measured at beamline P04 (PETRA III, DESY), at $hv = 1000\,\text{eV}$, after decapping. All core-level and Auger excitation peaks of the constituent elements are labeled. The C 1s peak points out some carbon contamination. The Se peaks show reminiscent Se at the surface after the cap removal.

Te as ligand atom, namely $Cr_{0.1}(Bi_{0.21}Sb_{0.79})_{1.9}Te_3$, since the Cr 2p levels would not overlap with any other spectroscopic feature. Figure 4.3 shows the trace of Cr 2p and Te 3d core-levels for $Cr_{0.4}(Bi_{0.21}Sb_{0.79})_{1.6}Te_3$ (black curve) and $Cr_{0.1}(Bi_{0.21}Sb_{0.79})_{1.9}Te_3$ (red curve) films, measured at $hv = 1000\,\text{eV}$, at beamline P04 (PETRA III, DESY). In the sample containing Te, the Cr 2p peaks contribute to the spectral weight as an asymmetric shoulder at the high binding energy side of the Te 3d peaks. It is clearly difficult to distinguish the Cr 2p lineshape. On the other hand, in the sample containing Se, one can see the intrinsic lineshape of the Cr 2p states. In the inset, one can distinguish a complex multiplet structure of the Cr $2p_{3/2}$, with a maximum at 573.7 eV. The complex lineshape may be due to different ionization states that may occur when two different Cr species are present. For instance, Cr atoms in large Cr-clusters, in addition to the Cr as dilute impurities, may also lead to this kind of splitting in the core-levels.

For an estimation of the stoichiometry of the samples, a systematic quantitative analysis of the core-level spectra is required. First, detailed measurements of particular core-levels are performed with high statistics. Then, the intrinsic spectra are extracted from the raw experimental data by modeling of the background and the in-

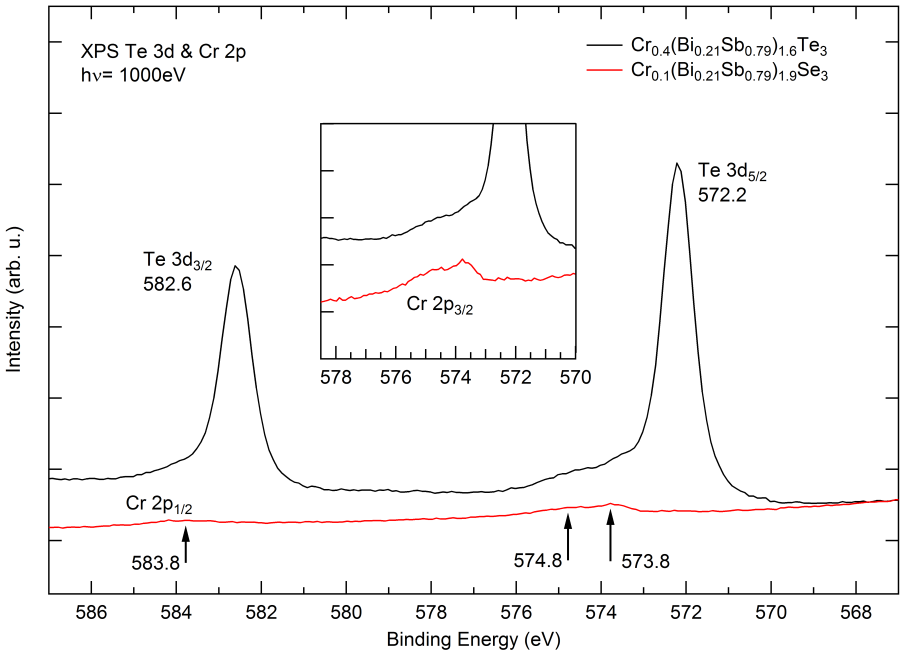

Figure 4.3: X-ray photoemission spectra of the Cr 2p core-levels at the (black curve) $Cr_{0.4}(Bi_{0.21}Sb_{0.79})_{1.6}Te_3$ and (red curve) $Cr_{0.1}(Bi_{0.21}Sb_{0.79})_{1.9}Te_3$ films, measured at $h\nu$=1000 eV, at beamline P04 (PETRA III, DESY). The different compositions of the samples were chosen in order to avoid the overlap of Cr 2p with Te 3d levels, and thus facilitate the determination of the Cr 2p lineshape.

dividual lineshapes. This is shown in the following subsections for angle-dependent XPS measurements and for the main core-levels of the constituent elements.

4.2.1 Depth information and surface stoichiometry from the angle-dependence of the core levels

As mentioned in chapter 3, it is possible to estimate the stoichiometry of the crystals from the quantitative analysis of the core spectra, in order to determine, for example, the changes in selenium and tellurium concentrations at and near the surface. For that, angle-dependent XPS measurements of the core-levels can provide depth information of the sample stoichiometry. The probing depth of XPS measurements is determined by the photoelectron escape depth, i.e. the path the photoelectron must travel from the point where it was excited up to the surface. Along this path, the photoelectron may undergo further (elastic as well as inelastic) scattering. The longer the path, the larger the probability of multiple scattering events, and the lower the chance of the photoelectron escaping the surface. The length of this path is proportional to the the IMFP and the $\cos(\theta)$ of the emission angle (see equation 3.5).

Thus, the shortest path is experienced by a photoelectron traveling along the surface normal direction, and it increases to off-normal emission. The IMFP is a function of the electron kinetic energy (see eq. 3.4), and therefore it is different at each core-level. The advantage of choosing the shallow core-levels for this analysis is that all relevant core-levels are found within a short energy range in which the IMFP varies very slowly and can be considered constant. The IMFP of the electrons is estimated to be $2-3\,\mathrm{nm}$ for the energy of the measured core levels [74]. This leads to an increased surface sensitivity for measurements taken at high emission angles. Therefore, XPS core-level spectra taken at high emission angles yield depth-dependent information of the chemical composition.

In fig. 4.4 we show XPS spectra of the shallow core-level low binding energy excitations ($E_B < 80\,\mathrm{eV}$) measured at normal emission (red curve) and under 60° emission angle (black curve), using synchrotron radiation, with a photon energy of $h\nu = 1000\,\mathrm{eV}$ (beamline P04, PETRA III, DESY). In order to be able to quantitatively compare the data, the measurements were carried out with the same integration time. The normalization has been accomplished by the intensity above the Fermi level. Directly below the Fermi edge, in the range of approximately $E_B \in [5,0]\,\mathrm{eV}$, the photoemission signal originates from electrons emitted from the valence band (labeled VB). Right above this region, one finds the Bi 5d (24.5 eV and 27.5 eV), Sb 4d (32.4 eV and 33.9 eV) , Te 4d (39.9 eV and 41.5 eV) and Se 3d (53.2 eV and 54.1 eV) core-level peaks. All of them exhibit a splitting into two partner peaks caused by the spin-orbit interaction. This interaction breaks the degeneracy of states with different total angular momentum quantum number j, which are named accordingly. Thus, for a particular element or compound, the spin-orbit partners of each core-level show a characteristic energy speration, with a well defined spin-orbit splitting and a peak ratio proportional to the degeneracy of each multiplet, i.e. the 2j+1 number of states with different values of m_j. Their binding energies are summarized in table 4.1. A comparison to the binding energies of elemental Se, Bi and Te [123] points out a chemical shift of +0.5 eV for Bi 5d and Sb 4d, and -0.5 eV for Te 4d [123]. The opposite shifts in binding energy can be explained by a charge transfer from Bi/Sb to Te due to the chemical bond at the surface [134], whereas the similar shifts for Bi and Sb indicate an isoelectronic substitution of Sb by the Bi-doping. The position of the Se 3d states from the amorphous Se cap agree well with the values for elemental Se [123], as expected. But after decapping, there is a chemical shift of roughly -2.8 eV, showing a different valence state of Se at the surface of $(Bi,Sb)_2Te_3$. In addition to the core-level peaks, there are also very broad features at the high binding energy side of the main peaks. Those are due to characteristic energy losses of the electrons emitted from the respective core levels. Photoelectrons excited from core-levels at higher binding energies have a higher chance of losing energy for other lower

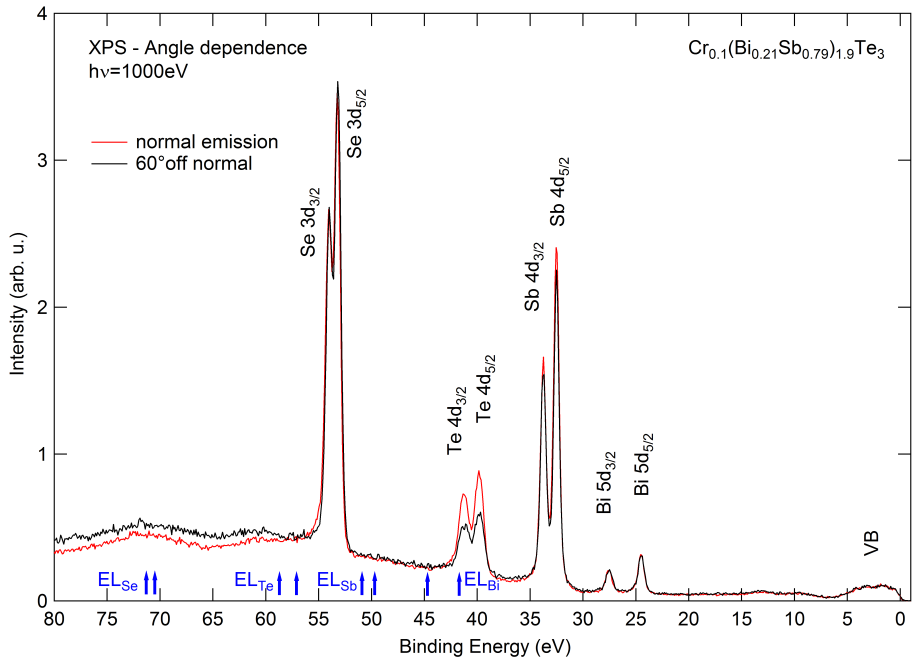

Figure 4.4: X-ray photoemission spectroscopy spectra comparison of the core levels of a $Cr_{0.1}(Bi_{0.21}\ Sb_{0.79})_{1.9}Te_3$ at normal and 60° emission angles (red and black curves, respectively). The angle-dependent intensity variations of the core-level peaks provides depth information of the constituent elements. The blue arrows and labels indicate the positions of the electron loss features of each core-level excitation.

Table 4.1: Binding energies of Se 3d, Te 4d, Sb 4d, Bi 5d, and core levels of $Cr_{0.1}(Bi_{0.21}Sb_{0.79})_{1.9}Te_3$ film compared to that extracted from ref. [123].

Core levels	Bi 5d		Sb 4d		Te 4d		Se 3d	
	5/2	3/2	5/2	3/2	5/2	3/2	5/2	3/2
Binding energies	24.5	27.5	32.5	33.7	39.9	41.5	53.3	54.1
Binding energies ref. [123]	24	27	33	33	41	42	56	57

energy collective elementary excitations, such as the oscillations of the free electron gas (plasmons). These scattering events contribute to the XPS background with particular energy-loss features. The distance between a core-level peak and their respective plasmon loss peaks is constant, and therefore they can be easily identified. For instance, in comparison with the Te 3d peak (fig. 4.6), one finds a clear plasmon peak at 17.2 eV above the main peak, as labeled in fig. 4.4 by arrows.

When measured at an angle of 60° (black curve), the intensity of the Bi 5d core level remains unchanged, while the Se 3d core level increases and the Sb 4d and Te 4d decrease. This observation indicates a Se-rich environment at the surface of the topological insulator films and a depletion of Te atoms at the surface. This is a

general observation, valid for both undoped, Cr- and V- doped samples.

In order to gain some quantitative insight into the depth information, the IMFP of the electrons has been considered. The obtained data, thus, indicates a gradient of Se and Te concentrations within the upper 2-3 quintuple layers. A likely explanation is the substitution of Te by Se atoms at the surface in the top quintuple layer of the film caused by the migration of Se atoms from the capping layer, which supplies a surplus of Se at the sample surface. $(V,Cr)_y(Bi_xSb_{1-x})_{2-y}Te_3$ has the same quintuple-layered structure of topological insulators [135, 136]. Both references determine the height of a quintuple layer, with a typical height of a quintuple layer (QL) about 10 Å, as also reported by Richardella et. al. [137].

For an estimation of the depth of the surface layer which contributes to the measured signals, the depth z of penetration of the photoelectrons is considered (eq. 3.5). The depth information z indicates the depth at which 95% of the electrons are excited. A comparison with Equation 3.5 shows that by tilting from $\theta = 0°$ to $\theta = 60°$, it decreases by half. In order to obtain absolute values for z, the IMPF is first determined by the TPP-2M equation (see equation 3.4). Since the IMFP mainly depends on the kinetic energy of the electrons and the considered core level excitations are in an energy interval in which the IMFP changes only slightly, the IMFP can be estimated uniformly as:

$$\lambda(Bi, Sb, Te, Se) \approx 30\text{Å} \tag{4.1}$$

The comparison of the calculated value with the so-called universal curve [138] shows a good agreement. The universal curve indicates the IMFP as a function of the kinetic energy of the photoelectrons, which has the same profile for all elements. Thus, the depth assessed by our emisison-angle dependence can be estimated as:

$$z(0°) = 90\,\text{Å} \approxeq 9.0\,QL, \tag{4.2a}$$

$$z(60°) = 45\,\text{Å} \approxeq 4.5\,QL. \tag{4.2b}$$

This allows an estimation of the number of quintuple layers in which the ratio of selenium to tellurium concentration changes to a maximum of 9 quintuple layers. The increase in the levels of selenium shows an accumulation of selenium on the surface of the sample. The additional simultaneous reduction of the levels of the tellurium indicates the displacement of tellurium atoms by selenium atoms in the surface-near layers of the sample. In comparison, the negligible relative changes in bismuth and antimony intensities confirm such a presumption. Three possible ways may lead to the substitution of selenium with tellurium: (i) during the vapor deposition process of the amorphous Selenium protection layer, (ii) during the

storage or (iii) during the decapping process, whereas the likely way is due to heating of the Selenium layer. As a result of the elevated temperatures and the additional available Selenium atoms in the protection layer, it is likely that the exchange takes place during this process. A further possible explanation of the increasing Selenium intensity is a monatomic layer of amorphous selenium, which is too strongly bound to the layer structure of the topological $(V,Cr)_y(Bi_xSb_{1-x})_{2-y}Te_3$ and does not dissolve by heating the sample during the preparation. The Se 3d core levels of amorphous Se-protective layer are at a higher binding energy than the bound in the film selenium atoms. In the case of a residual layer of the amorphous selenium, a shifting of the intensity should also be shown at an angle, which is not observed here. An additional atomic layer selenium should also equally lead to the weakening of the core levels of tellurium and bismuth. Since this is not the case, the scenario of the remaining layer of selenium is unlikely to happen.

For a quantitative estimation of the stoichiometry, let us explain in detail each step of the analysis. In Fig 4.5 the normal-emission spectrum from fig. 4.4 is shown in more detail (black curve), in the range from 20 eV to 60 eV. First of all, the background originated from electrons that suffered multiple losses must be modeled and removed. For this low binding energy range, the assumption of a Shirley background (green curve) is fairly reasonable, where most of the electron energy losses occur at the core-level maximum. After subtraction of the Shirley background, the corrected spectrum (red curve) is obtained, representing the contribution of single-scattered photoelectrons, i.e. the intrinsic lineshapes of the core-levels. Each core-level is split in two spin-orbit partners and have been therefore fitted by two Voigt profiles (blue curves). Since all the electrons that contribute to the signals originate from d-orbitals, the intensity of the profiles is set to the ratio h(X 3/2):h(X 5/2) = 2:3 for the intensity ratio, analogous to equation 3.32, X = Bi, Sb, Te, Se. The size of the spin-orbit splittings are very close to those of the elemental species, which are well-known from the literature: Δ_{SO}(Bi) = 3.1 eV [139], Δ_{SO}(Sb) = 1.25 eV [140], Δ_{SO}(Te) = 1.4 eV [125] and Δ_{SO}(Se) = 0.8 eV [141]. In addition, based on the assumption that each core-level signal results in a characteristic loss feature, the loss-line intensities were scaled by the width of the respective core-levels, whereas the distance between the main peak and the loss line for the three elements were left as free parameters. The best fit value for the loss-line position was E(loss line)-E(core level) = 17.4 eV.

The relative element concentrations can be obtained from the best fit of the individual peak areas, by use of the equation 3.3 The relative cross sections σ_{rel} are taken from [132], taking the IMFP into account according to the TPP-2M equation 3.4. The best fit values are listed in table 4.2. In order to calculate the total intensity of the core-level lines, the sum of the areas of the characteristic core-level peaks was considered. For a sample with nominal formula $(Bi_{0.21}Sb_{0.79})_2Te_3$, the following

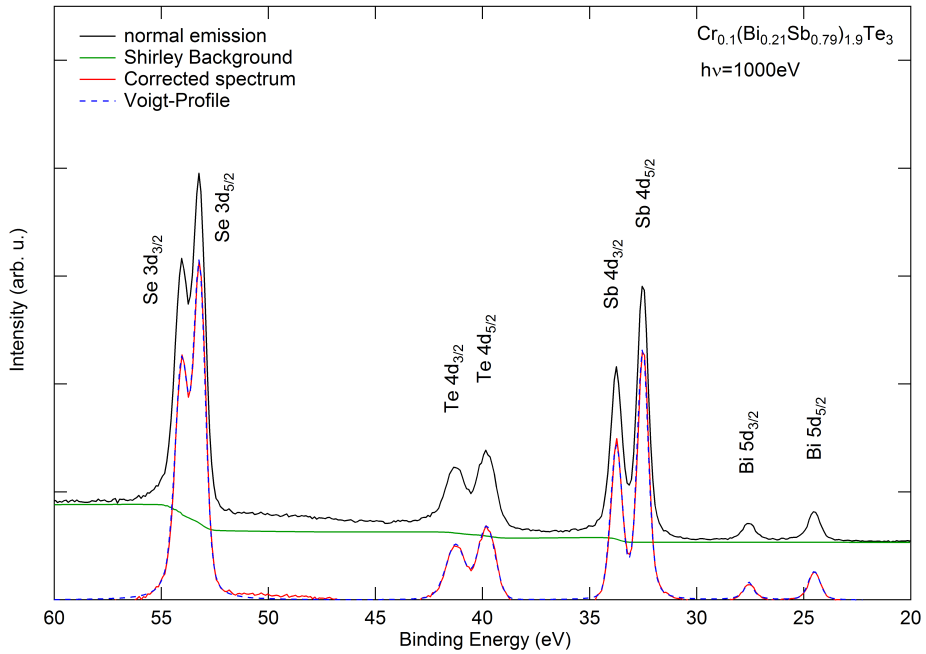

Figure 4.5: Quantitative analysis of the core-level spectrum for the topological insulator $Cr_{0.1}(Bi_{0.21}Sb_{0.79})_{1.9}Te_3$ at low binding energies, taken at $h\nu$ = 1000 eV. The measured spectrum (black curve) has already been corrected from the satellite lines. A Shirley background [124] (green curve) was assumed and subtracted from the experimental spectrum, resulting in a spectrum with the intrinsic core-level lineshapes (red curve). Subsequently, Voigt peaks were fitted to the individual signals (blue dashed line).

stoichiometries are obtained for the different emission angles considered:

(θ=0°): Bi(0.25) Sb(1.69) Te(3.05)
(θ=60°): Bi(0.24) Sb(1.66) Te(3.09)

where the total number of atoms was set to five.

The angle-dependence of the stoichiometry confirms the qualitative observation. At a constant proportion of bismuth in the sample, the selenium content which is on the surface, will increases, while the tellurium is reduced. The concentration of the Antimony is greater than the expected. The rising in the Antimony can be explained because of the ratios calculation procedure by the sum of the areas of the core levels and the electron loss. the same thing will be true for the Te 4d core level and loss peaks of bismuth. The oxide of the bismuth level is about 25.9 eV [139], and its at at 44.6 eV for tellurium oxide [142]. Which is not in our case. However, there are deviations between the sample measured in normal emission and the tilted sample. The calculation of the stoichiometry is subject to uncertainties.These are mainly

Table 4.2: Values of the relative cross-sections [132] and IMFP (λ), calculated by eq. 3.4, for the core-levels used for estimation of the relative atomic ratio of the constituent elements for $Cr_{0.1}(Bi_{0.21}Sb_{0.79})_{1.9}Te_3$ films.

	σ_{rel}	$\lambda(E_{kin})$ / Å
Bi 5d	0.077	23.18
Sb 4d	0.1054	22.46
Te 4d	0.1204	22.04
Se 3d	0.099	21.37

from uncertainties in the adjustment of the background and the consideration of the loss of electrons. The full width at half maximum of the loss peaks was determined in the range (5.3, 7.6) eV. The large fluctuation of the values leads to errors in the determination of the areas under the loss lines, as well as under the core levels and thus resulting in errors of the calculated ratio.

Despite of the clear presence of selenium at the surface, the nominal stoichiometry of the samples is apparently only slightly affected. This means that the Se-rich stoichiometry of the surface stem from remaining selenium islands strongly bound to the top surface of the film, resulting in a different selenium species than that from the original capping layer. The thermal decapping method does not allow the complete removal of the selenium cap, which strongly changes the chemical composition and the electronic properties of the film surface. These changes are expected to also affect the optical properties of the surface. The decapping method should be optimized, in such a way to keep the pristine quality of the film surface.

4.3 Electron energy loss spectroscopy in $(V,Cr)_y(Bi_{0.21}Sb_{0.79})_{2-y}Te_3$

As discussed in the last session, a thorough determination of the loss energy background is a very important step in the quantitative chemical analysis of core-level spectra by XPS. This is a rather complex task that is usually out of the scope of most studies, especially in the low binding energy range discussed previously. However, when analyzing deeper core levels, this problem cannot be easily circumvented by simple assumptions, since the probability of multiple scattering of the excited photoelectrons is higher. In fig. 4.6, detail measurements of the main core-levels of the constituent elements (Bi 4f, Se 3d, Te 3d and Sb 3d) are shown for $h\nu$ = 750 eV. At the higher binding energy side of the main peaks there are broad peaks, marked by thick arrows, that point out the position of the main plasmon loss features. In this case, the assumption of a Shirley background is an oversimplified one, and the exact

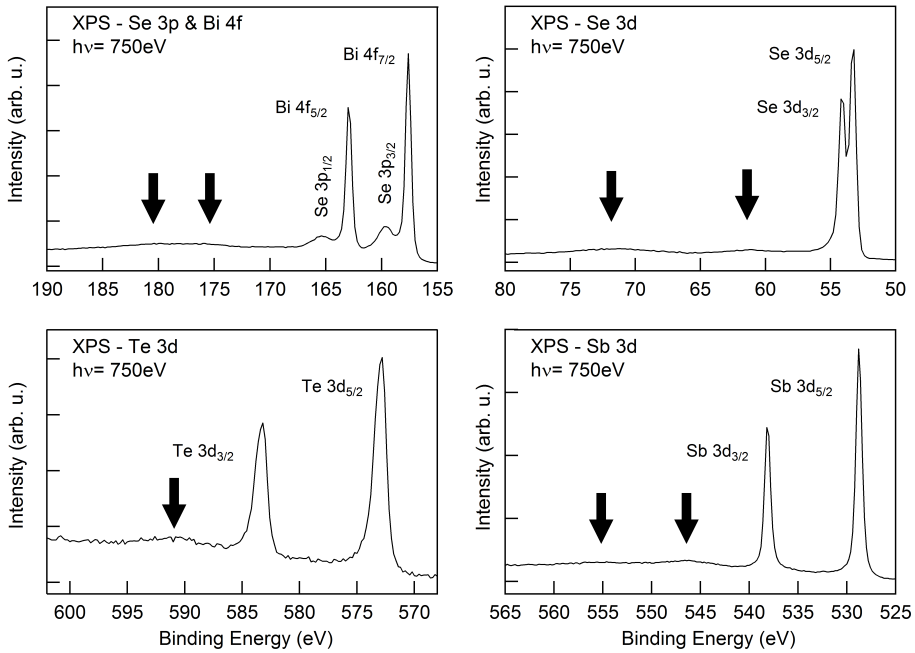

Figure 4.6: X-ray photoemission spectra of Se 3p and Bi 4f (top left), Se 3d (top right), Te 3d (bottom left) and Sb 3d (bottom right) from a $V_{0.1}(Bi_{0.21}Sb_{0.79})_{1.9}Te_3$ thin film, measured at a photon energy $h\nu$ = 750 eV. The inelastic background contains the main energy-loss signatures of the system (marked by black arrows) at the high binding energy side of the core-level peaks.

determination of the energy loss spectrum is required. In this session this problem is tackled by means of reflective electron energy loss spectroscopy (REELS).

To illustrate this, figure 4.7 shows the XPS spectrum of Sb 3d core-levels from a $(Bi_{0.21}Sb_{0.79})_2Te_3$ thin film (full black curve). The spectrum was processed using a Shirley-background (dashed curve) in order to remove the low-energy inelastic scattering contributions. Obviously the Shirley method did not remove all loss features in the in the high binding energy side of the spectrum (full red curve) [124].

Nevertheless, a preliminary attempt to directly extract the energy-loss function from the XPS backgrounds from the spectrum in fig. 4.8 with the aid of a theoretical model provided by Tougaard et al. in the literature [85] and implemented in the Tougaard Queels software [92]. In the model, the XPS background is fitted by a theoretical inelastic cross-section λK(E) based on a superposition of Drude-Lorentz oscillators describing the plasmon modes of a homogeneous medium. At first, four oscillators were assumed at loss-energies 3 eV, 7 eV , 19 eV and 28 eV. The next step was to calculate the effective cross-sections for electrons that are backscattered at different depths, by means the equation 3.51. From the cross-sections calculated in the previous step, inelastic cross-section for a homogeneous medium is computed,

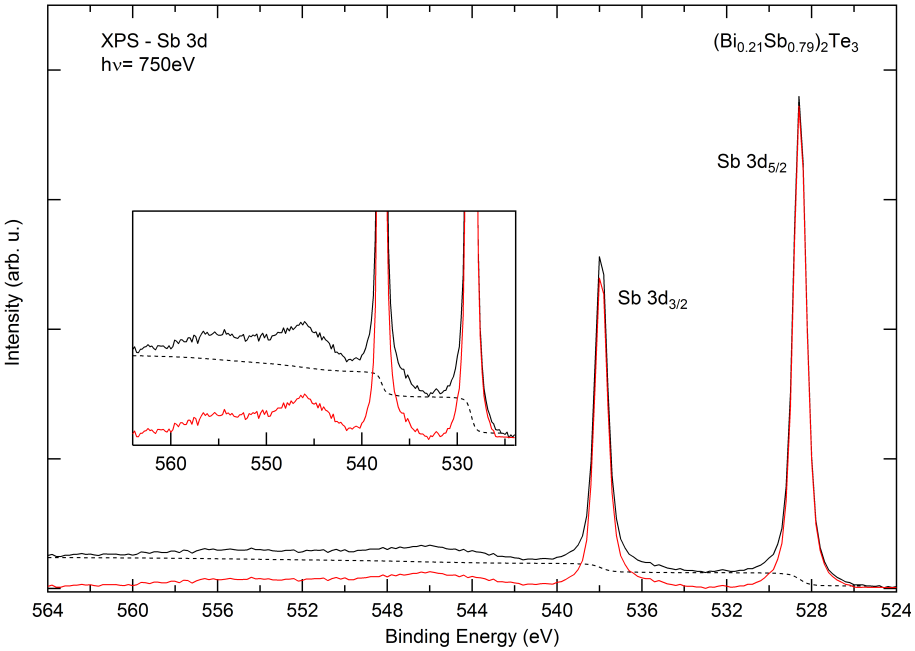

Figure 4.7: Shirley-background analysis of Sb 3d XPS peaks from a $(Bi_{0.21}Sb_{0.79})_2Te_3$ topological insulator thin film measured at $h\nu$ = 750 eV (P04, PETRA III, DESY). The original XPS spectrum (black curve) is plotted with the Shirley-background lineshape (dashed curve) and the resulting corrected spectrum (red curve). It is obvious that the analysis did not remove all loss features.

and it is shown in fig. 4.8a . Subsequently the calculated loss spectrum was applied to the background subtraction from the Sb 3d spectrum from fig. 4.6 again, showing a much better result (see fig. 4.8b). This shows that a precise modeling of the energy-loss spectrum is a much more reliable method for the treatment of XPS backgrounds. One step further in the direction of a realistic background treatment is the experimental determination of the energy-loss spectrum by means of EELS measurements. This method applies the Tougaard analysis directly on real REELS experimental data, allowing one to extract the real optical properties of the system.

EELS can directly probe the characteristic energy-loss excitations of a system, e.g. interband transitions, multiple scattering and plasmon excitations. With a variable energy electron source in the range of 100 to 1000 eV, the surface sensitivity can be tuned in the nanometer region. EEL-spectra were measured at energies varying from 100 to 1000 eV, for a fixed scattering geometry of an incident angle $\theta_i = 56°$ and exit angle $\theta_o = 64°$, i.e. close to the specular geometry ($\theta_i = \theta_o = 60°$). Figure 4.9 shows a typical REELS spectrum (full black curve) of a $V_{0.1}(Bi_{0.21}Sb_{0.79})_{1.9}Te_3$ topological insulator thin film, measured with a primary energy E_0 = 300 eV, plotted against the kinetic energy of the scattered electrons. The spectrum can be separated

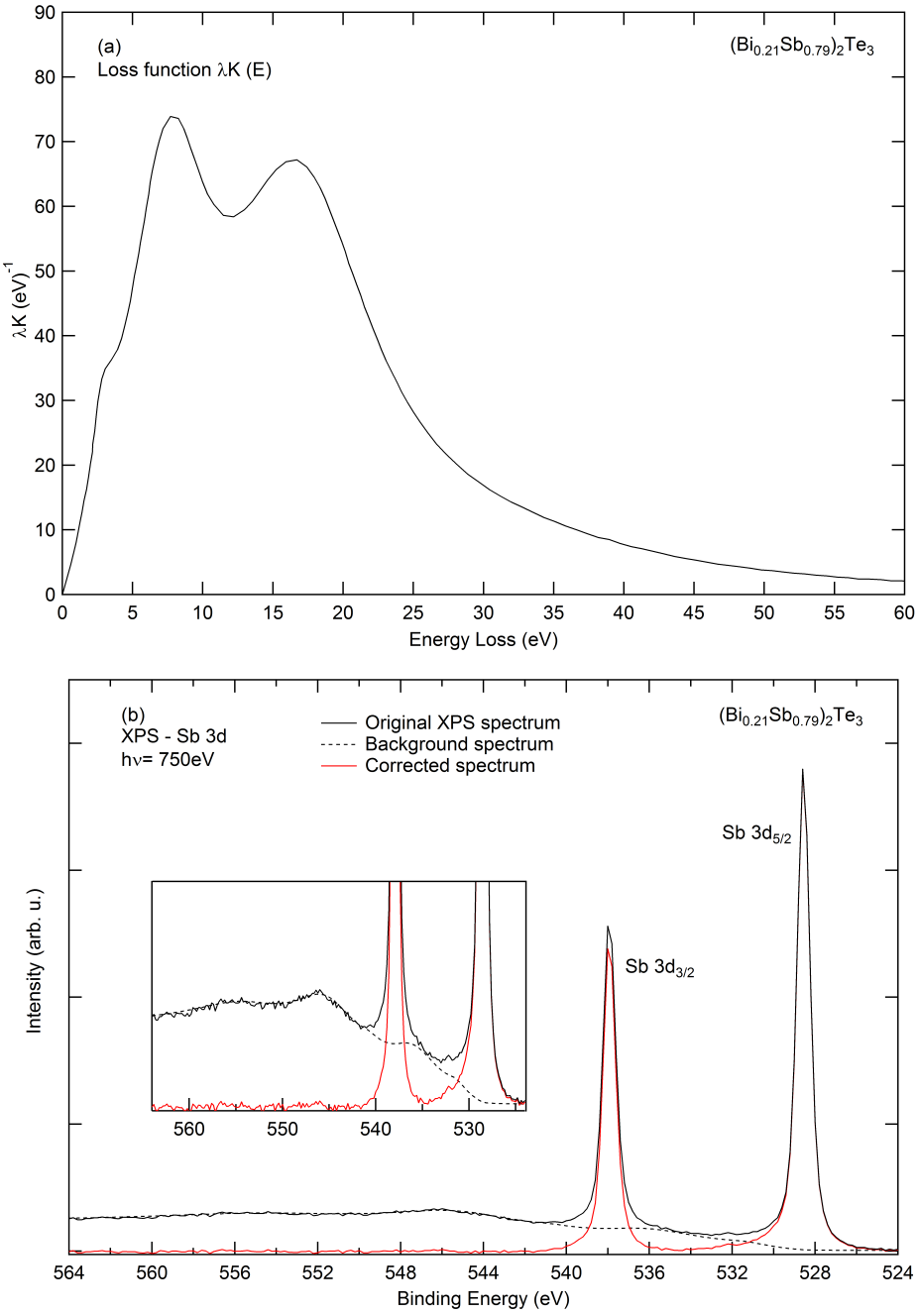

Figure 4.8: a) The resulting effective inelastic cross sections λK(E) of a topological insulator $(Bi_{0.21}Sb_{0.79})_2Te_3$ thin film sample based on XPS spectrum in (b) at $h\nu$ = 750 eV. b) Inelastic Background analysis of Sb 3d peak for the same sample. The original XPS spectra (black curve) is plotted together with the background lineshape (dashed curve) based in the loss function λK(E) from figure (a) and the corrected spectrum (red curve) resulted from analysis.

into two regions. The first part consists of the elastically scattered electrons, forming the prominent peak centered at 300 eV, the so-called zero-loss peak (Rayleigh line). The second region of the spectra is the long tail at lower kinetic energy, caused by the inelastically scattered electrons, exhibiting much lower intensity as the elastic peak. In order to highlight this structure, the inelastic region is magnified by a factor of 5 in fig 4.9. This region starts at the excitonic band gap and contains characteristic single scattering excitations, as well as multiple-scattered electrons. For the quantitative analysis of REELS spectra, the multiple-scattering contribution must be removed, as discussed in section 3.4. This contribution increases with the loss-energy and dominates the spectra at energy-loss above 25 eV.

The removal of the multiple-scattering contribution follows the approach described in ref. [143] and is based on a recursive algorithm developed by Tougaard and Chorkendorff was used, which provides λK(E), the experimental single cross-section K multiplied by the inelastic mean free path λ as a function of the energy loss (E) [92, 99, 121]. The resulting spectrum shown as a red curve in fig. 4.9, in which the elastic peak has also been removed, representing the inelastic cross-section λK(E). One notices that when considering only single-scattering events, the inelastic cross-section should converge to zero for higher energy-loss.

Subsequently, the elastic peak has to be accurately subtracted from the REELS spectrum [143]. Hence different approaches can be found in the literature, e.g. subtraction of a power law, a mirrored Rayleigh line or a fitted logarithmic tail, deconvolution of the elastic peak or fitting Voigt profiles [121, 143–145]. In this work, a split-Voigt profile was used to account the for the asymmetric lineshape of the Rayleigh line. This is due to a non-uniform thermal distribution of the electrons in the energy region of the elastically scattered electrons. The thus determined FWHM of the Rayleigh line is 460 ± 40 meV.

The theoretical λK(E) is calculated by applying the recursive equation 3.45. It should be noted that λK(E) is area-normalized in order to fulfill the Kramers-Kronig sum rule [90, 91, 97]. This normalization is accomplished by processing λK(E) with the equation 3.46. That means the area of the cross section curve should typically be in the range $0.7 - 0.95$ eV (see section 3.4). For each sample three oscillators were used to describe the plasmon modes that determine the lineshape of the inelastic scattering cross-sections. Each oscillator is modeled by a peak described by eq. 3.49, defined by the input parameters A_i, $\hbar\omega_i$, $\hbar\beta_i$ and α_i. The values of the parameters hω_i, $\hbar\beta_i$ and α_i that respectively describe the energy, damping and dispersion of each oscillators are listed in table 4.3 for a $(Bi_{0.21}Sb_{0.79})_2Te_3$ sample. These parameters are crucial to determine the lineshape of the inelastic scattering cross sections. A dispersion coefficient $\alpha_i = 1$ is used for all thin film samples, since this value is typically used for narrow band-gap materials [102, 103]. The corresponding

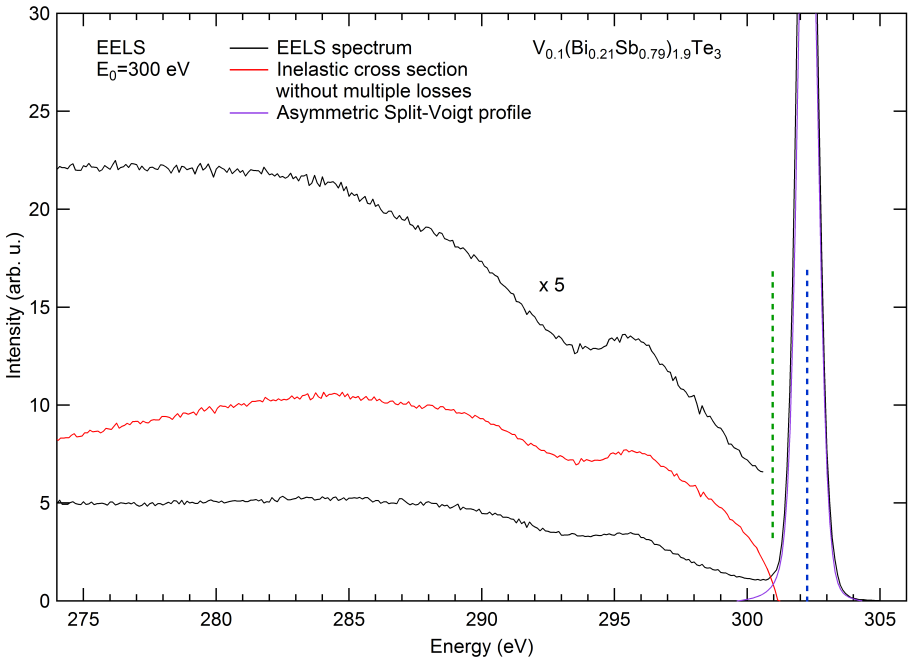

Figure 4.9: Electron energy loss spectrum (full black line) of a $V_{0.1}(Bi_{0.21}Sb_{0.79})_{1.9}Te_3$ topological insulator thin film, measured at E_0 = 300 eV, illustrating the elastic peak centered at 300 eV (marked by the dashed blue line), and the inelastic spectrum at lower kinetic energies (also five times magnified). The elastic peak was fitted by an asymmetric Spli-Voigt lineshape (full violet curve) with a FWHM of 460 $\pm$ 40 meV. The red curve represents the inelastic cross-section after removal of the multiple-scattering losses. The dashed green line marks the cut-off of the inelastic cross-section at the border of the excitonic bandgap.

parameters for all the oscillators are derived via trial and error procedure until a good agreement between the experimental and the simulated inelastic scattering cross section λK(E) is found. The best-fit models of λK(E) are plotted as red curves in figure 4.11 on top of the corresponding experimental λK(E) (black curves) obtained from REELS spectra taken at E_0 = 300 eV (top panel), 500 eV (middle panel) and 700 eV (bottom panel) from a $V_{0.1}(Bi_{0.21}Sb_{0.79})_{1.9}Te_3$ thin film. One can identify three broad maxima, respectively centered at 6 eV, 13 eV and 18 eV. The theoretical and experimental λK(E) for TI thin film samples show a good agreement, as well as with the energy-loss spectra from Sb_2Se_3 reported in the literature (see section 2.4) [47, 48, 58] (see figs. 2.7, 2.9 and 2.6).

The procedures described above were applied to REELS measurements for $(Bi_{0.21}Sb_{0.79})_2Te_3$ thin films doped with vanadium or chromium, as well as for undoped samples, grown on different substrates [Si(111) and InP(111)], for primary energies ranging from 100 to 1000 eV. The results were similar for samples with

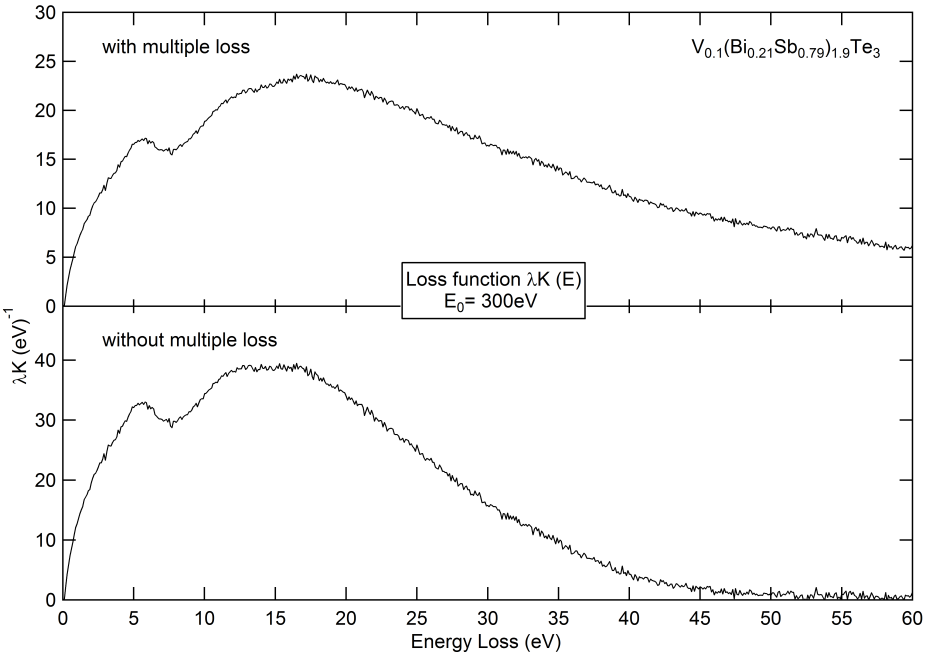

Figure 4.10: The loss function λK(E) of a $V_{0.1}(Bi_{0.21}Sb_{0.79})_{1.9}Te_3$ topological insulator sample extracted from the experimental EELS data measured at E_0 = 300 eV primary electron energy with before (top panel) and after (bottom panel) the removal of the multiple losses. Single-scattering events are bound to low energy-loss.

Table 4.3: Best-fit parameters of the Drude-Lorentz oscillator model for the $(Bi_{0.21}Sb_{0.79})_2Te_3$ topological insulator thin film for EELS spectra measured at different primary energies $E_0 = 300$, 500 and 700 eV.

Primary Energy (E_0)	Excitation Energy (eV) $\hbar\omega_i$	Oscillator Strength (eV^2) A_i	Damping Coefficient (eV) $\hbar\beta_i$	Dispersion α_i	Area
300 eV	5.9	5.05	6	1	30.3
	13.5	9.37	7	1	65.59
	23.2	405.18	15	1	6077.7
500 eV	5.75	4.27	6	1	25.62
	13.5	8.1	8	1	64.8
	22.9	406.3	13	1	5281.9
700 eV	5.1	2.92	5	1	14.6
	13.5	5.47	8.5	1	46.49
	22.5	407.8	11.6	1	4730.5

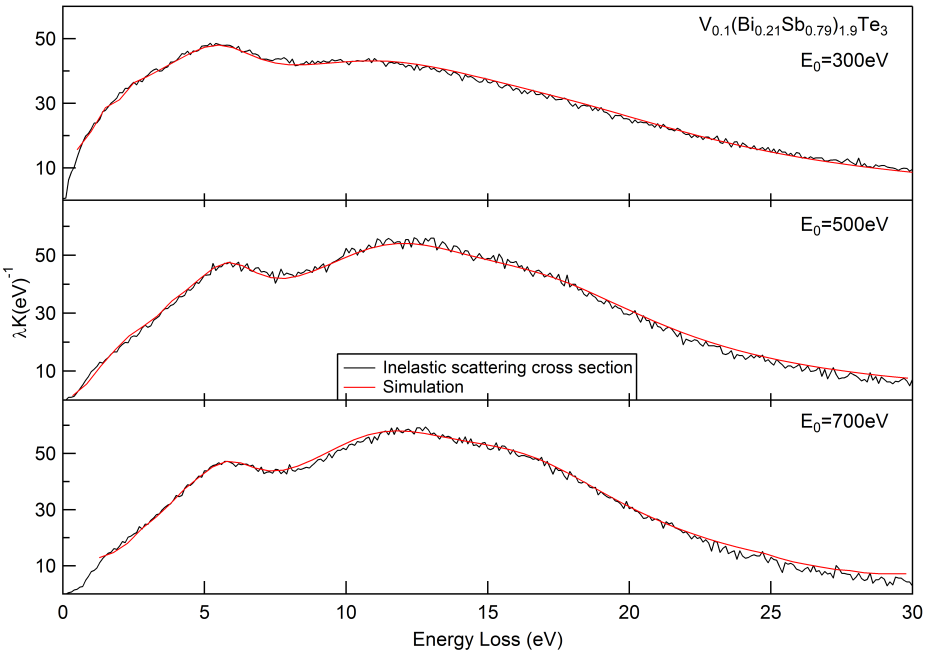

Figure 4.11: The inelastic scattering cross-sections extracted from the EELS-spectra of the $V_{0.1}(Bi_{0.21}Sb_{0.79})_{1.9}Te_3$ topological insulator film (black curves), measured for different E_0 = 300 eV (top panel), 500 eV (middle panel) and 700 eV (bottom panel). Their respective theoretically calculated cross- sections λK(E) based on the Drude-Lorentz oscillator model (red cruves) show good agreement with the experiments. Three broad maxima are found at 6 eV, 13 eV and 18 eV, in good agreement with Sb_2Se_3[47, 48, 58].

different compositions, but differed mostly as a function of primary energy. For instance, the results for $V_{0.1}(Bi_{0.21}Sb_{0.79})_{1.9}Te_3$ are shown in fig. 4.12, for primary energies E_0 of 100 eV, 150 eV, 300 eV, 500 eV and 700 eV. Three plasmons modes are identified and, in general, it has been noticed that:

- The first oscillator (red range in fig. 4.12) lies between 5.1 $\sim$ 6.3 eV while its strength of about 1.4 $\sim$ 5.2 eV^2, and the damping coefficient range 2.7 $\sim$ 6.5 eV, whereas the area 1.5 $\sim$ 30.

- The second oscillator (green range in fig. 4.12), the excitation energy between 12.5 $\sim$ 16.9 eV while its strength of about 5.4 $\sim$ 9.5 eV^2, and the damping coefficient range 8 $\sim$ 13 eV, whereas the area 45 $\sim$ 102.

- The third oscillator, the excitation energy between 19 $\sim$ 24.5 eV while its strength of about 324 $\sim$ 455 eV^2, and the damping coefficient range 10 $\sim$ 15 eV, whereas the area 3890 $\sim$ 6100.

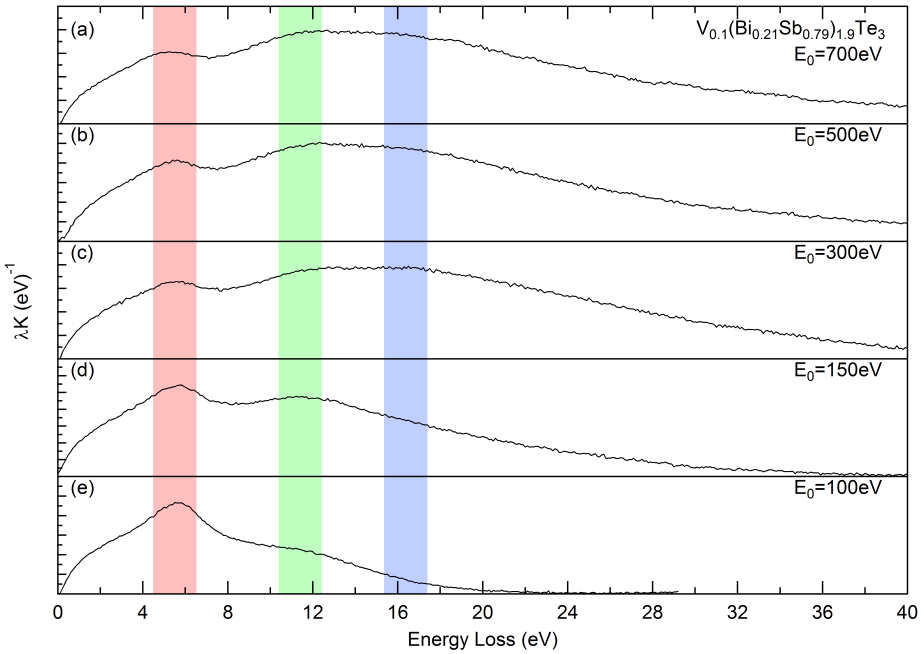

Figure 4.12: The inelastic electron cross-section (black curve) derived from EELS experiments at $V_{0.1}(Bi_{0.21}Sb_{0.79})_{1.9}Te_3$ topological insulator thin films, for primary energies (a) 700 eV, (b) 500 eV, (c) 300 eV, (d) 150 eV and (e) 100 eV, showing the ranges of the three main plasmon modes. The red colored stripes represent the position of the surface plasmons, while the green and blue colored stripes denote the bulk plasmon modes.

Losses lower than 8 eV mainly originate from single electron processes such as interband transitions [45–47] as the number of electrons participating at plasma oscillations is too small below that energy [146]. The spectral feature at 12 eV and 16 eV have been interpreted respectively as surface and volume plasmons in $(Bi_{0.21}Sb_{0.79})_2Te_3$ [47, 48, 58] see figs. 2.7, 2.9 and 2.6. In this work it is found that the intensity of both spectral features at 12 and 16 eV increase with increasing primary energy, indicating that both spectral features are volume excitations. Consequently, the interpretation of the spectral feature at 12 eV as surface plasmon appears to be incorrect [47] (see fig. 2.6). On the other hand, the spectral feature at 5.5 eV remains at constant strength with increasing primary energy, as expected of surface plasmons, which is in agreement with the literature [47, 48, 58] explained extensively in chapter 2.4.

Now one can proceed with the correction of the XPS background, using the modeled λK(E), and with the derivation of the optical properties. In fig. 4.12 the same core-level spectra from fig. 4.8 are shown, now with the background correction using the modeled λK(E) from fig. 4.12. The results show a clearly better treatment

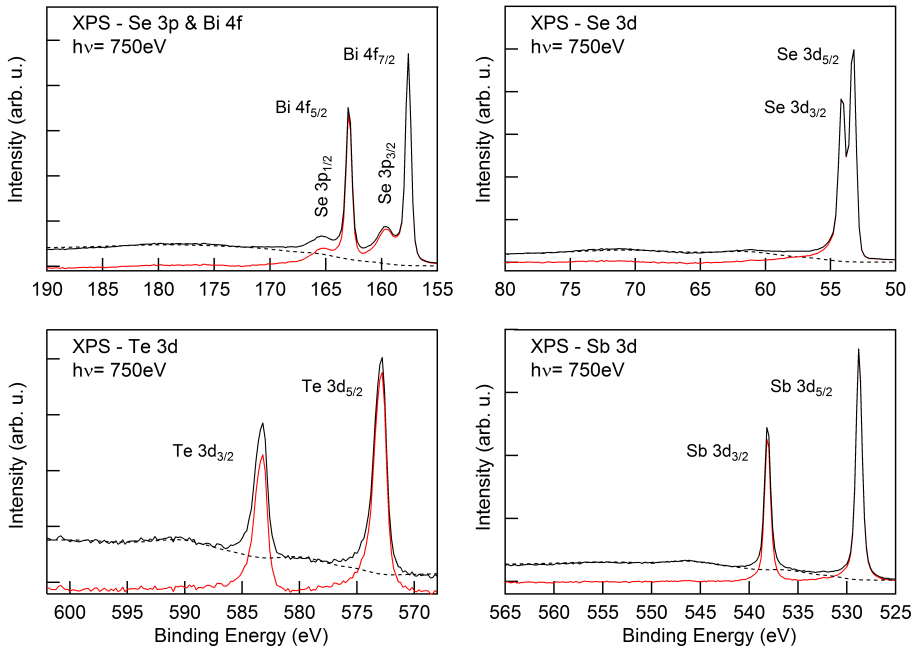

Figure 4.13: Inelastic background analysis of (top left) Se3p, Bi 4f, (top right) Sb 3d, (bottom left) Te 3d and (bottom right) Sb 3d peaks measured at $h\nu$ = 750 eV for a $V_{0.1}(Bi_{0.21}Sb_{0.79})_{1.9}Te_3$ thin film. The original XPS spectra (black curve) are plotted together with the inelastic background derived from EELS spectra by means of the Drude-Lorentz oscilator model (dashed curve) and the corrected spectra resulted from the analysis (red curve). This more realistic approach shows a much better result for removing the plasmon peaks.

of the plasmon peaks at the high binding energy side of the core-level peaks as the previous approaches.

In the following session the inelastic cross-sections obtained by the application of the Drude-Lorentz model to the EELS experimental data are used for calculating the high-energy optical properties of the topological insulator samples by means of the Kramers-Kronig transformations.

4.3.1 Energy loss function and surface energy loss function

The single-scattering loss cross-section λK(E) is closely related to the complex dielectric function ε via the bulk electron loss function $\mathrm{Im}\left[-\frac{1}{\varepsilon(\hbar\omega)}\right]$ [101, 147]. Using only very low primary electron energies, the REELS spectrum becomes very surface sensitive, due to the short inelastic mean free path of the electrons [71, 74]. In this case, the effects of the surface must be taken into account in terms of the surface electron loss function (SELF)= $\mathrm{Im}\left[-\frac{1}{1+\varepsilon(\hbar\omega)}\right]$, as well as the interference between

the bulk and surface processes [85, 100, 148]. In the electron energy range used here (100 to 1000 eV), this expression must be expanded to include also surface effects, but this is more complicated than a simple linear combination of the SELF and the ELF [100]. The time varying electric field induced by the moving electrons leads to electronic excitations in the material. This field is modified when the electrons move near to the surface and the electrons can even lose energy although moving outside the material as they still induce charge redistribution into the material [149]. Therefore, any interference between the bulk and surface excitations must be taken into account. Yubero and Tougaard suggested a semi-classical model for the dielectric response function including all these effects, which is implemented in the QUEELS-$\varepsilon(\kappa,\omega)$-REELS software package [85, 100]. Here the dielectric function is given in terms of ELF and SELF, which are approximated by a sum of Drude-Lorentz oscillators [96, 149]. Figure 4.14 shows the bulk ELF (top panel) and the SELF (bottom panel) of a $(Bi_{0.21}Sb_{0.79})_2Te_3$ topological insulator thin film obtained from an EELS spectrum measured at E_0 = 300 eV. A maximum at 22.5 eV is observed in the bulk ELF, whereas the SELF exhibits three maxima at 6 eV, 11.8 eV and 17 eV, which are respectively connected to one surface and two bulk plasmon modes. The observations by Greenaway et. al. shows a peak appears at 6 eV (see fig. 2.5) in chapter 2.4, which is also noticeable in the (top panel) in fig. 4.14. Greenaway's measurements covers the range of $(0.1 - 12\,\text{eV})$, thus the largest peak which raise at 22.5 eV it did not appear in fig. 2.5. Previously in section 3.2 mentioned electrons lose energy due to inelastic scattering processes when moving through a medium. Various types of excitations are possible either single or collective. In interband transitions or ionization processes only a single electron participates [147]. Plasmon losses are a collective resonant oscillation of the whole electronic system which mainly occur at loss energies lower then 30 eV [87]. Bulk plasmons have a oscillation frequency $\omega_p = \sqrt{\frac{4\pi ne^2}{m}}$ (n is the charge carrier, m is electron mass) whereas the frequency of a corresponding surface plasmon is $\omega_{sp} = \frac{\omega}{\sqrt{2}}$ [101]. A plasmon oscillation is longitudinal and can therefore only occur when the real part of the dielectric function $\varepsilon_1 = 0$ and the imaginary part of the dielectric function ε_2 does not have a maximum at the same energy [150], as depicted in fig. 3.4. Due to the zero crossing of ε_1 the ELF will have a maximum at this energy indicating a bulk plasmon. For a surface plasmon ε_1 must equal -1 and at the same energies the SELF will exhibit a maximum [146]. The plasmon energy changes due to interference with oxide or in this case the selenium layer [151]. Furthermore, multiple scattering can occur, where one electron excites more than one of the above stated processes.

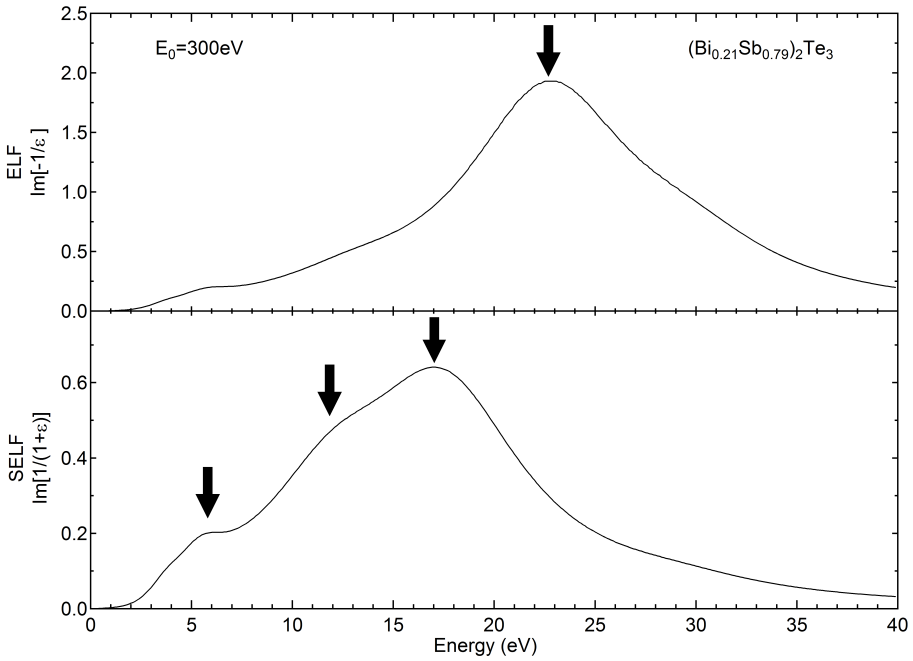

Figure 4.14: (top panel) ELF Im$\left[-\frac{1}{\varepsilon(\hbar\omega)}\right]$ and (bottom panel) SELF Im$\left[-\frac{1}{1+\varepsilon(\hbar\omega)}\right]$ of a $(Bi_{0.21}Sb_{0.79})_2Te_3$ topological insulator thin film from an EELS spectrum measured at 300 eV. The bulk ELF shows a maximum at 22.5 eV, whereas the SELF shows a surface plasmon at 6 eV and two plasmons at 11.8 eV and 17 eV, respectively.

4.3.2 Real and imaginary parts of dielectric constant

Knowledge of ELF leads to the real and imaginary parts of ε. Figure 4.15 represent the dielectric function of in its two parts the real and the imaginary, for a topological insulator $(Bi_{0.21}Sb_{0.79})_2Te_3$ at different primary energies. There are two spectral features: a low-energy peak at 6 eV and a split high-energy peak located at 24 eV. These features as low- and high-energy plasmon can be relate respectively. The first, low-energy, zero is caused by transitions within the overlapping p bands of the TI components, while the second zero occurs after the respective s bands get involved as well. In figure 4.15 ε_1 pass the zero at ~ 6 and ~ 21.6 eV accompanied by a decreasing ε_2. This gives rise to the maxima in the volume loss function (Im$\left[\frac{1}{\varepsilon}\right]$) at the energies of ~ 6 and 22.5 eV, characteristic of volume plasmon excitations. Further inspection of the absorption features ε_2 in fig. 4.15 also reveals a peak spanning from 8 to 12 eV , which occurs as a result of the interband-transition excitations (e.g., contribution of Bi 6s electrons) [47, 48].

As mentioned in section 3.3 the real and the imaginary parts of the dielectric function is in dependence of the frequency ω as shown if fig. 3.4. Figure 4.15 shows also the lower value ε_0 (see table 4.4) for the experimental dielectric function of

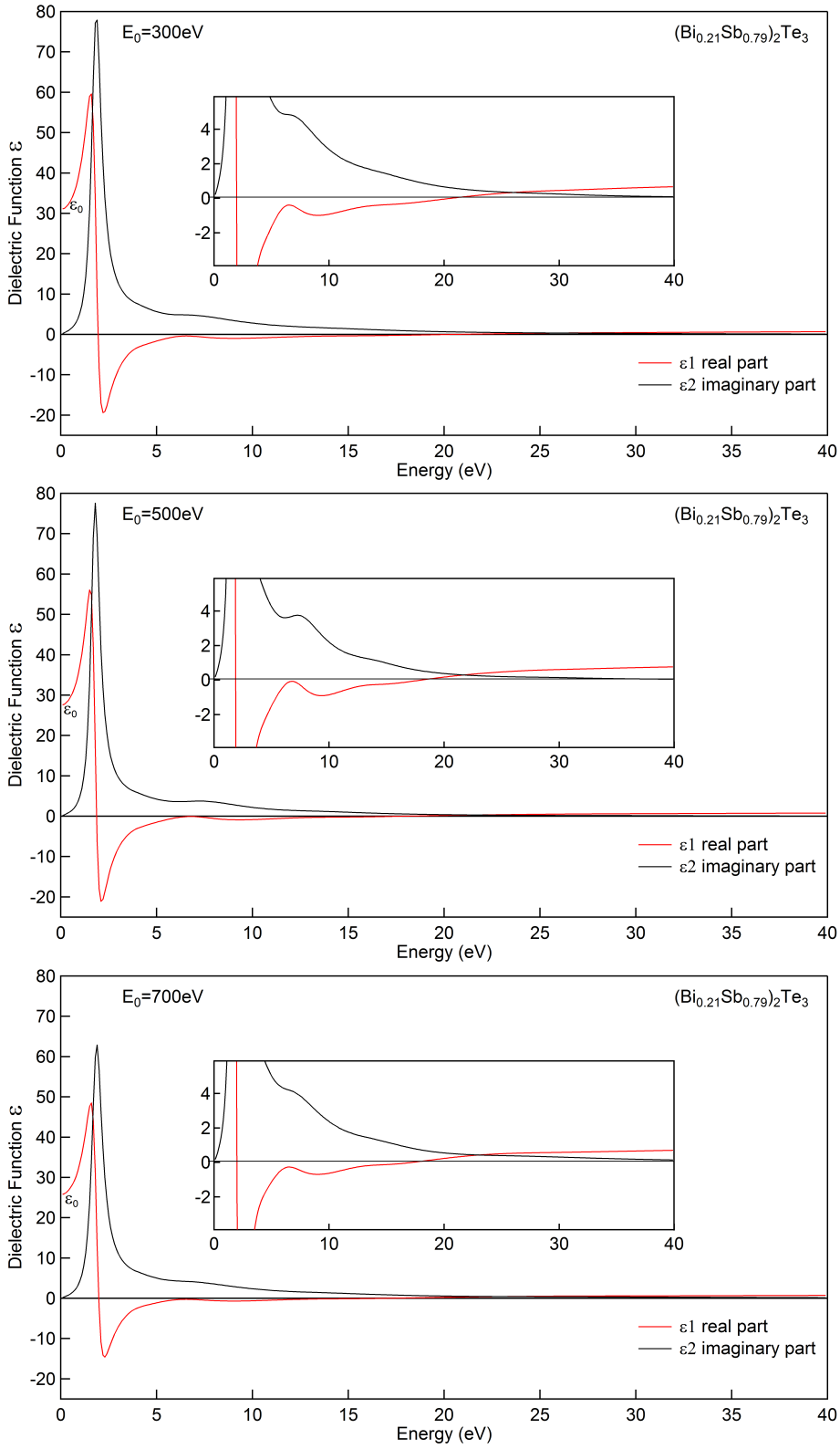

Figure 4.15: Real part ε_1 (—) and imaginary part ε_2 (—) of dielectric function of the topological insulator thin film $(Bi_{0.21}Sb_{0.79})_2Te_3$ for $E_0 = 300$, 500 and 700 eV primary electron energies.

Table 4.4: Shows the lower values ε_0 extracted from the experimental data of the real part of the dielectric function for the topological insulator thin film $(Bi_{0.21}Sb_{0.79})_2Te_3$ for $E_0 = 300$, 500 and 700 eV primary electron energies.

Primary energy (eV)	Lower value of the real part ε_0
300	32
500	28
700	26

$(Bi_{0.21}Sb_{0.79})_2Te_3$. It is obvious that the values of the ε_0 are decreases with increasing of the primary energy E_0, due to the reduce in the interband transitions with rising of the primary energy [45]. Furthermore, in comparison to the values of ε_0 in fig. 2.5 (a) measured by Greenaway et. al. for Bi_2Te_3 [45]. It is possible to say that the behavior of the dielectric function in fig. 4.15 and fig. 2.5 are convergent. Also the lower value of the real part in fig. 4.16a, the Bi_2Sb_3 had a close value to that in table 4.4.

The low energy plasmon in fig. 2.5 (a) for Bi_2Te_3 appears at $6 - 7$ eV which is very comparable to the low energy plasmon arise in the experimental real part of the dielectric function for $(Bi_{0.21}Sb_{0.79})_2Te_3$ in fig. 4.15. Moreover the maximum value of ε for the real and the imaginary parts has relative value to what observed in fig. 4.15. Reijnders et. al. shows a comparable value of ε_0 to what observed in this dissertation As mentioned in chapter 2.4, Yin et. al. theoretically calculated through density functional theory (DFT) with local density approximation and Quantum ESPRESSO code, the real and the imaginary parts of the dielectric function for [59]. A noticeable match can be observed between the experimental data shown in fig. 4.15 and the theoretical real and imaginary for Sb_2Te_3 and Bi_2Te_3. Back to fig. 2.10, in general the experimental observation of Yin et. al. shows a comparable behavior Sb_2Te_3 and Bi_2Te_3, while it is not for the Bi_2Se_3 [59]. Furthermore Yin et. al. shows a low energy plasmon at $(1 - 1.5$ eV) while it is at about $(6.5 - 6.8$ eV) for $(Bi_{0.21}Sb_{0.79})_2Te_3$ TI sample in fig. 4.15. Moreover, and because of the narrow energy range of Yin et. al. data which is up to 5 eV, the high energy plasmon did not appear.

A comparison between the experimental real and imaginary parts of the dielectric function and the theoretical study by Dr. Nechaev from Donostia International Physics Center in San Sebastán. Dr. Nechaev et al. study the electronic structure and the plasmonic excitations in the topological insulator [56–58] by using density functional theory (DFT) based on the GW approximation [110] (see section 3.5). Calculations were carried out within the all-electron full-potential linearized augmented-plane-wave (FLAPW) formalism [152] as implemented in the DFT code FLEUR and the GW code SPEX [153]. The calculations of Dr. Nechaev based on

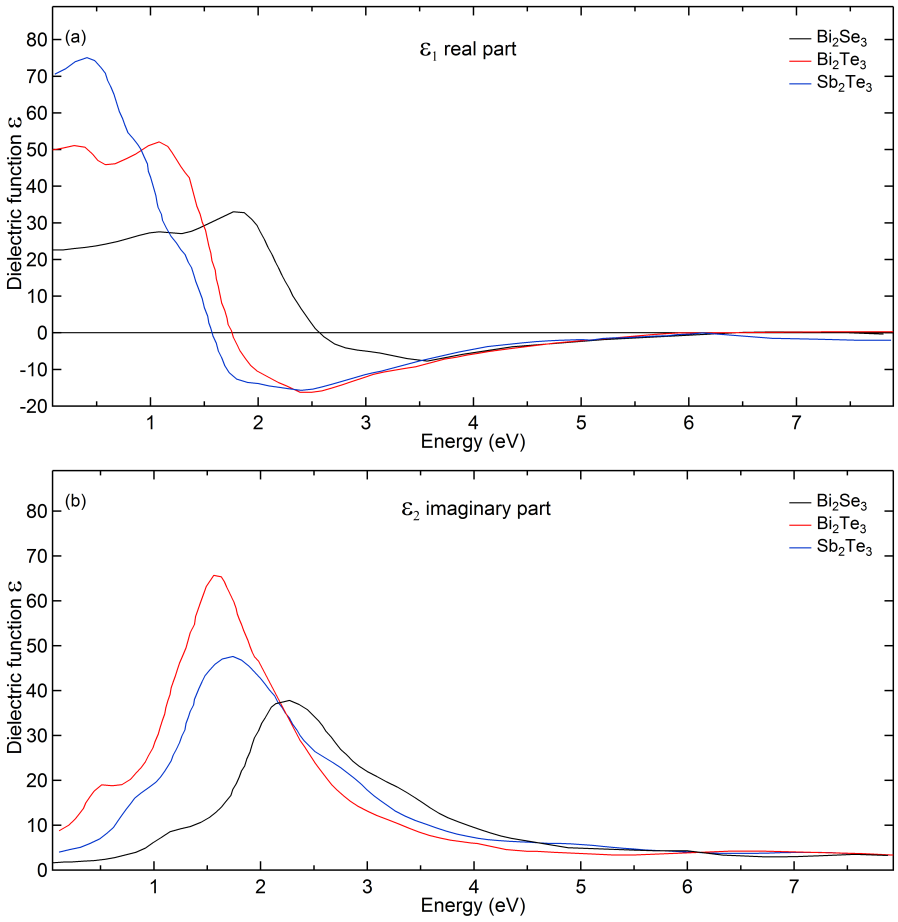

Figure 4.16: The theoretical dielectric function, (a) real and (b) imaginary parts for Bi_2Se_3, Sb_2Te_3 and Bi_2Te_3 calculated by Yin et. al. through DFT with local density approximation and optical Quantum ESPRESSO code [59].

the assumption of three oscillators (5.9, 11.6 and 16.5 eV)[58]. Figure 4.17 and 4.18 represent the comparison between the experimental real and imaginary parts of the dielectric function for the topological insulator thin film $(Bi_{0.21}Sb_{0.79})_2Te_3$ and the theoretical real and imaginary parts of the dielectric function of the topological insulator calculated by Dr. Nechaev [58]. All the features like the low and the high bulk plasmons the peak which appear between the 8 to 12 eV which are appears in the experimental real and imaginary parts of the dielectric function are compatible to that of the theoretical dielectric function [58].

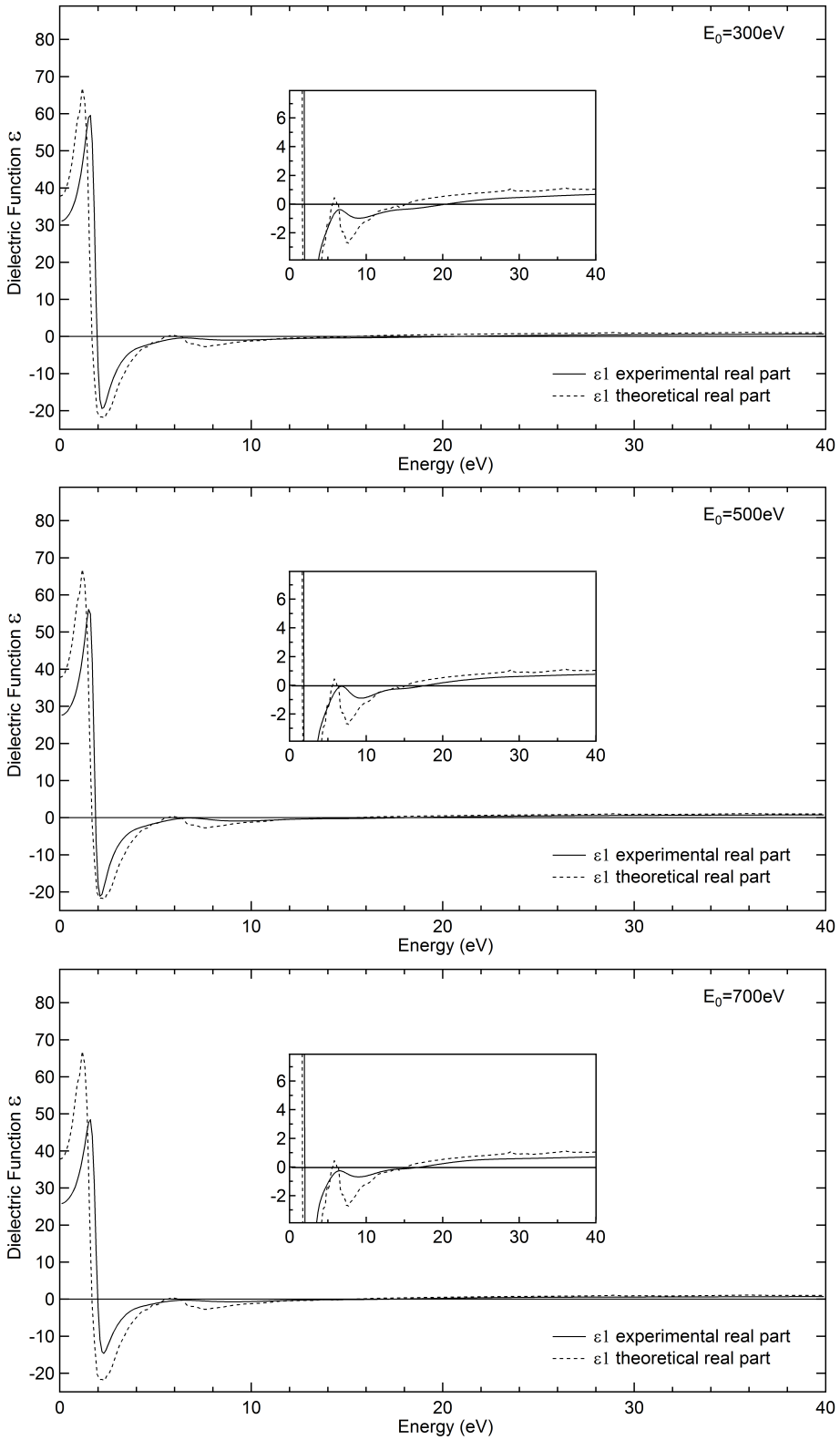

Figure 4.17: The experimental real part ε_1 of dielectric function of a topological insulator thin film at $E_0 = 300, 500$ and 700 eV primary electron energies compared to the theoretical real of the dielectric function calculated by Nechaev et al. [58].

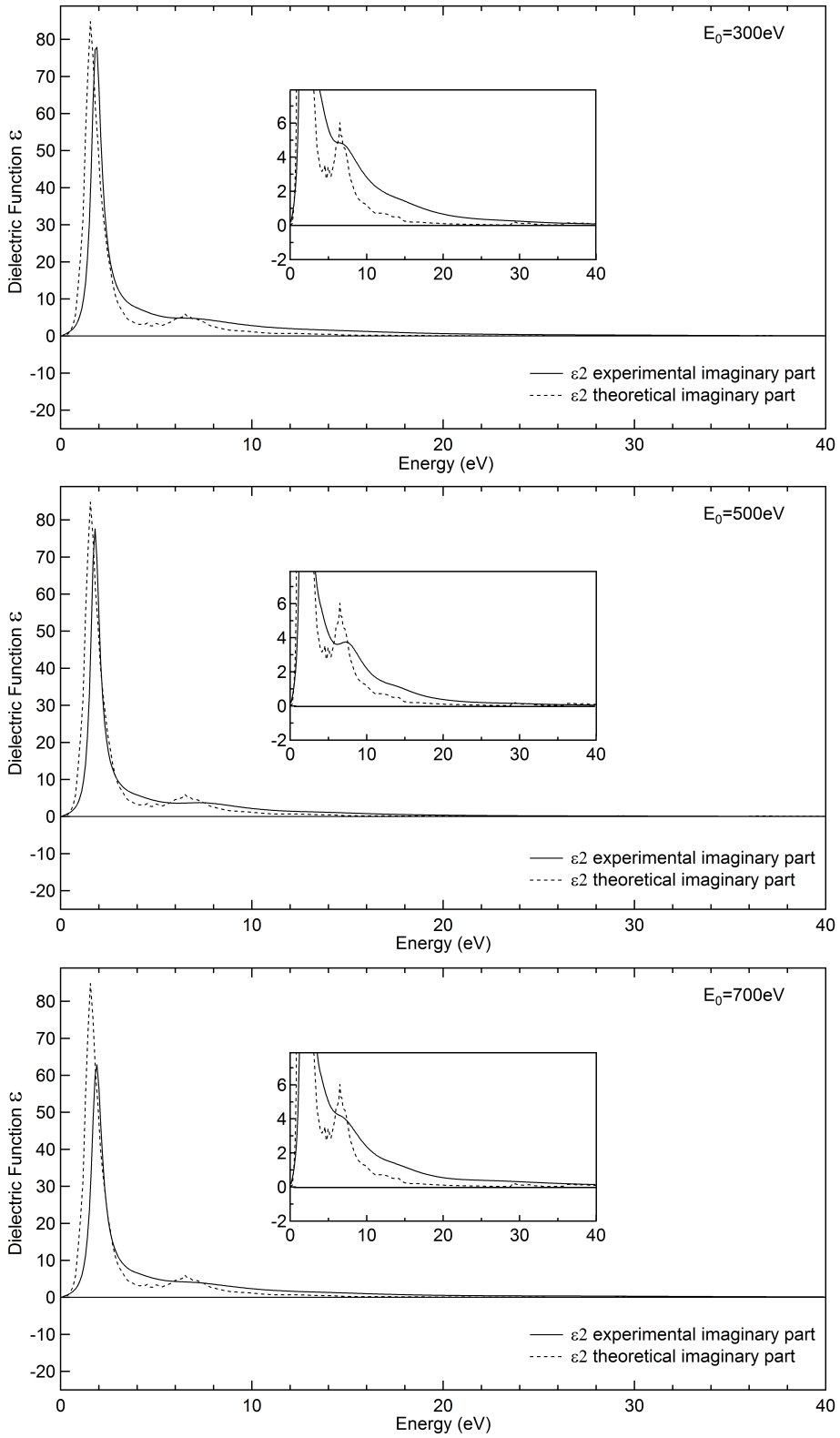

Figure 4.18: The experimental imaginary part ε_2 of dielectric function of a topological insulator thin film at $E_0 = 300$, 500 and 700 eV primary electron energies compared to the theoretical imaginary parts of the dielectric function calculated by Nechaev et al. [58].

4.3.3 Optical constants

Figure 4.19 demonstrate the refraction index n, the extinction coefficient κ, and the absorption coefficient α, were determined from the dielectric function for the topological insulator $(Bi_{0.21}Sb_{0.79})_2(Te)_3$ at primary energy of about 300 eV. The refraction index n shows a similar shape for all the samples. So it is obvious that in resonance the loss is high which is at about $2eV$ and the refraction index n, at a higher energies, approximately above $10eV$ the n is almost constant. The bow at 6 eV may related to the first oscillator which is usually lies on the excitation energy between $5.1 \sim 6.3$ eV. Return back to fig. 2.5 b which represent the refractive index n of the Bi_2Te_3 measured by Greenaway et. al. [45], it is clear that experimental behavior of n is so comparable to that plotted in the (top panel) in fig. 4.19.

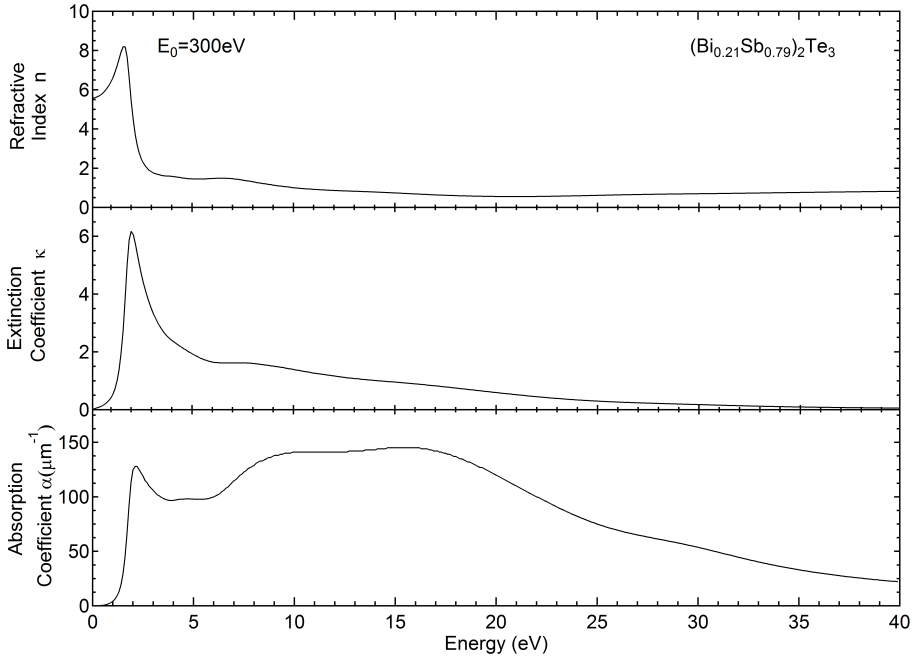

Figure 4.19: Optical parameters: Absorption A, extinction coefficients κ and refractive index n of a topological insulator $(Bi_{0.21}Sb_{0.79})_2Te_3$ thin film, extracted from REELS for primary energy E_0 = 300 eV.

The extinction coefficient κ spectrum for the topological insulator thin film sample $(Bi_{0.21}Sb_{0.79})_2(Te)_3$ (medal panel) in fig. 4.19 shows a maximum at 2 eV which is right at the resonance and decreases for higher energies, till its reaches the zero at 40 eV which represent the plasma frequency, further feature appears at 8 eV maybe due to the decapping heat process which can lead to an increase of the grain size [154, 155] which might explain the higher extinction coefficient in this region. The optically determined κ of this topological insulator deviates for binding

energy >8 eV compered to REELS pattern of REELS 4.12. The presence of the selenium as different composition on the surface [46], That sustains the XPS results of the selenium fig. 4.1. Moreover, there is a nice comparable between the experimental extinction coefficient κ for the $(Bi_{0.21}Sb_{0.79})_2(Te)_3$ topological insulator and the κ behavior of Bi_2Te_3 observed in the literature [45].

The (bottom panel) in 4.19 shows the absorption coefficient α of the topological insulator $(Bi_{0.21}Sb_{0.79})_2(Te)_3$, three different features can be observed, the first one appears in the binding energy <5 eV and the second broad peak exist in the binding energy interval between $7-20$ eV, it contain two bows at 9 and 17.5 eV. Another light trend appears at 29 eV binding energy, the second and the third peaks were explained in terms of the extinction coefficient κ or in another word due to the bulk contribution [58]. Also from figure 4.19 it is clear that the resonance is near by 2 eV, below this energy the material are transmissive. While on resonance the material properties become very extreme, for that the refraction index n, the extinction coefficient κ and the absorption coefficient α goes way up and the material become very absorbing on resonance [156]. Above this region the material become reflective in the binding energy range between $7-20$ eV, at the end of this region the high-energy plasmon lay, which represent the switch between the reflective region and the second transmissive region which is at binding energy >20 eV. While the low-energy plasmon located at the beginning of reflective interval, which is in a good agreement with the theoretical study [58]. For most of the samples the variation of the refraction index n and extinction coefficient κ in fig. 4.19 shows a comparable behavior to that in fig. 2.5 (b) observed by Greenaway et. al. for Bi_2Te_3. There are two features can be seen at 2 and 7 eV for extinction coefficient κ in the topological insulator $(Bi_{0.21}Sb_{0.79})_2(Te)_3$, which are the same for Bi_2Te_3 observed in ref. [45].

4.3.4 Systematic information about REELS measurements

Systematic REELS measurements have been done for samples with different magnetic concentrations (0% to 4% V), grown on different types of substrates (Si or InP), as well as for freshly decapped and aged (up to 24 hours) samples. Figure 4.20 shows the loss functions λK(E) extracted from REELS data for the $(Bi_{0.21}Sb_{0.79})_2Te_3$, $V_{0.1}(Bi_{0.21}Sb_{0.79})_{1.9}Te_3$ and $V_{0.2}(Bi_{0.21}Sb_{0.79})_{1.8}Te_3$ topological insulators, at primary electron energies of 300, 500 and 700 eV. It is obvious that the presence of the magnetic dopants in the sample do not affect the behavior of the loss function qualitatively. In principle, the existence of magnetic particles in the system could give rise to a magneto-optical response and, consequently, the optical constants. But the dilute character of the magnetic doping in the TI thin films do not strongly influence the host electronic properties. Thus, the nature of the plasmon excitations observed

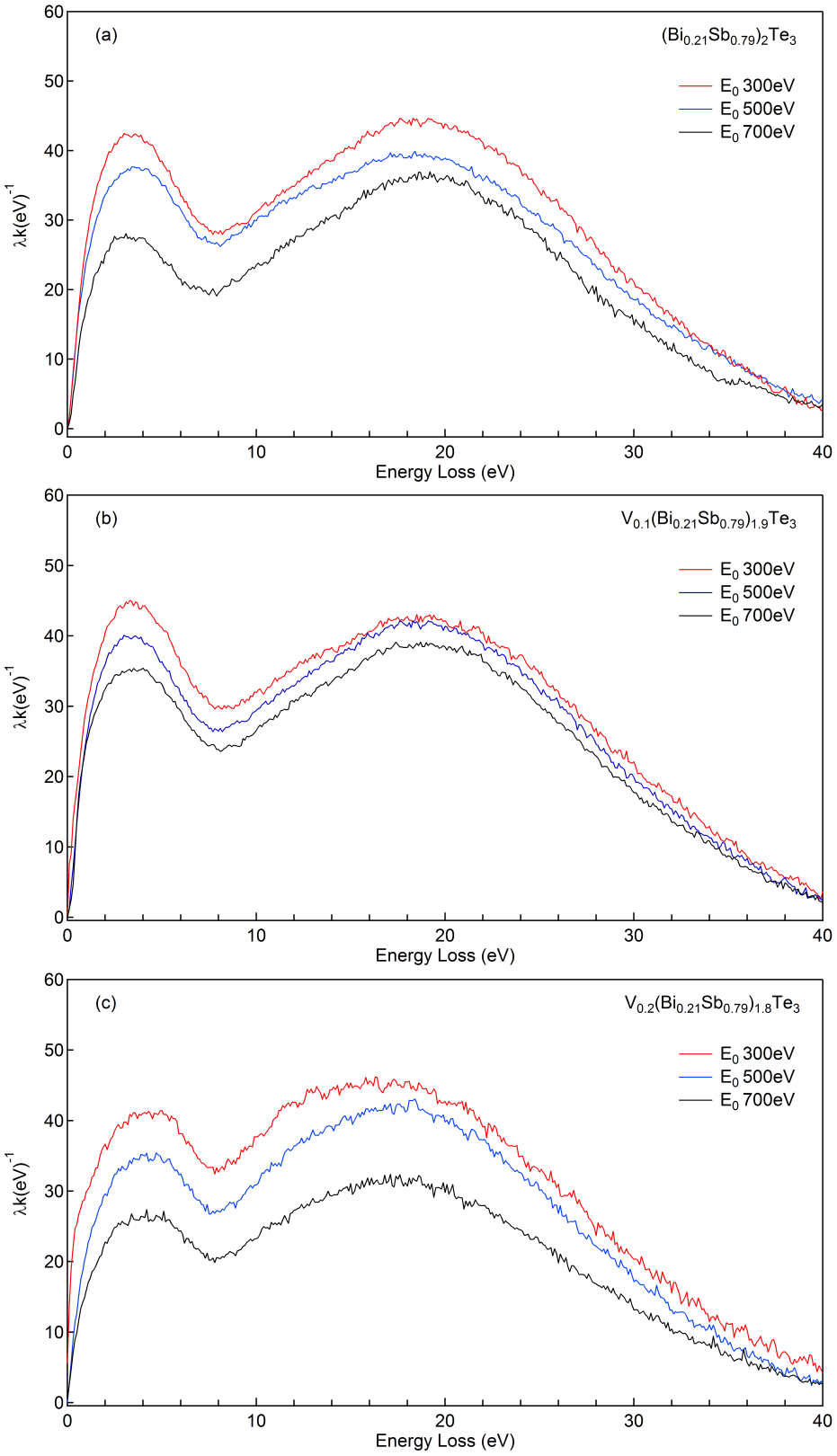

Figure 4.20: Loss function λK(E) from $(Bi_{0.21}Sb_{0.79})_2Te_3$ TI films doped with vanadium at (a) 0 at.% , (b) 2 at.% and (c) 4 at.%), at E_0 of 300 eV (red curve), 500 eV (blue curve) and 700 eV (black curve).

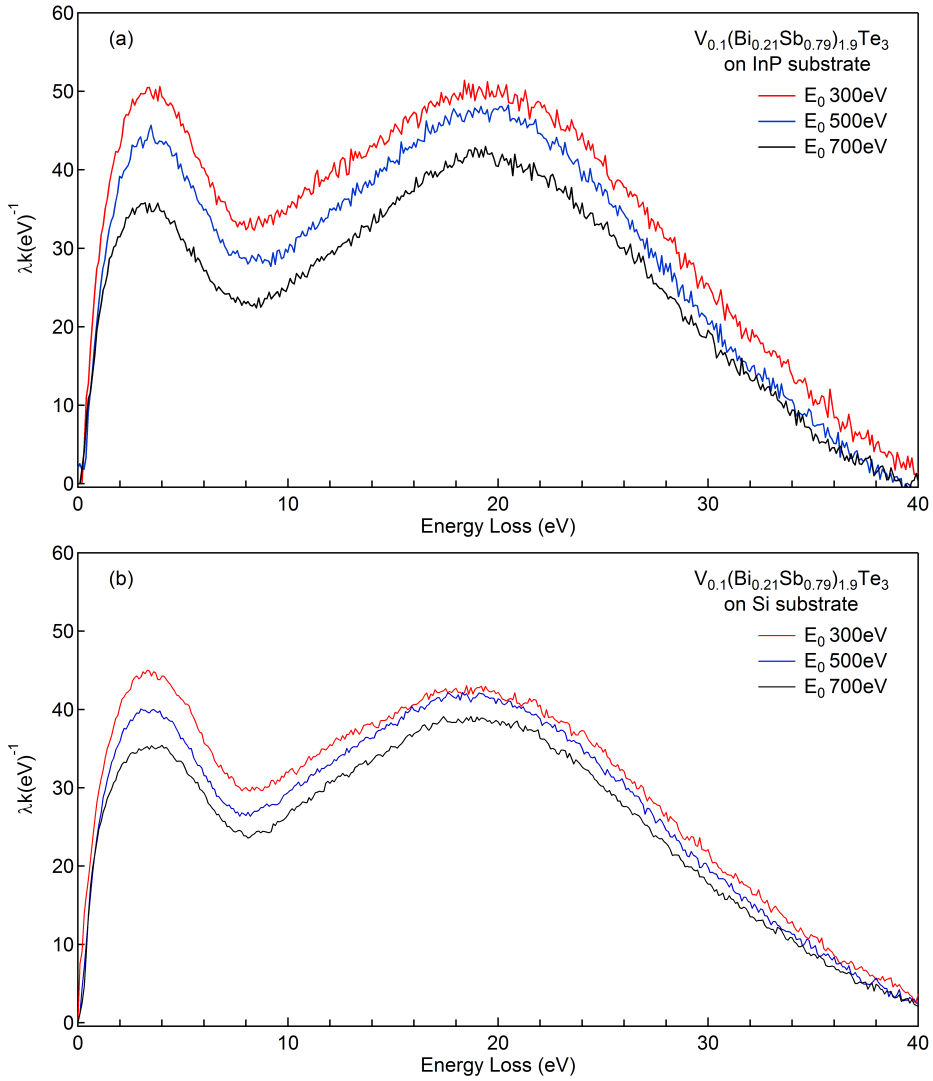

Figure 4.21: Loss function λK(E) from $V_{0.1}(Bi_{0.21}Sb_{0.79})_{1.9}Te_3$ TI films grown on (a) InP and (b) Si substrates, at primary electron energies of 300 eV (red curve), 500 eV (blue curve) and 700 eV (black curve).

here stem mostly from the topological insulator electronic structure.Another systematic observation has been performed on topological insulator thin films grown on two types of substrates. Figure 4.21 shows the loss functions λK(E) extracted from REELS data from $V_{0.1}(Bi_{0.21}Sb_{0.79})_{1.9}Te_3$ grown on (a) InP(111)and (b) Si(111), at primary electron energies of 300, 500 and 700 eV. They show no evidence of changes on the the loss function λK(E) lineshapes in dependence of the substrate. The typical film thicknesses are about 10 nm, which is much larger than the IMFP. REELS is a surface sensitive probing technique, so the incident electrons interact with the topmost layers and are reflected from the sample before reaching the underlying

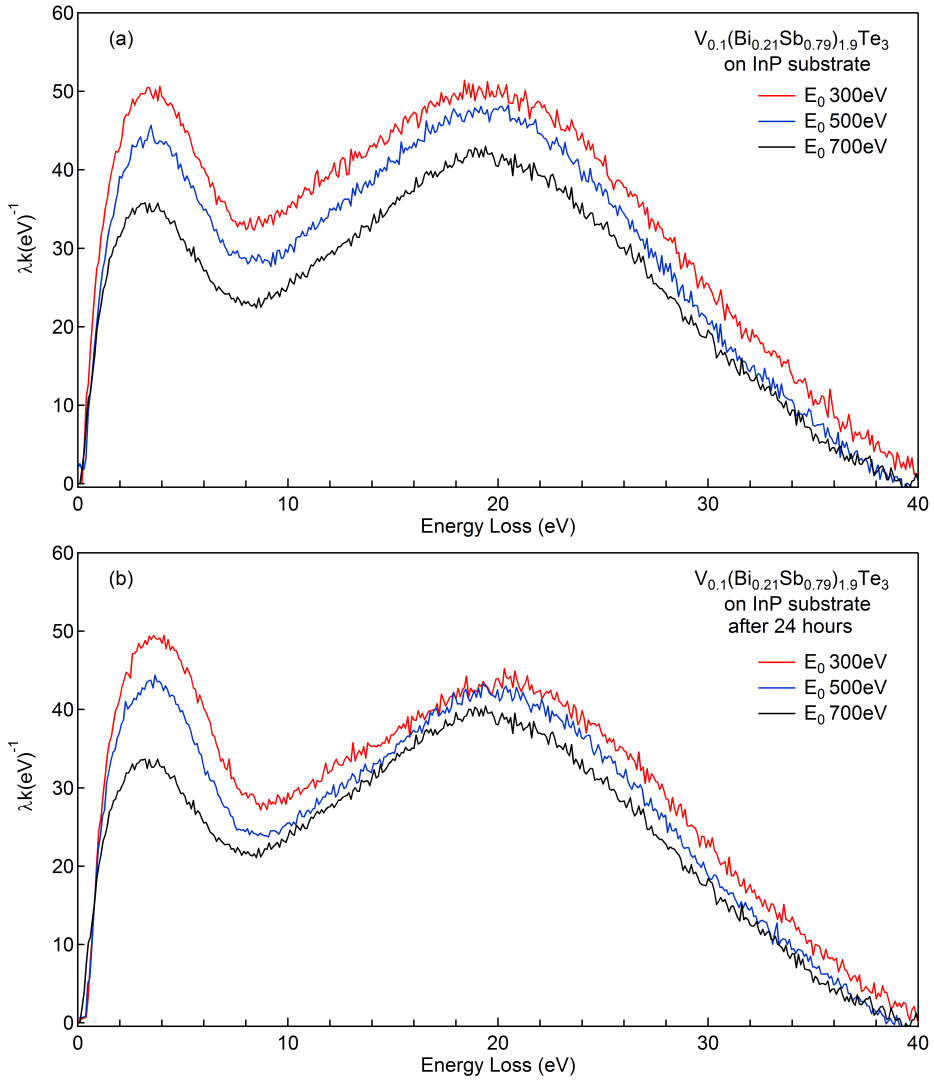

Figure 4.22: Loss function λK(E) for $V_{0.1}(Bi_{0.21}Sb_{0.79})_{1.9}Te_3$ TI films grown on an InP substrate measured at a (a) freshly decapped sample and (b) after 24 hours under vacuum, at primary electron energies of 300 eV (red curve), 500 eV (blue curve) and 700 eV (black curve).

substrate.

Furthermore, the aging-dependent measurements were performed to investigate the effect of the surface contamination by the background environment on the optical properties of the TI thin film. Figure 4.22 shows the loss functions λK(E) extracted from REELS data from $V_{0.1}(Bi_{0.21}Sb_{0.79})_{1.9}Te_3$ grown on InP(111) (a) right after decapping and (b) 24 hours after decapping , at primary electron energies of 300, 500 and 700 eV. It illustrates that even after one day under the UHV atmosphere no qualitative change occurs in the loss function. This leads the observer to believe that the optical properties remain stable up to one day under vacuum.

Finally, REELS experiments were performed at surfaces in which the decapping process did not satisfactorily succeed. These samples did not show any clear electron emission signal, which made the REELS measurements impossible. These samples were subsequently investigated by *ex situ* atomic force microscopy (AFM), showing a very rough surface. This may have lead to strong variations of the work-function of the surface, yielding an incoherent electron scattering.

In summary, the systematic observations in this dissertation shows that the effect of the concentration of the magnetic dopants (in the dilute range studied here), the type of substrate or aging do not strongly affect the surface optical properties. However, the surface quality, *i.e.* a successful decapping process, is very important for successful REELS experiments and, therefore, for determining the high energy optical properties.

CHAPTER 5

CONCLUDING DISCUSSION AND OUTLOOK

In this work I presented a consistent method for determining the electronic response to high-energy optical excitations and the optical constants of nanostructured materials. Here I demonstrated the validity of this method for the magnetically doped topological insulator films of $(V,Cr)_y(Bi_xSb_{1-x})_{2-y}Te_3$. The electron energy loss spectra were obtained from EELS experiments for primary energies between 100 and 1000 eV and were subsequently analyzed based on the Drude-Lorentz model of plasmonic excitations. The obtained electron energy loss function (ELF) was used to simulate the background of soft x-ray photoemission spectra of Te3d, Sb3d, Bi4f and Se3d core-levels, fitting the XPS data very well. In addition, by means of the Kramers-Kronig transformations I obtained the frequency-dependent dielectric function and calculated the main optical properties of magnetically doped $(Bi,Sb)_2Te_3$ for the first time. Due to the lack of optical characterization data on $(Bi,Sb)_2Te_3$ in the literature, the obtained real and imaginary parts of the dielectric function of these materials were compared with available optical data for intrinsic Sb_2Te_3, showing a reasonable agreement. In particular, the characteristic of the low-energy plasmon modes could identify.

Three oscillators were suggested to describe the dielectric function:

- First oscillator, with excitation energy $\hbar\omega_i$ $5.1 \sim 6.3$ eV, oscillator strength A_i $1.4 \sim 5.2\text{eV}^2$, and the damping coefficient $\hbar\beta_i$ range $2.7 \sim 6.5$ eV, whereas the area $1.5 \sim 30$.
- Second oscillator, with excitation energy $\hbar\omega_i$ $12.5 \sim 16.9$ eV, oscillator strength A_i $7 \sim 7.8\,\text{eV}^2$, and the damping coefficient $\hbar\beta_i$ range $8 \sim 13$ eV, whereas the area $56 \sim 102$.

- Third oscillator, with excitation energy $\hbar\omega_i$ $19 \sim 24.5\,\text{eV}$, oscillator strength A_i $324 \sim 455\,\text{eV}^2$, and the damping coefficient $\hbar\beta_i$ range $10 \sim 12\,\text{eV}$, whereas the area $3890 \sim 5469$.

and for all the oscillators the dispersion $\alpha_i = 1$. The bulk electron loss function (ELF) and the surface bulk electron loss function (SELF) calculated, shows the maximum at 22.5 eV for the ELF, while the SELF at 6 eV while the plasmons located at 11.8 and 17 eV are associated to the bulk and surface plasmon.

The other optical properties like the refraction index n, the extinction coefficient κ and absorption coefficient α were determined over a large energy range, and all the features which appears in these patterns were discussed extensively in chapter four.

Concerning the experimental real and imaginary parts of the dielectric function, the results shows two features: a low-energy peak at 6 eV and a split high-energy peak located at 24 eV, the two features associated to the low- and high-energy plasmon. These results shows a good agreement with the theoretical results of Dr. Nechaev from Donostia International Physics Center in San Sebastán-Spain. The theoretical study based on the density functional theory (DFT) with the use of the GW approximation. Interestingly, Dr. Nechaev based his theoretical calculations on the assumption of three oscillators 5.9, 11.6 and 16.5 eV, which is sufficiently comparable to the experimental results of this thesis.

Further more, the real and imaginary parts of the dielectric function calculated experimentally, shows also a good convergence with the theoretical calculations based on the $WIEN2k$ code with the generalized gradient approximation (GGA). This study is not published yet by Dr. Sudhir Kumar from the Institute of Eng. & Technology-M.J.P. Rohilkhand University-India.

The method described here is a general one and can be applied to other complex nanomaterials. It can further profit from the combination with electronic band structure *ab initio* calculations, since the theoretical simulation of the optical properties requires parameters that can be obtained from the band structure, such as shape and size of the bandgap and gap continuity function.

Topological insulators exhibit high potential for applicability in optoelectronic devices. In combination with the spin-dependent transport properties of these nanomaterials, one may take advantage of new degrees of freedom for the manipulation of information in such applications, as foreseen by the field of spintronics. Therefore the detailed knowledge of their electronic and optical properties is of utmost importance for the development of these novel applications.

Finally, I hope to have contributed to motivating the development of theoretical as well as experimental studies of the optical properties of magnetically doped topological insulators in the near future.

BIBLIOGRAPHY

[1] Calligraphy. *The english translation: In the name of God, the Most Gracious, the Most Merciful.* arabic hand writing art.

[2] C. L. Kane and E. J. Mele. "Quantum Spin Hall Effect in Graphene". *Physical Review Letters* **95** (2005), pp. 226801–1–226801–4.

[3] J. E. Moore. "Topological Insulators The next generation". *Nature Physics* **5** (2009), pp. 378–380.

[4] L. Fu, C. L. Kane, and E. J. Mele. "Topological Insulators in Three Dimensions". *Physical Review Letters* **98** (2007), pp. 106803–1–106803–4.

[5] S. Murakami. "Phase transition between the quantum spin Hall and insulator phases in 3D: emergence of a Topological gapless phase". *New Journal of Physics* **9** (2007), pp. 356–1–356–15.

[6] L. Fu and C. L. Kane. "Topological Insulators with inversion symmetry". *Physical Review B* **76** (2007), pp. 045302–1–045302–17.

[7] D. Hsieh, D. Qian, L. Wray, Y. Xia, Y. S. Hor, R. J. Cava, and M. Z. Hasan. "A Topological Dirac Insulator in a quantum spin Hall phase". *Nature* **452** (2008), pp. 970–974.

[8] M. König, S. Wiedmann, C. Brüne, A. Roth, H. Buhmann, M. Laurens, X. L. Qi, and S. Zhang. "Quantum Spin Hall Insulator State in HgTe Quantum Wells" (2007), pp. 766–770.

[9] D. Hsieh, Y. Xia, L. Wray, D. Qian, A. Pal, J. H. Dil, J. Osterwalder, F. Meier, G. Bihlmayer, C. L. Kane, Y. S. Hor, R. J. Cava, and M. Z. Hasan. "Observation of Unconventional Quantum Spin Textures in Topological Insulators". *Science* **323** (2009), pp. 915–919.

[10] Y. Xia, D. Qian, D. Hsieh, L. Wray, A. Pal, H. Lin, A. Bansil, D. Grauer, Y. S. Hor, R. J. Cava, and M. Z. Hasan. "Observation of a large-gap Topological-

Insulator class with a single Dirac cone on the surface". *Nature Physics* **5** (2009), pp. 398–402.

[11] M. Z. Hasan and C. L. Kane. "Colloquium : Topological insulators". *Reviews of Modern Physics* **82** (2010), pp. 3045–3067.

[12] R. Yu, H.-J. Zhang, and W. Zhang. "Quantized Anomalous Hall Effect in Magnetic Topological Insulators". *Science* **329** (2010), pp. 59–61.

[13] Y. Jiang, C. Song, Z. Li, M. Chen, R. L. Greene, K. He, L. Wang, X. Chen, X. Ma, and Q.-K. Xue. "Mass acquisition of Dirac fermions in magnetically doped Topological Insulator Sb_2Te_3 films". *Physical Review B* **92** (2015), pp. 195418–1–195418–9.

[14] Z. Qiao, W. Ren, H. Chen, L. Bellaiche, Z. Zhang, A. H. MacDonald, and Q. Niu. "Quantum anomalous Hall effect in graphene proximity coupled to an antiferromagnetic insulator". *Physical review letters* **112** (2014), pp. 116404–1–116404–5.

[15] H. Weng, R. Yu, X. Hu, X. Dai, and Z. Fang. "Quantum anomalous Hall effect and related Topological electronic states". *Advances in Physics* **64** (2015), pp. 227–282.

[16] X.-L. Qi and S.-C. Zhang. "Topological Insulators and Superconductors". *Reviews of Modern Physics* **83** (2011), pp. 1057–1110.

[17] L. A. Wray, S.-Y. Xu, Y. Xia, D. Hsieh, A. V. Fedorov, Y. S. Hor, R. J. Cava, A. Bansil, H. Lin, and M. Z. Hasan. "A topological insulator surface under strong Coulomb, magnetic and disorder perturbations". *Nature Physics* **7** (2011), pp. 32–37.

[18] C.-Z. Chang, J. Zang, F. Xiao, J. Shen, Z. Zhang, M. Guo, K. Li, Y. Ou, P. Wei, L.-L. Wang, Z.-Q. Ji, Y. Feng, S.-H. Ji, X. Chen, J.-F. Jia, X. Dai, Z. Fang, S.-C. Zhang, K. He, Y. Wang, L. Lu, X.-C. Ma, and Q.-K. Xue. "Experimental Observation of the Quantum Anomalous Hall Effect in a Magnetic Topological Insulator". *Science* **340** (2013), pp. 167–170.

[19] C.-Z. Chang, W. Zhao, D. Y. Kim, H. Zhang, B. A. Assaf, D. Heiman, S.-C. Zhang, C. Liu, M. H. W. Chan, and J. S. Moodera. "High-precision realization of robust quantum anomalous Hall state in a hard ferromagnetic Topological Insulator". *Nature Materials* **14** (2015), pp. 473–477.

[20] S. Grauer, S. Schreyeck, M. Winnerlein, K. Brunner, C. Gould, and L. W. Molenkamp. "Coincidence of superparamagnetism and perfect quantization in the quantum anomalous Hall state". *Physical Review B* **92** (2015), pp. 201304–1–201304–5.

[21] X.-L. Qi, Y.-S. Wu, and S.-C. Zhang. "Topological quantization of the spin Hall effect in Two-Dimensional paramagnetic semiconductors". *Physical Review B* **74** (2006), pp. 085308–1–085308–7.

[22] K. v Klitzing, G. Dorda, and M. Pepper. "New method for high-accuracy determination of the fine-structure constant based on quantized Hall resistance". *Physical Review Letters* **45** (1980), pp. 494–497.

[23] L. He, X. Kou, and K. L. Wang. "Review of 3D Topological Insulator thin-film growth by molecular beam epitaxy and potential applications". *physica status solidi (RRL) - Rapid Research Letters* **7** (2013), pp. 50–63.

[24] M. Eschbach, E. Młyńczak, J. Kellner, J. Kampmeier, M. Lanius, E. Neumann, C. Weyrich, M. Gehlmann, P. Gospodarič, S. Döring, G. Mussler, N. Demarina, M. Luysberg, G. Bihlmayer, T. Schäpers, L. Plucinski, S. Blügel, M. Morgenstern, C. M. Schneider, and D. Grützmacher. "Realization of a vertical Topological p-n junction in epitaxial Sb_2Te_3/Bi_2Te_3 heterostructures". *Nature Communications* **6** (2015), pp. 8816–1–8816–7.

[25] C.-Z. Chang, J. Zhang, M. Liu, Z. Zhang, X. Feng, K. Li, L.-L. Wang, X. Chen, X. Dai, Z. Fang, X.-L. Qi, S.-C. Zhang, Y. Wang, K. He, X.-C. Ma, and Q.-K. Xue. "Thin Films of Magnetically Doped Topological Insulator with Carrier-Independent Long-Range Ferromagnetic Order". *Advanced Materials* **25** (2013), pp. 1065–1070.

[26] K. Schubert, K. Anderko, M. Kluge, H. Beeskow, M. Ilschner, E. Dörre, and P. Esslinger. "Strukturuntersuchung der Legierungsphasen Cu_2Te, CuTe, Cu_3Sb, InTe, Bi_2Se_3, Pd_5Sb_3 und Pd_5Bi_3". **40** (1953), pp. 269 –269.

[27] J. R. Wiese and L Muldawer. "Lattice constants of Bi_2Te_3-Bi_2Se_3 solid solution alloys". *Pergamon Press* **15** (1960), p. 13.

[28] H. Zhang, C.-X. Liu, X.-L. Qi, X. Dai, Z. Fang, and S.-C. Zhang. "Topological insulators in Bi_2Se_3, Bi_2Te_3 and Sb_2Te_3 with a single Dirac cone on the surface". *Nature Physics* **5** (2009), pp. 438–442.

[29] Y. L. Chen, J. G. Analytis, J.-H. Chu, Z. K. Liu, S.-K. Mo, X. L. Qi, H. J. Zhang, D. H. Lu, X. Dai, Z. Fang, S. C. Zhang, I. R. Fisher, Z. Hussain, and Z.-X. Shen. "Experimental Realization of a Three-Dimensional Topological Insulator, Bi_2Te_3". *Science* **325** (2009), pp. 178–181.

[30] D. Teweldebrhan, V. Goyal, and A. A. Balandin. "Exfoliation and Characterization of Bismuth Telluride Atomic Quintuples and Quasi-Two-Dimensional Crystals". *Nano Letters* **10** (2010), pp. 1209–1218.

[31] D. Kong, J. C. Randel, H. Peng, J. J. Cha, S. Meister, K. Lai, Y. Chen, Z.-X. Shen, H. C. Manoharan, and Y. Cui. "Topological Insulator Nanowires and Nanoribbons". *Nano Letters* **10** (2010), pp. 329–333.

[32] D. Kong, W. Dang, J. J. Cha, H. Li, S. Meister, H. Peng, Z. Liu, and Y. Cui. "Few-Layer Nanoplates of Bi_2Se_3 and Bi_2Te_3 with Highly Tunable Chemical Potential". *Nano Letters* **10** (2010), pp. 2245–2250.

[33] M. Winnerlein, S. Schreyeck, S. Grauer, S. Rosenberger, K. M. Fijalkowski, C. Gould, K. Brunner, and L. W. Molenkamp. "Epitaxy and structural properties of $(V,Bi,Sb)_2Te_3$ layers exhibiting the quantum anomalous Hall effect". *Physical Review Materials* **1** (2017), pp. 011201–1–011201–5.

[34] M. König, H. Buhmann, L. W. Molenkamp, T. L. Hughes, C.-X. Liu, X. L. Qi, and S.-C. Zhang. "The Quantum Spin Hall Effect: Theory and Experiment". *J. Phys. Soc. Jpn.* **77** (2008), p. 031007.

[35] S. V. Eremeev, G. Landolt, T. V. Menshchikova, B. Slomski, Y. M. Koroteev, Z. S. Aliev, M. B. Babanly, J. Henk, A. Ernst, L. Patthey, A. Eich, A. A. Khajetoorians, J. Hagemeister, O. Pietzsch, J. Wiebe, R. Wiesendanger, P. M. Echenique, S. S. Tsirkin, I. R. Amiraslanov, J. H. Dil, and E. V. Chulkov. "Atom-specific spin mapping and buried topological states in a homologous series of topological insulators". *Nature Communications* **3** (2012), pp. 635–1–635–7.

[36] P. Roushan, J. Seo, C. V. Parker, Y. S. Hor, D. Hsieh, D. Qian, A. Richardella, M. Z. Hasan, R. J. Cava, and A. Yazdani. "Topological surface states protected from backscattering by chiral spin texture". *Nature* **460** (2009), pp. 1106–1109.

[37] Z. Alpichshev, J. G. Analytis, J.-H. Chu, I. R. Fisher, Y. L. Chen, Z. X. Shen, A. Fang, and A. Kapitulnik. "STM Imaging of Electronic Waves on the Surface of Bi_2Te_3 : Topologically Protected Surface States and Hexagonal Warping Effects". *Physical Review Letters* **104** (2010), pp. 016401–1–016401–4.

[38] J. Hillier and R. F. Baker. "Microanalysis by Means of Electrons". *Journal of Applied Physics* **15** (1944), pp. 663–675.

[39] H. Watanabe. "Experimental Evidence for the Collective Nature of the Characteristic Energy Loss of Electrons in (Solids-Studies) on the Dispersion Relation of Plasma Frequency". *Journal of the Physical Society of Japan* (1956), pp. 112–119.

[40] S. Tougaard. "Surface nanostructure determination by X-ray photoemission spectroscopy peak shape analysis". *Journal of Vacuum Science & Technology A: Vacuum, Surfaces, and Films* **14** (1996), pp. 1415–1423.

[41] M. P. Seah, I. S. Gilmore, and S. J. Spencer. "Background subtraction: II. General behaviour of REELS and the Tougaard universal cross section in the removal of backgrounds in AES and XPS". *Surface science* **461** (2000), pp. 1–15.

[42] E. E. Krasovskii, V. M. Silkin, V. U. Nazarov, P. M. Echenique, and E. V. Chulkov. "Dielectric screening and band-structure effects in low-energy photoemission". *Physical Review B* **82** (2010), pp. 125102–1–125102–5.

[43] Y. Cao, J. A. Waugh, X.-W. Zhang, J.-W. Luo, Q. Wang, T. J. Reber, S. K. Mo, Z. Xu, A. Yang, J. Schneeloch, G. D. Gu, M. Brahlek, N. Bansal, S. Oh, A. Zunger, and D. S. Dessau. "Mapping the orbital wavefunction of the surface states in three-dimensional topological insulators". *Nature Physics* **9** (2013), pp. 499–504.

[44] Z.-H. Zhu, C. Veenstra, S. Zhdanovich, M. Schneider, T. Okuda, K. Miyamoto, S.-Y. Zhu, H. Namatame, M. Taniguchi, M. Haverkort, I. Elfimov, and A. Damascelli. "Photoelectron Spin-Polarization Control in the Topological Insulator Bi_2Se_3". *Physical Review Letters* **112** (2014), pp. 076802–1–076802–5.

[45] D. L. Greenaway and G. Harbeke. "Band structure of Bismuth Telluride, Bismuth Selenide and their respective alloys". *Journal of Physics and Chemistry of Solids* **26** (1965), pp. 1585–1604.

[46] V. V. Sobolev, S. D. Shutov, Y. V. Popov, and S. N. Shestatskii. "Reflectivity Spectra of the Rhombohedral Crystals Bi_2Te_3, Bi_2Se_3, and Sb_2Te_3 over the Range from 0.7 to 12.5 eV". *physica status solidi (b)* **30** (1968), pp. 349–355.

[47] V. Nascimento. "XPS and EELS study of the Bismuth Selenide". *Journal of Electron Spectroscopy and Related Phenomena* **104** (1999), pp. 99–107.

[48] S. C. Liou, M.-W. Chu, R. Sankar, F.-T. Huang, G. J. Shu, F. C. Chou, and C. H. Chen. "Plasmons dispersion and nonvertical interband transitions in single crystal Bi_2Se_3 investigated by electron energy-loss spectroscopy". *Physical Review B* **87** (2013), pp. 085126–1–085126–6.

[49] M. Zhao, M. Bosman, M. Danesh, M. Zeng, P. Song, Y. Darma, A. Rusydi, H. Lin, C.-W. Qiu, and K. P. Loh. "Visible Surface Plasmon Modes in Single Bi_2Te_3 Nanoplate". *Nano Letters* **15** (2015), pp. 8331–8335.

[50] A. A. Reijnders, Y. Tian, L. J. Sandilands, G. Pohl, I. D. Kivlichan, S. Y. F. Zhao, S. Jia, M. E. Charles, R. J. Cava, N. Alidoust, S. Xu, M. Neupane, M. Z. Hasan, X. Wang, S. W. Cheong, and K. S. Burch. "Optical evidence of surface state suppression in Bi-based topological insulators". *Physical Review B* **89** (2014).

[51] R. K. Gopal, D. K. Ambast, S. Singh, J. Sarkar, B. Pal, and C. Mitra. "Bulk saturable absorption in topological insulator thin films". *Journal of Applied Physics* **122** (2017), p. 035705.

[52] Y. R. Sapkota, A. Alkabsh, A. Walber, H. Samassekou, and D. Mazumdar. "Optical evidence for blue shift in topological insulator bismuth selenide in the few-layer limit". *Applied Physics Letters* **110** (2017), p. 181901.

[53] O. V. Yazyev, E. Kioupakis, J. E. Moore, and S. G. Louie. "Quasiparticle effects in the bulk and surface-state bands of Bi_2Se_3 and Bi_2Te_3 Topological Insulators". *Physical Review B* **85** (2012), pp. 161101–1–161101–4.

[54] I. Aguilera, C. Friedrich, and S. Blügel. "Spin-orbit coupling in quasiparticle studies of Topological Insulators". *Physical Review B* **88** (2013).

[55] I. Aguilera, C. Friedrich, G. Bihlmayer, and S. Blügel. "GW study of Topological Insulators Bi_2Se_3 , Bi_2Te_3, and Sb_2 Te_3: Beyond the perturbative one-shot approach". *Physical Review B* **88** (2013), pp. 045206–1–045206–7.

[56] I. A. Nechaev and E. V. Chulkov. "Quasiparticle band gap in the Topological Insulator Bi_2Te_2". *Physical Review B* **88** (2013), pp. 165135–1–165135–11.

[57] I. A. Nechaev, R. C. Hatch, M. Bianchi, D. Guan, C. Friedrich, I. Aguilera, J. L. Mi, B. B. Iversen, S. Blügel, P. Hofmann, and E. V. Chulkov. "Evidence for a direct band gap in the Topological Insulator Bi_2Se_3 from theory and experiment". *Physical Review B* **87** (2013), pp. 121111–1–121111–5.

[58] I. A. Nechaev, I. Aguilera, V. De Renzi, A. di Bona, A. Lodi Rizzini, A. M. Mio, G. Nicotra, A. Politano, S. Scalese, Z. S. Aliev, M. B. Babanly, C. Friedrich,

S. Blügel, and E. V. Chulkov. "Quasiparticle spectrum and plasmonic excitations in the Topological Insulator Sb_2Te_3". *Physical Review B* **91** (2015), pp. 245123–1–245123–8.

[59] J. Yin, H. N. Krishnamoorthy, G. Adamo, A. M. Dubrovkin, Y. Chong, N. I. Zheludev, and C. Soci. "Plasmonics of topological insulators at optical frequencies". *NPG Asia Materials* **9** (2017), e425.

[60] H. Hertz. "Ueber einen Einfluss des ultravioletten Lichtes auf die electrische Entladung". *Annalen der Physik,* (1887), pp. 983–1000.

[61] A. Einstein. "Über einen die Erzeugung und Verwandlung des Lichtes betreffenden heuristischen Gesichtspunkt". **322** (1905), pp. 132–148.

[62] A. Einstein. "Zur Theorie der Lichterzeugung und Lichtabsorption". **325** (1906), pp. 199–206.

[63] A. Einstein. "Quantum theory of radiation, Zur Quantentheorie der Strahlung". *Physikalische Gesellschaft Zürich* **16** (1916), pp. 47–62.

[64] K. Siegbahn. "Electron spectroscopy for atoms, molecules and condensed matter". *Nova Acta Regiae Societatis Scientiarum Upsaliensis* **Ser.IV** (1967), p20.

[65] S. Hüfner. *Photoelectron Spectroscopy*. 2nd Edition. 1995.

[66] S. Tanuma, C. J. Powell, and D. R. Penn. "Proposed formula for electron inelastic mean free paths based on calculations for 31 materials". *Surface Science* **192** (1987), pp. L849–L857.

[67] S. Tanuma, C. J. Powell, and D. R. Penn. "Calculations of electron inelastic mean free paths for 31 materials". *Surface and Interface Analysis* **11** (1988), pp. 577–589.

[68] S. Tanuma, C. J. Powell, and D. R. Penn. "Calculations of electorn inelastic mean free paths. II. Data for 27 elements over the 50–2000 eV range". *Surface and Interface Analysis* **17** (1991), pp. 911–926.

[69] S. Tanuma, C. J. Powell, and D. R. Penn. "Calculations of electron inelastic mean free paths. III. Data for 15 inorganic compounds over the 50–2000 eV range". *Surface and Interface analysis* **17** (1991), pp. 927–939.

[70] S. Tanuma, C. J. Powell, and D. R. Penn. "Calculations of electron inelastic mean free paths (IMFPs). IV. Evaluation of calculated IMFPs and of the

predictive IMFP formula TPP-2 for electron energies between 50 and 2000 eV". *Surface and interface analysis* **20** (1993), pp. 77–89.

[71] S. Tanuma, C. J. Powell, and D. R. Penn. "Calculations of electron inelastic mean free paths. V. Data for 14 organic compounds over the 50–2000 eV range". *Surface and interface analysis* **21** (1994), pp. 165–176.

[72] S. Tougaard. "QUASES-Tougaard Quantitative Analysis of Surfaces by Electron Spectroscopy". **Version 5.1** (2011).

[73] J. F. Watts and J. Wolstenholme. *An introduction to surface analysis by XPS and AES*. Chichester, West Sussex, England ; New York: J. Wiley, 2003.

[74] M. P. Seah and W. A. Dench. "Quantitative electron spectroscopy of surfaces: a standard data base for electron inelastic mean free paths in solids". *Surface and interface analysis* **1** (1979), pp. 2–11.

[75] R. F. Egerton. "Electron energy-loss spectroscopy in the TEM". *Reports on Progress in Physics* **72** (2009), pp. 016502–1–016502–25.

[76] D. Pines and D. Bohm. "A collective description of electron interactions: II. Collective vs individual particle aspects of the interactions". *Physical Review* **85** (1952), pp. 338–353.

[77] D. Bohm and D. Pines. "A collective description of electron interactions: III. Coulomb interactions in a degenerate electron gas". *Physical Review* **92** (1953), pp. 609–625.

[78] D. Pines. "A collective description of electron interactions: IV. Electron interaction in metals". *Physical Review* **92** (1953), pp. 626–636.

[79] J. C. Ingram, K. W. Nebesny, and J. E. Pemberton. "Optical constants of the noble metals determined by reflection electron energy loss spectroscopy". *Applied Surface Science* **44** (1990), pp. 293–300.

[80] P. Drude. "Zur Elektronentheorie der Metalle II. Teil, Galvanomagnetische und thermomagnetische Effecte". *Annalen der Physik* **308** (1900), pp. 369–402.

[81] P. Drude. "Zur Elektronentheorie der Metalle I." *Annalen der Physik* **306** (1900), pp. 566–613.

[82] N. W. Ashcroft and N. D. Mermin. *Solid State Physics*. College Edition. Harcourt college Publishers, 1976.

[83] N. Ashcroft, N. Mermin, and d. Wei. *Solid State Physics*. Revised Edition. Singapore: Cengage Learning Asia Pte Ltd, 2016.

[84] K. Kopitzki and P. Herzog. *Einführung in die Festkörperphysik*. 6th Edition. Germany: Teubner GmbH Wiesbaden, 2007.

[85] F. Yubero, J. M. Sanz, B. Ramskov, and S. Tougaard. "Model for quantitative analysis of reflection electron energy loss spectra: Angular dependence". *Physical Review B* **53** (1996), pp. 9719–9727.

[86] J. Thirlwell. "Characteristic energy losses of low-energy electrons reflected from aluminium and copper". *Journal of Physics C: Solid State Physics* **1** (1968), pp. 979–989.

[87] R. Brydson. *Electron Energy Loss Spectroscopy*. 1st Edition. Taylor & Francis, 2001.

[88] J. Thirlwell. "The characteristic energy losses of slow electrons reflected from aluminium, germanium, copper and gold". *Proceedings of the Physical Society* **91** (1967), pp. 552–564.

[89] F. Reinert. "Diplomarbeit, Elektronenspektroskopie an NiO und $Ni_{1-x}Li_xO$". PhD thesis. Universität des Saarlandes, Mathematisch Naturwissenschaftliche Fakultät, 1992.

[90] R. L. Kronig. "On the theory of dispersion of X-Rays". *J. Opt. Soc. Am.* **12** (1926), pp. 547–556.

[91] H. A. Kramers. "La diffusion de la lumiere par les atomes". *Atti Cong. Intern. Fisici* (1927), pp. 545–557.

[92] S. Tougaard and F. Yubero. "Manual QUEELS epsilion REELS". **Version 4.32** (2013).

[93] H. Kuzmany. *Solid-state spectroscopy: an introduction*. 2nd Edition. New York: Springer-Verlag Berlin Heidelberg, 2009.

[94] J. Geiger. *Elektronen und Festkrper*. 1st Edition. Springer Fachmedien Wiesbaden GmbH, Vieweg & Sohn GmbH, Braunschweig, 1968.

[95] J. Daniels and C. Festenberg. "Optical Constant of Solids By Electron Spectroscopy". *Springer Tracts in Modern Physics*. Vol. 54. Springer, 1970, pp. 77–135.

[96] F. Wooten. *Optical Properties Of Solids*. Academic Press, Inc (London), 1972.

[97] S. Tougaard. "universality classes of inelastic electron scattering cross sections". *Surface and Interface Analysis* **25** (1997), pp. 137–154.

[98] S. Tougaard. "Algorithm for analysis of low-energy-resolution REELS; determination of inelastic electron scattering cross sections and applications in quantitative XPS". *Surface science* **464** (2000), pp. 233–239.

[99] S. Tougaard and I. Chorkendorff. "Differential inelastic electron scattering cross sections from experimental reflection electron energy loss spectra: Application to background removal in electron spectroscopy". *The American Physical Society* **35** (1987), pp. 6570–6577.

[100] F. Yubero and S. Tougaard. "Model for quantitative analysis of reflection electron energy loss spectra". *Physical Review B* **46** (1992), pp. 2486–2497.

[101] R. H. Ritchie. "Plasma losses by fast electrons in thin films". *Physical Review* **106** (1957), pp. 874–881.

[102] D. Tahir, E. K. Lee, H. L. Kwon, S. Kun Oh, H. J. Kang, S. Heo, E. H. Lee, J. G. Chung, J. C. Lee, and S. Tougaard. "Electronic and optical properties of GIZO thin film grown on SiO_2/Si substrates". *Surface and Interface Analysis* **42** (2010), pp. 906–910.

[103] F. Yubero, S. Tougaard, E. Elizalde, and J. M. Sanz. "Dielectric loss function of Si and SiO_2 from quantitative analysis of REELS spectra". *Surface and interface analysis* **20** (1993), pp. 719–726.

[104] F. Yubero, D. Fujita, B. Ramskov, and S. Tougaard. "Experimental test of model for angular and energy dependence of reflection electron energy loss spectra". *Physical Review B* **53** (1996), pp. 9728–9732.

[105] S. Hajati, O. Romanyuk, J. Zemek, and S. Tougaard. "Validity of Yubero-Tougaard theory to quantitatively determine the dielectric properties of surface nanofilms". *Physical Review B* **77** (2008), pp. 155403–1–155403–11.

[106] S. Tougaard and J. Kraaer. "Inelastic electron scattering cross sections for Si, Cu, Ag, Au, Ti, Fe, and Pd". *Physical Review B* **43** (1991), pp. 1651–1661.

[107] E. Kioupakis, M. L. Tiago, and S. G. Louie. "Quasiparticle electronic structure of Bismuth Telluride in the GW approximation". *Physical Review B* **82** (2010).

[108] R. Sakuma, C. Friedrich, T. Miyake, S. Blügel, and F. Aryasetiawan. "GW calculations including spin-orbit coupling: Application to Hg chalcogenides". *Physical Review B* **84** (2011), pp. 085144–1–085144–10.

[109] I. P. Rusinov, I. A. Nechaev, and E. V. Chulkov. "Many-body effects on the width of the band gap in Bi_2Te_2X (X = Te, Se, S) Topological Insulators". *JETP Letters* **98** (2013), pp. 397–402.

[110] L. Hedin. "New method for calculating the one-particle Green's function with application to the electron-gas problem". *Physical Review* **139** (1965), A796.

[111] J. Vidal, X. Zhang, L. Yu, J.-W. Luo, and A. Zunger. "False-Positive and False-Negative assignments of Topological Insulators in density functional theory and hybrids". *Physical Review B* **84** (2011), pp. 041109–1–041109–4.

[112] P. Blaha, K. Schwarz, and J. Luitz. *Wien97-An Augmented Plane Wave Plus Local Orbitals Program for Calculating Crystal Properties, WIEN2k*. 16.1. Vienna, Austria: Vienna University of Technology Institute of Materials Chemistry, 1997.

[113] K. Schwarz, P. Blaha, and G. Madsen. "Electronic structure calculations of solids using the *WIEN2k* package for material sciences". *Computer Physics Communications* **147** (2002), pp. 71–76.

[114] J. P. Perdew, K. Burke, and E. Matthias. "Generalized Gradient Approximation Made Simple". *Physical Review Letters* **77** (1996), pp. 3865–3868.

[115] B. Yan, C. Felser, and S.-C. Zhang. "Topological Insulators - From Materials Design to Reality". *physica status solidi (RRL) - Rapid Research Letters* **7** (2013), pp. 13–14.

[116] T. R. F. Peixoto, H. Bentmann, S. Schreyeck, M. Winnerlein, C. Seibel, H. Maaß, M. Al-Baidhani, K. Treiber, S. Schatz, S. Grauer, C. Gould, K. Brunner, A. Ernst, L. W. Molenkamp, and F. Reinert. "Impurity states in the Magnetic Topological Insulator V:$(Bi,Sb)_2$ Te_3". *Physical Review B* **94** (2016), pp. 195140–1–195140–5.

[117] J. R. Arthur. "Molecular beam epitaxy". *Surface science* **500** (2002), pp. 189–217.

[118] S. Schreyeck, N. V. Tarakina, G. Karczewski, C. Schumacher, T. Borzenko, C. Brüne, H. Buhmann, C. Gould, K. Brunner, and L. W. Molenkamp. "Molecu-

lar beam epitaxy of high structural quality Bi_2Se_3 on lattice matched InP(111) substrates". *Applied Physics Letters* **102** (2013), pp. 041914–1–041914–4.

[119] H. Maaß, S. Schreyeck, S. Schatz, S. Fiedler, C. Seibel, P. Lutz, G. Karczewski, H. Bentmann, C. Gould, K. Brunner, L. Molenkamp, and F. Reinert. "Electronic structure and morphology of epitaxial Bi_2Te_2Se Topological". *Journal of Applied Physics* **116** (2014), pp. 193708–1–193708–4.

[120] J. Viefhaus, F. Scholz, S. Deinert, L. Glaser, M. Ilchen, J. Seltmann, P. Walter, and F. Siewert. "The Variable Polarization XUV Beamline P04 at PETRA III: Optics, mechanics and their performance". *Nuclear Instruments and Methods in Physics Research Section A: Accelerators, Spectrometers, Detectors and Associated Equipment* **710** (2013), pp. 151–154.

[121] S. Gusenleitner, E. Handik, D. Hauschild, and F. Reinert. "Quantitative analysis of electron energy loss spectra and modelling of optical properties of multilayer systems for extreme ultraviolet radiation regime". *J. Appl. Phys* **115** (2014), pp. 123513–1–123513–5.

[122] D. Briggs and J. T. Grant. *Surface analysis by Auger and x-ray photoelectron spectroscopy.* Manchester, UK: IMPublications, Chichester, UK and SurfaceSpectra, Manchester, UK, 2003.

[123] J. F. Moulder, E. F. Stickle, P. E. Sobol, and K. D. Bomben. *Handbook of X-Ray Photoelectron Spectroscopy.* eden prairie, minnesota, USA: Perkin-Elmer Corporation, Physical Electronics Division, 1992.

[124] D. A. Shirley. "High-resolution X-ray photoemission spectrum of the valence bands of gold". *Physical Review B* **5** (1972), pp. 4709–4714.

[125] J. M. Thomas, I. Adams, R. H. Williams, and M. Barber. "Valence band structures and core-electron energy levels in the monochalcogenides of gallium. Photoelectron spectroscopic study". *Journal of the Chemical Society, Faraday Transactions 2: Molecular and Chemical Physics* **68** (1972), pp. 755–764.

[126] S. Tougaard. "Quantitative Analysis of the Inelastic Background in Surface Electron Spectroscopy". *SURFACE AND IhTERFACE ANALYSIS* **11** (1988), pp. 453–472.

[127] S. Tougaard. "PRACTICAL ALGORITHM FOR BACKGROUND SUBTRACTION". *Surface Science* **216** (1989), pp. 343–360.

[128] S. Tougaard and H. Hansen. "Non-destructive depth profiling through quantitative analysis of surface electron spectra". **14** (1989), pp. 730–738.

[129] S. Tougaard. "Inelastic background correction and quantitative surface analysis". *Journal of Electron Spectroscopy and Related Phenomena* **52** (1990), pp. 243–271.

[130] S. Tougaard. "Accuracy of the Non-destructive Surface Nanostructure Quantification Technique Based on Analysis of the XPS or AES Peak Shape". *Surface and interface analysis* **26** (1998), pp. 249–269.

[131] M. P. Seah and M. T. Anthony. "Quantitative XPS: The calibration of spectrometer intensity-energy response functions. 1-The Establishment of Reference Procedures and Instrument Behaviour". *Surface and interface analysis* **6** (1984), pp. 230–241.

[132] J. J. Yeh and I. Lindau. "Atomic subshell photoionization cross sections and asymmetry parameters: $1 \leq Z \leq 103$". *Atomic data and nuclear data tables* **32** (1985), pp. 1–155.

[133] R. Hesse, P. Streubel, and R. Szargan. "Improved accuracy of quantitative XPS analysis using predetermined spectrometer transmission functions with UNIFIT 2004". *Surface and Interface Analysis* **37** (2005), pp. 589–607.

[134] M. G. Vergniory, M. M. Otrokov, D. Thonig, M. Hoffmann, I. V. Maznichenko, M. Geilhufe, X. Zubizarreta, S. Ostanin, A. Marmodoro, J. Henk, W. Hergert, I. Mertig, E. V. Chulkov, and A. Ernst. "Exchange interaction and its tuning in magnetic binary chalcogenides". *Physical Review B* **89** (2014), pp. 165202–1–165202–7.

[135] S. Nakajima. "The crystal structure of $Bi_2Te_{3-x}Se_x$". *Journal of Chemical Solids* **24** (1963), pp. 479–485.

[136] H.-A. Ullner. "Strukturuntersuchungen am System $Sb_2Te_{3-x}Se_x$ (Halbleitereigenschaften von Telluriden. VIII)". *Annalen der Physik* **476** (1968), pp. 45–56.

[137] A. Richardella, A. Kandala, J. S. Lee, and N. Samarth. "Characterizing the structure of Topological Insulator thin films". *APL Materials* **3** (2015), pp. 083303–1–083303–7.

[138] L. Fu. "Hexagonal Warping Effects in the Surface States of the Topological Insulator Bi_2Te_3". *Physical Review Letters* **103** (2009), pp. 266801–1–266801–4.

[139] T. P. Debies and J. Rabalais. "X-Ray Photoelectron spectra and electronic structure of Bi_2X_3 (X = O, S, Se, Te)". *Chemical Physics* **20** (1977), pp. 277–283.

[140] D. E. Eastman, T.-C. Chiang, P. Heimann, and F. J. Himpsel. "Surface core-level binding-energy shifts for GaAs (110) and GaSb (110)". *Physical Review Letters* **45** (1980), pp. 656–6659.

[141] N. J. Shevchik, M. Cardona, and J. Tejeda. "X-Ray and Far-uv Photoemission from Amorphous and Crystalline Films of Se and Te". *Physical Review B* **8** (1973), pp. 2833–2841.

[142] M. K. Bahl, R. L. Watson, and K. J. Irgolic. "X-Ray Photoemission studies of Tellurium and some of its compounds". *The Journal of Chemical Physics* **66** (1977), pp. 5526–5535.

[143] M. Stöger-Pollach. "Optical properties and bandgaps from low loss EELS: Pitfalls and solutions." *Micron* **39** (2008), pp. 1092–1110.

[144] S. Lazar, G. Botton, M.-Y. Wu, F. Tichelaar, and H. Zandbergen. "Materials science applications of HREELS in near edge structure analysis and low-energy loss spectroscopy". *Ultramicroscopy* **96** (2003), pp. 535–546.

[145] B. Rafferty and L. M. Brown. "Direct and indirect transitions in the region of the band gap using electron-energy-loss spectroscopy". *Physical Review B* **58** (1998), pp. 10326–10337.

[146] L. Surnev and G. Rangelov. "EELS study of a clean and an Oxygen covered Ru (001) surface". *Solid state communications* **54** (1985), pp. 783–785.

[147] J. Lindhard. "On the properties of a gas of charged particles". *Dan. Mat. Fys. Medd.* **28** (1954).

[148] A. C. Simonsen, F. Yubero, and S. Tougaard. "Quantitative model of electron energy loss in XPS". *Physical Review B* **56** (1997), pp. 1612–1619.

[149] S. Tougaard and F. Yubero. "QUEELS software package for calculation of surface effects in electron spectra". *Surface and Interface Analysis* **36** (2004), pp. 824–827.

[150] J. Hubbard. "The dielectric theory of electronic interactions in solids". *Proceedings of the Physical Society. Section A* **68** (1955), pp. 976–986.

[151] E. A. Stern and R. A. Ferrell. "Surface plasma oscillations of a degenerate electron gas". *Physical Review* **120** (1960), pp. 130–136.

[152] http://www.flapw.de. *FLAPW all-electron full-potential linearized augmented-plane-wave formalism.* FLAPW.

[153] C. Friedrich, S. Blügel, and A. Schindlmayr. "Efficient implementation of the GW approximation within the all-electron FLAPW method". *Physical Review B* **81** (2010), pp. 125102–1–125102–16.

[154] M. Calixto-Rodriguez, A. Tiburcio-Silver, A. Ortiz, and A. Sanchez-Juarez. "Optoelectronical properties of indium sulfide thin films prepared by spray pyrolysis for photovoltaic applications". *Thin Solid Films* **480-481** (2005), pp. 133–137.

[155] C Sanz, C Guillén, and J Herrero. "Annealing of indium sulfide thin films prepared at low temperature by modulated flux deposition". *Semiconductor Science and Technology* **28** (2013), pp. 015004–1–015004–6.

[156] R. Rumpf. *Lorentz and Drude models*. Lecture. 21st Century Electromagnetics, University of Texas at El Paso, USA, 2016.

Own Publications

- E. K. Al-Shakerchi, **M. Al-Baidhani**. "Thermoanalytical study and its effect on the nucleation growth of $Y_{0.7}Eu_{0.3}Ba_2Cu_3O_{7-\delta}$ Crystalline Superconductor". *Journal of Eng. And Tech. University of Technology*, **20**, (2001).

- E. Yousif, **M. Al-Baidhani**, S. Aliwi. "Optical properties modification of poly -styrene films by 2N-salicylidene-5-(p-nitro phenyl)-1,3,4-thiadiazole complexes". *Journal of Al-Nahrain University* **8**, (2005), pp.22 − 26

- N. J. Al-Mashhadani, N. F. Tawfiq, and **M. Al-Baidhani**. "Spectrophotometric study of γ-Irradiated PM-355". *Baghdad Science Journal* **6** (2009), pp. 584 − 589.

- **M. Al-Baidhani**. "Preparation of ultra fine $Li_{0.43}Zn_{0.195}Fe_{2.37}O_4$ Lithium Ferrite powder". *Journal of college of Education* **3** (2009), pp. 923 − 929.

- E. Yousif, **M. Al-Baidhani**, A. Hameed, N. Salih, J. Salimon. "Studying the conductivity of poly (vinyl chloride) using of 2-(sub.)-5-[3-(5-nitro-fur-2-yl)-propen-2-yldiene] amino -1,3,4- thidiazoles as additives by measuring forbidden energy gap". *Journal of Al-Nahrain University*, **13**, (2010), pp. 30 − 35

- E. K. Al-Shakerchi, **M. Al-Baidhani**, and O. Adnaan. "Designing and manufacture of HTSc flexible wire of Bi-2223". *Journal of Superconductivity and Novel Magnetism* **23** (2010), pp. 1251 − 1259.

- W. A. Al-Taa'y, T. K. Al-Rawi, and **M. Al-Baidhani**. "The optical properties of Poly Methyl Methacrylate (PMMA) polymers doped by Potassium Iodide with different thickness". *Baghdad Science Journal* **8** (2011), pp. 538 − 542.

- W. A. Al-Taa'y, **M. Al-Baidhani**, and T. K. Al-Rawi. "The MR affect on optical properties for Poly (Vinyl Alcohol) films". *Baghdad Science Journal* **8** (2011), pp. 543 − 550.

- W. A. Al-Taa'y, T. K. Al-Rawi, and **M. Al-Baidhani**. "Thickness effect on the optical constants of Poly Methyl Methacrylate (PMMA) doped by Potassium Iodide". *Journal of Al-Nahrain University* **16** (2013), pp. 119 − 123.

- W. Al-Taa'y, **M. Al-Baidhani**, R. M. Yusop,E. Yousif, B. M. Abdullah,J. Salimon, N. Salih, and S. I. Zubairi. "Effect of nano ZnO on the optical properties of Poly(Vinyl Chloride) films". *International Journal of Polymer Science* **2014** (2014), pp. $1-6$

- W. A. Al-Taa'y, **M. Al-Baidhani**, and E. Yousif. "The effect of $NiCl_2$ on the optical properties of Poly Vinyl Alcohol films". *Yanbu Journal of Engineering and Science* **8** (2014), pp. $40-45$

- A. Alwash, A. A. Ameer, **M. Al-Baidhan**i, A. Ahmed, Y.-F. Win, and E. Yousif. "Optical study on $NiSO_4$ doped PVA". *International Journal of Research in Pharmacy and Chemistry* **4** (2014), pp. $294-298$.

- W. A. Al-Taa'y, S. F. Oboudi, E. Yousif, **M. Al-Baidhani**, R. M. Yusop, and D. Derawi. "Fabrication and characterization of Nickel Chloride doped PMMA films". *Advances in Materials Science and Engineering* **2015** (2015), pp. $1-5$.

- S. F. Oboudi, **M. Al-Baidhani**, W. A. Al-Taa'y, R. M. Yusop, D. Derawi, and Y. Yousif. "Dispersion characterization of conductive polymer". *International Journal of Electrochemical Science* **10** (2015), pp. $1555-1562$.

- H. T. Salloom, W. A. Al-Taa'y, T. K. Al-Rawi, T. Jumaa, and **M. Al-Baidhani**. "Laser induced optical properties modification of Poly(Methyl Methacrylate) films doped with Antimony Trioxide Nanoparticles". *Journal of Physical Science and Application* **6** (2016), pp. $91-96$.

- T. R. F. Peixoto, H. Bentmann, S. Schreyeck, M. Winnerlein, C. Seibel, H. Maaß, **M. Al-Baidhani**, K. Treiber, S. Schatz, S. Grauer, C. Gould, K. Brunner, A. Ernst, L. W. Molenkamp, and F. Reinert. "Impurity states in the magnetic topological insulator V:$(Bi,Sb)_2Te_3$ ". *Physical Review B* **94** (2016), pp. $195140-1-195140-5$.

- W. A. Al-Taa'y, **M. Al-Baidhani**, S. F. Oboudi, and E. Yousif. "Effect of nano Sb_2O_3 on the dispersive optical constants of PMMA films". *Sultan Qaboos University Journal for Science [SQUJS]* **22** (2017), pp. $56-62$.

Acknowledgment

This work could only be born by the help of many people. I would like to take this opportunity to express my heartfelt thanks to all who have accompanied and assisted me during the period of my stay in *Deutschland* and have contributed to the success of this work.

A very special thanks to my supervisor Prof. Dr. Friedrich Reinert who gave me this opportunity to be a member of his chair and opened the doors for me to meet and discuss with best scientist of physics. Thanks for the support, advice and last but not least for his academic leadership. I am also grateful to Prof. Dr. Jean Geurts taking over the second report of this work. Furthermore, I would like to express my gratitude to Dr. Hendrik Bentmann for the intensive cooperation and guidance in the field of topological insulators. I would also like to forward my appreciation to Dr. Thiago Ribeiro Fonseca Peixoto for the close and successful assistance in all of research segments, from samples measurement through the result analysis and the support to build a mathematical model to calculate the losses of electrons.

In addition, my thanks and appreciation to Prof. Dr. Laurens W. Molenkamp and his team of the Experimental Physics III for the preparation of the topological insulators samples doped with ferromagnetic metals, specially Dr. Steffen Schreyeck and Martin Winnerlein for their scientific collaboration.

I would like to thank Sina Göhl-Gusenleitner, who gave me the first lessons in electron energy loss spectroscopy (EELS). I am also grateful to Dr. Dirk Hauschild from Karlsruhe Institute for Technology for the precious discussions about the quantitative analysis of electron energy loss in XPS spectra, as well as the dielectric function and optical properties of materials by the analysis of reflected electron energy loss spectrum (REELS). For him I forward my sincerest appreciation.

I am all gratitude to Dr. Ilya Nechaev from Donostia International Physics Center in San Sebastián, Spain, for the private discussions about the theoretical calculations, which enriched this dissertation a lot. Additionally, important theoretical discussions with Dr. Sudhir Kumar of the Institute of Engineering & Technology-M.J.P. Rohilkhand University, India. For him I forward all the gratitude.

I am grateful to the people who accompanied and helped me at the time of measurements in the Experimental Physics VII laboratories and at the synchrotron beamtimes at Helmholtz-Zentrum in Berlin (BESSYII) and Petra III at DESY, in Hamburg, specially to Dr. Henriette Maaß and Sonja Schatz.

My colleagues Dr. Andreas Benkert, Dr. Frank Meyer, Holger Schwab, Dr. Sebastian Fiedler, Peter Lutz and Katharina Treiber, thank you for supporting me on my study and specially in the run-up to this graduation. Also special thanks for the "organic crew" of the Experimental Physics VII: Martin Graus, Manuel Grimm, Christian Metzger for the computer software assistance and various scientific and life aspects. I am thankful to my colleagues in the office Sonja Schatz and Dean Nestorov, from whom I learned so many things.

I would like to address my gratitude to Priv. Doz. Dr. Achim Schöll for his academic support. All the respect and appreciation to the secretary of Experimental Physics VII, specially Frau Hiltrud Eaton. Thanks again to Dr. Henriette Maaß and Dr. Andreas Benkert for their assistance with LaTeX. I would like to thank the remaining members and former members of the Experimental Physics VII for their joy at work and for their spare time. I would like to thank Peter Lutz for his kind companionship during the summer-school in Mont Blanc, France. Also I would like to thank Dr. Sebastian Fiedler who helped me to fix the water cooling system of the neu ESCA system. All thanks and appreciation to my friend Dr. Christoph Seibel for his scientific cooperation during the research specially bringing the life back to the REELS measuring system, and for different matters of life.

I am also grateful to Sina, Holger, Christoph, Henriette, Sonja, Martin and Katharina, who many times accompanied me to the Rathaus Würzburg. Those were memorable hard days.

My appreciation to Prof. Dr. Nils Heeßel, the former Chair of Altorientalistik, in the Institut für Altertumswissenschaften of the Würzburg University, who guided me to the ancient Sumerian and Akkadian civilization cuneiform writing.

For the good times that we spent in *Deutschland* with Ahmed Al-Jarjari and Doreen Akawi, I forward them all appreciation.

To my friends inside and outside Iraq who helped me during my study especially, Dr. Mohammed Al-Taa'y for following up my scholarship file during my study time in *Deutschland*. Also my thanks to Dr. Emad Al-Sarraj and Wasan Al-Taa'y for their scientific cooperation in the field of polymers and its optical properties, which was rewarded with a prize of physics in 2016 at Al-Nahrain University in Iraq. For the assist and help of Dr. Emad Al-Shakarchi, I forward him all the appreciation.

All gratitude to my aunt Zakia, my uncle Abdul Jalil and Ahmed Al-Baidhani for their kind words as well as standing beside my parents during my study here in *Deutschland*.

My homeland Iraq, I know very well you will rise like the Phoenix, and your sun will shine again, thank you.

Last but not least, this work would not have been possible without the aid and support of my wife Hadeel Al-Rubaye, who is unfortunately deprived to attend my defense. Special thanks to my parents Brigadier General Tariq Al-Baidhani and Fakhriya Al-Jabri in Baghdad who have been behind me all the time. For my brother Ziad and my sister Esra Al-Baidhani, many thanks. My brother Ali Al-Baidhani in Berlin, who was with me from the first day in *Deutschland*, all the appreciation.